

ABSTRACT

KOOLIVAND, AMIR. Dynamics, Surface Electrostatics and Phase Properties of Nanoscale Curved Lipid Bilayers. (Under the direction of Prof. Alex Smirnov).

Surface electrostatic potential of a lipid bilayer governs many vital functions of living cells. Several classes of proteins are known of exhibiting strong binding preferences to curved lipid bilayer surfaces. In this project we employed electron paramagnetic resonance (EPR) of a recently introduced phospholipid (IMTSL-PTE) bearing a pH-sensitive nitroxide covalently attached to the lipid head group to measure the surface electrostatics of the lipid membrane and nanopore-confined lipid bilayers as a function of the bilayer curvature. The pK_a of the ionizable group of this lipid-based spin probe is reporting on the bilayer surface electrostatics potential by changes in the EPR spectra. Specifically, both rotational dynamics and magnetic parameters of the nitroxide are affected by the probe protonation. Effect of curvature on the surface electrostatic potential and dynamics of lipid bilayer was studied for POPG and DMPG unilamellar vesicles (ULVs). It was found that the magnitude of the negative surface electrostatic potential increased upon decrease in the vesicle diameter for the bilayers in the fluid phase; however, no significant changes were observed for DMPG ULVs in a gel phase. We speculate that biologically relevant fluid bilayer phase allows for a larger variability in the lipid packing density in the lipid polar head group region than a more ordered gel phase and it is likely that the lipid flip-flop is responsible for pH equilibration of IMTSL-PTE. The kinetic EPR study of nitroxide reduction showed that the rate of flip-flop is in the order of 10^{-5} s^{-1} . The flip-flop rate constant increases when vesicle size decreases. Oxygen permeability measured by X-ban EPR decreases in higher curved vesicles - an observation that is consistent with a tighter packing in smaller vesicles. Partitioning of a small nitroxide molecule TEMPO into ULVs was

measured by X-band (9 GHz) and W-band (95 GHz) EPR spectroscopy. The partitioning coefficient of this probe in the lipid phase of the bilayer was higher in smaller vesicles likely due to a larger number of defects in smaller vesicles allowing more water soluble molecules partitioning into lipid bilayers. However, the rotational correlation time for TEMPO slows down in smaller vesicles indicating an increase in the lipid packing. Pulsed EPR techniques, HYSCORE and ESEEM spectroscopy, were used to detect local water concentration and distinguish the hydrogen bonded water to the nitroxide from the bulk one. HYSCORE was then employed to investigate the effect of bilayer curvature on the water penetration into lipid bilayer and it was found that the higher curved lipids allow more water to penetrate into lipid bilayer as a result of more defects in the highly curved lipid vesicles.

Nanopore-confined lipid bilayers formed inside ordered nanochannels of anodic aluminum oxide (AAO) have found many practical applications, serving as thermodynamically stable biophysical models of cellular membranes of concave curvature and allowing for stabilization of membrane proteins in functional conformations. It was found that surface potential of POPG lipids inside the AAO pores are higher than that of vesicles – the effect that is attributed to highly ordered and packed lipids inside the AAO nanopores. At pH=7.0 the AAO zeta potential was found to be -29 ± 0.64 mV. Cytochrome C and poly glutamic acid as positively and negatively charged macromolecules in physiological pH (7.4) were used to prepare multilayer protein nanotubes and cytochrome c interaction with AAO was studied by CD and UV-Vis spectroscopy. Lipid nanotube arrays containing a transmembrane WALP peptide were also formed and these macroscopically aligned lipid nanotubes were studied by CD spectroscopy. The lipid phase transition of DMPC and binding

of melittin, an antibacterial peptide model, were observed from a frequency change for the QCM quartz-AAO-Lipid as a promising “biosensor”.

© Copyright 2015 Amir Koolivand

All Rights Reserved

Dynamics, Surface Electrostatics and Phase Properties of Nanoscale Curved Lipid Bilayers

by
Amir Koolivand

A dissertation submitted to the Graduate Faculty of
North Carolina State University
in partial fulfillment of the
requirements for the degree of
Doctor of Philosophy

Chemistry

Raleigh, North Carolina

2015

APPROVED BY:

Alex I. Smirnov
Committee Chair

Morteza G. Khaledi

Jerry L. Whitten

Keith R. Weninger

DEDICATION

To my family

BIOGRAPHY

Amir Koolivand was born in Nahavad, Iran, in July 1985. He grew up in a house where his father inspired him to pursue science major in his future. After finishing his middle school in Nahavand, he was accepted by a high school for talented students, Seifeh high school, in a nearby city, Malayer. His high school chemistry teacher found his interest in chemistry and biology and encouraged him to select one of those majors in the college. His interest to the science makes him to pursue his education in applied chemistry at Tabriz University which has one the best chemistry departments in Iran. He started his research career in the laboratory of Dr. Hosein Dastanagoo where he prepared modified electrodes to determine the hydrazine content in water and study its electrochemical properties. After finishing his bachelor, he got admitted at Tehran University, one of the oldest and best universities in Iran. He started his master's research on the synthesis of nanoporous material and its application in the adsorption process under the supervision of Prof. Alireza Badiei, and then he decided to continue his academic pursuits in the United States of America. An effective communication with Prof. Alex Smirnov about his research area was enough to encourage him to apply for North Carolina State University. He later joined his group in 2011 and continued his Ph.D. research on the biophysical properties in lipid bilayers.

ACKNOWLEDGMENTS

The following people are acknowledged for their contribution:

Prof. Alex Smirnov, Advisor;

Prof. Jerry Whitten, Prof. Morteza Khaledi and Prof. Keith R. Weninger

for being a part of the advisory committee;

Prof. Tatyana Smirnova for discussions and suggestions

Prof. Maxim Voinov for many discussions and help during research.

Dr. Antonin Marek for fabricating AAO membrane and providing help with QCM

Prof. Jacqueline Krim and her group for their help in QCM measurement

Prof. Smirnov and Prof. Smirnova groups

Prof. Khaledi group for helping in lipid extrusion

Prof. Nevzorov group for helping in lipid sonication

Family- father, mother, sisters and brother

Friends for their support

TABLE OF CONTENTS

List of Tables	vii
List of Figures.....	viii
Chapter 1. General Introduction	1
1.1 Lipids Bilayers and Vesicles	1
1.2 EPR (Electron Paramagnetic Resonance).....	4
1.3 Pulsed-EPR	10
1.3.1 ESEEM.....	13
1.3.2 HYSCORE.....	15
Chapter 2. Materials and Methods.....	18
2.1 Materials	18
2.2 Phospholipid Sample Preparation	19
2.2.1 Multilamellar Vesicle Preparation	19
2.2.2 Unilamellar Vesicle (ULV) Preparation	21
2.2.3 Preparation of Small Unilamellar Vesicles (SUV) Doped with Gramicidin A	22
2.2.4 Nanopore Confined Lipid Bilayers Preparation.....	22
2.3 CW-EPR Measurements.....	23
2.4 Differential Scanning Calorimetry (DSC).....	23
2.5 Zeta Potential Measurement, UV-Vis and CD Spectroscopy of AAO	24
2.6 Quartz Crystal Microbalance (QCM) Measurement	25
2.7 HYSCORE and ESEEM.....	26
2.8 pH Adjustment in Vesicles	26
2.9 pH Adjustment in Lipid Nanopore Confined Bilayer.....	27
2.10 Oxygen Permeability	27
2.11 Reduction of Spin Labeled Phospholipid: Kinetic Study.....	27
2.12 Partitioning into Lipid Bilayers.....	28
2.13 The Cytochrome C/Poly Glutamic Acid Layer Deposition	28
2.14 Melittin Interaction with Lipid Bilayers	29
Chapter 3. Electrostatic, Phase Properties and Dynamics of Phospholipid Vesicles... 30	
3.1 Introduction	30

3.2	Results and Discussion	41
3.2.1	Dynamic Light Scattering (DLS) and Differential Scanning Calorimetry (DSC)	41
3.2.2	Surface Electrostatic Potential Measurement	45
3.2.3	pH Equilibration of Both Inner and Outer Leaflets.....	63
3.2.4	Kinetics of Lipid Flip-Flops in Unilamellar Vesicles.....	66
3.2.5	Dynamics inside Lipid Bilayers	75
3.2.6	Conclusions.....	86
Chapter 4.	The Surface Electrostatics and Phase Properties of the Nanopore-confined Lipid Bilayers	89
4.1	Introduction	89
4.2	Results and Discussion.....	93
4.2.1	Surface Potential Measurement of Confined Lipid Bilayers	93
4.2.2	AAO Surface Charge.....	97
4.2.3	Protein Deposition into AAO	99
4.2.4	EPR and UV-Vis Spectroscopy of AAO.....	105
4.2.5	Phase Transition of Nanopore Confined Lipid Bilayers As Studied by Quartz Crystal Microbalance (QCM).....	109
4.2.6	Melittin-Lipid Interaction	118
4.3	Conclusions	120
Chapter 5.	Hydrogen Bonding through Lipid Bilayers as Assessed by ESEEM and HYSORE 122	
5.1	Introduction	122
5.2	Results and Discussion.....	124
5.2.1	X-band EPR.....	124
5.2.2	ESEEM of D ₂ O and CH ₃ OD in Diglyme.....	126
5.2.3	HYSORE of D ₂ O and CH ₃ OD in Diglyme.....	134
5.2.4	Water Penetration into the Unilamellar Vesicles.....	140
5.3	Conclusions	146
	Summary.....	147
	References	152

LIST OF TABLES

<i>Table 3-1 Size stability of DMPG ULVs at different temperatures</i>	<i>42</i>
<i>Table 3-2 Interfacial pK_{ai} and polarity induced shifts measured for Triton-X-100 with 1% IMTSL-PTE [52]......</i>	<i>49</i>
<i>Table 3-3 Interfacial pK_a^i, polarity-induced and electrostatic shifts, ΔpK_a^{el}, measured for POPG SUVs doped with 1% IMTSL-PTE at 17 °C. Data for MLV was reported in ref [26].</i>	<i>57</i>
<i>Table 3-4 EPR titration results for POPG SUVs prepared by extrusion through 100 nm membrane with and without gramicidin A.....</i>	<i>65</i>
<i>Table 3-5 The theoretical and experimental ratio of inner leaflet lipids to the total number of lipids in one vesicle.....</i>	<i>71</i>
<i>Table 3-6 Rate constants for the outer leaflet ascorbic acid reduction and transverse diffusion in POPG unilamellar vesicles at various size and temperature.</i>	<i>73</i>
<i>Table 3-7 Oxygen permeability measured as Lorentzian broadening (peak-to-peak) for POPG and DMPG unilamellar vesicles doped with 1 mol% 5PC. The error was calculated from fitting of the experimental spectrum.</i>	<i>78</i>
<i>Table 3-8 Partitioning of TEMPO between lipid and aqueous phases of POPG ULVs measured by X-band EPR at 22 °C.....</i>	<i>82</i>
<i>Table 4-1 Surface electrostatic potential and interfacial pK_a of nanopore-confined POPG (AAO pore size: 200nm).....</i>	<i>97</i>

LIST OF FIGURES

<i>Figure 1-1 General phospholipid molecule structure presented by different models (figure adopted from ref [2]).</i>	1
<i>Figure 1-2 Structure of lipid phases in lamellar and micellar phases: a) subgel, b) gel untilted, c) gel titled, d) rippled gel, e) fully interdigitated gel, f) partially interdigitated gel, g) mixed interdigitated gel, h) liquid crystalline, i) spherical micelles, j) cylindrical micelles, l) inverted micelles and m) liposome (reproduced from ref [5]).</i>	3
<i>Figure 1-3 Phase transition of lipid bilayers from $L\beta$ to $L\alpha$. The rippled structure is formed upon transition and the thickness of bilayer decreases. Reproduced from ref [4].</i>	4
<i>Figure 1-4 The energy diagram of an unpaired electron in an external magnetic field, B.</i>	6
<i>Figure 1-5 Chemical structure a nitroxide radical: TEMPO (2,2,6,6-Tetramethylpiperidin-1-yl)oxyl) and its three X-band EPR lines: each energy levels splits in three levels and resonance frequency gives rise to three lines in X-band EPR.</i>	8
<i>Figure 1-6 X-band EPR spectra sensitivity to the motion of the radical: A)MTSL in solution (fast motion) B)MTSL bond to a small peptide in solution, C)The same spin labeled peptide in B folded in α helix and D) a spin labeled peptide in frozen sample.</i>	10
<i>Figure 1-7 Vector model representing magnetization vector aligned with z-axis in the presence of magnetic field (B_0); and after π (180°) and $\pi/2$ (90°) pulses.</i>	11
<i>Figure 1-8 Single $\pi/2$ pulse EPR: a) decay of magnetization along x-y plane after $\pi/2$ pulse, b) FID converted to corresponding EPR spectrum by Fourier transform (adopted from ref[12]).</i>	12
<i>Figure 1-9 Two-pulse spin echo sequence; a $\pi/2$ pulse followed by a π pulse to generate signal (acquired from ref [13]).</i>	13
<i>Figure 1-10 a) Pulse sequences for two and three- pulse ESEEM; at the time τ after the last pulse, modulation envelope is obtained. Echo is recorded while τ (for 2 pulse ESEEM) or T (for 3 pulse ESEEM) increases (reproduced from ref [15]) b) representative echo amplitude as a function of the interval between the pulses in two pulse ESEEM before Fourier transformation (acquired from ref [12]).</i>	15
<i>Figure 1-11 Pulse sequence for the HYSCORE technique. τ could be 30 to 500 ns [12], (reproduced from ref [14]).</i>	16
<i>Figure 1-12 Left) A schematic HYSCORE spectrum for $I=1/2$ (nucleus). The hyperfine coupling for peaks appeared in the right quadrant is smaller than twice nuclear Larmor frequency (orang signal). If the hyperfine coupling is higher than twice nuclear Larmor frequency, signals are expected to be in left quadrant. Right) the nuclear transient states evolve in two different electron spin manifolds (acquired from ref [14]).</i>	17
<i>Figure 2-1 Chemical structure of POPG.</i>	18
<i>Figure 2-2 Chemical structure of DMPG.</i>	19
<i>Figure 2-3 Chemical structure of DMPC.</i>	19
<i>Figure 2-4 Cartoon illustrating the mechanism of lipid vesicle formation (acquired from ref [17]). SUV, LUV and MLV stand for small unillamellar vesicle, large unilamellar vesicle and multilamelallar vesicles respectively.</i>	20

Figure 2-5 Quartz cuvette (1 mm) used to measure CD and UV-Vis spectra for AAO based samples: a black paper attached to cuvette with a pinhole helps to avoid light scattering.....	24
Figure 3-1 Electrostatic potentials across phospholipid bilayers; the surface potential Ψ_s due to charged groups at the interface, the transmembrane potential ($\Delta\Psi$) results from the net separation of charge across the membranes, and Ψ_d is the membrane dipole potential which is due to molecular dipole layer at the membrane-solution interface. Reproduced from ref [29]......	32
Figure 3-2 A cartoon shows the association of spin probes with the surface of lipid bilayer. Chemical structure of the probe, N, N-dimethyl-N-nonyl-NTEMPOylammonium bromide is shown. Reproduced from ref [41]......	34
Figure 3-3 A cartoon illustrating formation of diffuse double layer formed at a negatively charged surface based on the Gouy-Chapman theory.....	37
Figure 3-4 Chemical structure of a synthetic spin-labeled phospholipid (IMTSL PTE).....	39
Figure 3-5 Intensity size distribution of DMPG ULVs at different temperature: a) DMPG ULVs prepared by passing through 100 nm membrane and b) DMPG ULVs prepared by passing through 50 nm membrane.....	42
Figure 3-6 Z-Average diameters of DMPG ULVs measured by DLS at 48 °C. The DMPG vesicle concentration is 0.25% w/v.....	43
Figure 3-7 DSC traces of 5 % w/v DMPG multilamellar and unilamellar vesicles (30 and 100 nm). The DSC was performed with scan rate of 2 °C/min.....	44
Figure 3-8 Left: Experimental X-band EPR spectra of IMTSL-ME at 17 °C as a function of pH indicated next to the spectra. Right: An EPR titration curve obtained by fitting experimental a_N (filled squares) to a modified Henderson-Hasselbalch equation shown as a solid line [52]......	47
Figure 3-9 Triton X-100 chemical structure.....	48
Figure 3-10 Protonation of IMTSL-PTE at the interface of vesicles.....	49
Figure 3-11 Representative X-band (9.5 GHz) EPR spectra of unilamellar phospholipid vesicles composed of a) POPG (106 nm at 17 °C), b) DMPG (112 nm at 48 °C) doped with 1 mol % of IMTSL-PTE and measured at various pH. Dashed lines represent a guide for an eye to highlight the appearance of the protonated form at lower pH. ...	50
Figure 3-12. X-band EPR spectra of DMPG unilamellar 100 nm vesicles with appearance of free spin label at pH=7.00 (note the arrow) before and after spinning down.	52
Figure 3-13 Least-squares decomposition of the experimental X-band (9.5 GHz) EPR spectrum acquired from IMTSL-PTE 1%-doped 109 nm unilamellar POPG vesicles at pH=4.88 and 17 °C. A: Experimental spectrum; Least-squares simulated spectra of (B) nonprotonated and (C) protonated forms of the nitroxide; (D) simulated spectrum; (E) residual of the fit.	54
Figure 3-14 Titration curve of POPG small unilamellar vesicles (SUVs) doped with IMTSL-PTE 1% with diameter of 109 nm at 17 °C.....	56
Figure 3-15 Phase transition temperature at various pH in DMPG lipid (adopted from reference [27])......	59

Figure 3-16 a) Effect of curvature (vesicle diameter) on the surface electrostatic potential in lipid unilamellar vesicles; b) Zeta potentials for unilamellar vesicles vs. vesicle diameter.	62
Figure 3-17 A cartoon illustrating zeta and surface potentials in curved lipid bilayers.	63
Figure 3-18 Left: X-band EPR spectra at various pH; 107 nm POPG with gramicidin A at 17 °C, right: EPR titration curve fitted into Henderson-Hasselbalch equation.	64
Figure 3-19 Schematic representation of the phospholipid transverse diffusion.....	65
Figure 3-20 Reduction of a nitroxide radical with sodium ascorbate produces an EPR-silent hydroxylamine.....	66
Figure 3-21 Experimental data fitted into eq. 3-20: POPG unilamellar vesicles (diameter: 106 nm) at 17 °C.	69
Figure 3-22 Experimental data fitted into eq. 3-20: POPG unilamellar vesicles (diameter: 30 nm) at 17 °C.....	69
Figure 3-23 Experimental EPR nitroxide reduction data fitted into eq. 3-23: POPG unilamellar vesicles (diameter: 106 nm) at 0 °C.	71
Figure 3-24 Experimental EPR nitroxide reduction data fitted into eq. 3-23: POPG unilamellar vesicles (diameter: 30 nm) at 0 °C.	72
Figure 3-25 A cartoon of an EPR nitroxide reduction experiments to determine the phospholipid flip-flop rate. Sodium ascorbate reduces the outer spin labeled phospholipids and due to the lack of flip-flop at a low temperature, the EPR intensity of the inner leaflets remains (orange circles represent nitroxide radicals).	72
Figure 3-26 Calculation of theoretical “ α ” for POPG ULVs. Yellow circles represent spin labeled phospholipids.	73
Figure 3-27 Graphical presentation of lipid bilayer oxygen permeability and chemical structure of 5-Doxyl-PC (1-palmitoyl-2-stearoyl-(5-doxyl)-sn-glycero-phosphocholine).	75
Figure 3-28 Experimental X-band EPR spectra of DMPG ULVs (108 nm) labeled with 5- PC at 1 mol% in the presence of 100% O ₂ (black line) and 100% N ₂ (red line) at 1 atm and 30.5 °C.....	77
Figure 3-29 Experimental X-band EPR spectra at 22 °C of POPG ULVs (27 and 100 nm) and TEMPO. The amplitudes of the splitting in high field (H and P) can be used to calculate partitioning coefficient. Amplitude of H and P are approximately proportional lipid and aqueous phases respectively as discussed in ref [76].	80
Figure 3-30 Decomposition of X-Band EPR spectra of TEMPO partitioning into POPG ULVs (left: 27nm and right: 100nm).	81
Figure 3-31 Left) Least-squares decomposition of an experimental W-band (95 GHz) EPR spectrum of TEMPO for partitioning in 100 and 27 nm POPG ULVs: Experimental EPR, simulated EPR in lipid phase, simulated EPR in aqueous phase and residual of the fit. Right) Partitioning of TEMPO into the lipid phase in different diameters for POPG ULVs at 22 °C.	85
Figure 4-1 Two types of lipid bilayer depositions on inorganic substrate: a) deposition on a planar substrate, b) deposition into inorganic substrate nanochannels (nanotube	

array: arrows show the area exposed to the aqueous media. Reproduced from ref [83].	90
Figure 4-2 Left: high-resolution 94.4 GHz (W-band) EPR spectrum of randomly dispersed vesicles (in rigid limit) and the orientation of nitroxide magnetic axes with respect to molecular frame. Right: high-resolution 94.4 GHz (W-band) EPR spectrum of AAO substrate with deposited DMPC: 5PC (100:1) at two orientations of the substrate surface in the magnetic field. Cartoon shown is the structure of lipid bilayer inside AAO nanopores. Reproduced from [82]......	91
Figure 4-3. EPR spectra from AAO-supported POPG lipid bilayer doped with 1 mol. % of IMTSL-PTE measured at various pH. Left: Supported bilayers were obtained through hot plate deposition/freeze-thaw cycling. Right: Supported bilayers were prepared through syringe lipid extruder.	94
Figure 4-4 An example of a least-squares decomposition of an EPR spectrum acquired from IMTSL-PTE lipid in POPG bilayer confined within the 200 nm AAO nanopore and equilibrated with a buffer solution at pH = 5.00 into individual spectra of the protonated and the nonprotonated forms. (A) Experimental spectrum; Least-squares simulated spectra of (B) nonprotonated and (C) protonated forms of the nitroxide; (D) simulated spectrum; (E) residual of the fit.	95
Figure 4-5. Fraction of the nonprotonated form of the IMTSL-PTE plotted as a function of pH. Solid line represents the least-squares Henderson-Hasselbalch titration curve. POPG lipids were deposited into AAO through the hot-plate method.....	96
Figure 4-6 Zeta potential titration of AAO (200 nm) in 50 mM phosphate buffer.	98
Figure 4-7 a) Far-UV CD spectra of AAO before and after deposition of cyto-c b) AAO membrane before and after deposition and c) far-UV CD spectrum of cyto-c in aqueous solution (0.2 mg/ml). Spectra were taken at 22 °C with scan rate of 20 nm/min.	101
Figure 4-8 Right: Near UV CD spectra and Left: Soret region CD spectra; a) before and after deposition of cyto-c, b) “a” after subtracting AAO background, c) before and after deposition of cyto-c, d) “c” after subtracting AAO background. e and f) cyto-c in aqueous solution (1 mg/ml). Spectra were taken with scan rate 20 nm/min at 22° C.	102
Figure 4-9 Cyto-c absorbance in left) aqueous solution (1mg/ml) Right) Cyto-C layers deposited into AAO. Red line represents the he AAO absorbance. Absorbance peak in cyto-c solution is 410 nm and for one layer cyto-c deposited on AAO (blue line) is 407 nm.....	104
Figure 4-10 CD Spectra of AAO with (solid line) and without DOPG (dashed line) adopted with WALP peptide. The molar ratio of peptide to lipid was 1:150.	105
Figure 4-11 X-band EPR of AAO upon heating from 300 to 900 °C; each sample was heated with rate of 2 °C/min and kept at final temperature for 1 hr and then cooled down with rate of 10 °C/min to the room temperature. Each spectrum was taken with 1000 scans. The final temperature that AAO was treated at, is shown for each spectrum.	107
Figure 4-12 UV-Vis Spectroscopy of AAO treated at various temperature (shown on each spectrum). All spectrum were taken at room temperature and AAO was kept wet during	

measurement. The AAO samples were prepared and treated the same as for X-band EPR study in Figure 4-11.	108
Figure 4-13 A Quartz Crystal Microbalance (QCM) crystal with nanopore confined bilayers (AAO-lipid).	109
Figure 4-14 Water adsorption/desorption isotherm at 22 °C on AAO-quartz crystal. Arrow shows the frequency related to the end of hysteresis which was used to characterize the pore diameter.	110
Figure 4-15 BET plot for AAO-QCM crystal obtained from adsorption plot of water adsorption/desorption isotherm at 22 °C.	113
Figure 4-16 Frequency change of QCM-AAO crystal with and without DMPC deposited on compared to the original 5 MHz frequency of crystal without lipid and AAO (f_0); the main phase transition is about 24°C. To compare two plots, the Δf interval scale in frequency axis was kept the same.	114
Figure 4-17 Voltage change of QCM-AAO crystal with DMPC deposited on; to compare two plots, the voltage scale intervals were kept the same.	117
Figure 4-18 Melittin effect on nanopore confined lipid bilayer, A: Adsorption of melittin on the surface, B: disruption of lipid bilayers.	119
Figure 5-1 chemical structure diglyme used as glass forming solvent.	125
Figure 5-2 X-band EPR spectra of H ₂ O/diglyme mixture (Vol. %) with 1 mM TEMPO at 77 K. Dashed lines show how the outer hyperfine changes upon increasing H ₂ O percentage.	125
Figure 5-3 Three-pulse ESEEM time domain trace for 10 volume % of D ₂ O/H ₂ O (70 % v/v) in diglyme.	127
Figure 5-4 Fourier transformation of three-Pulse time domain for D ₂ O in diglyme: 10 volume % of D ₂ O/H ₂ O in diglyme. The top plot is zoom-in part of the ESSEM related to deuterium (D ₂ O) frequency (matrix deuteron signal).	128
Figure 5-5 The matrix deuteron amplitude of three-pulse ESEEM dependency to the D ₂ O (70 % D ₂ O/H ₂ O) concentration in diglyme.	130
Figure 5-6 Three-pulse-ESEEM of different mixtures of CH ₃ OD/diglyme (Vol. %) with 2 mM TEMPOL. The intensity was normalized for the comparison; one should compare the ratio of deuterium peak (at 2.3 GHz) with respect to the ¹ H matrix peak at 14.6 GHz. Right: zoom-in ESEEM of 50 % CH ₃ OD/diglyme which shows the splitting caused by quadrupole interaction between ² H and electron spin.	132
Figure 5-7 The matrix deuteron amplitude of three-pulse ESEEM dependency to the CH ₃ OD concentration in diglyme. The deviation from linear dependency is as a result of hydrogen bond formation with nitroxide radicals.	133
Figure 5-8 A) Contour presentation of HYSORE for 50 v/v % D ₂ O/H ₂ O (70 %) in diglyme with 2 mM TEMPOL at 77 K. B) Cross-peaks from Deuterons H-bonded to NO group.	135
Figure 5-9 Skyline projection of 2D-HYSORE spectrum for 50 v/v % D ₂ O/H ₂ O (70 %) in diglyme with 2 mM TEMPOL at 77 K. The corresponding peaks are assigned.	136

<i>Figure 5-10 The H-bonded amplitude extracted from HYSORE versus the concentration of D₂O/H₂O (70 %) in diglyme. The intensity is related to the skyline projection plot located at 1.8 and 3 GHz.</i>	<i>137</i>
<i>Figure 5-11 Cross-peaks from Deuterons H-bonded to NO group in 1 mM TEMPOL in 100 % CH₃OD.</i>	<i>138</i>
<i>Figure 5-12 The H-bonded amplitude extracted from HYSORE versus the concentration of CH₃OD in diglyme (v/v %).</i>	<i>139</i>
<i>Figure 5-13 Three pulse-ESEEM spectra of 60 nm (green line) and 30 nm (blue line) POPG ULVs with 1.7 mole % 10PC.</i>	<i>140</i>
<i>Figure 5-14 HYSORE of 60 nm POPG ULVs doped with 1.7 mole % 10PC. The black arrow in the spectrum shows deuterons hydrogen bonded to the nitroxide radical. The strong peak at 14.6 GHz corresponds to the protons in the matrix.</i>	<i>141</i>
<i>Figure 5-15 A) HYSORE Cross-peaks from deuterons H-bonded to NO group (left: 60 nm, right 30 nm ULVs B) Skyline projection of cross-peaks of 60 nm (green line) and 30 nm (blue line) POPG ULVs with 1.7 mole % 10PC.</i>	<i>142</i>
<i>Figure 5-16 HYSORE Cross-peaks from deuterons H-bonded to the NO group (left: 116 nm, right: 69 nm ULVs B) Skyline projection of cross-peaks of 116 nm (green line) and 69 nm (blue line) POPG ULVs with 1.7 mole % 5PC.</i>	<i>144</i>
<i>Figure 5-17 Model of highly curved lipid bilayers; the smaller vesicles have more defects in the lipid bilayer.</i>	<i>145</i>

Chapter 1. General Introduction

1.1 Lipids Bilayers and Vesicles

Biological membranes mainly composed from phospholipids play many important roles in cellular biology such as serving as ion barriers and providing an interface for assembly of membrane proteins [1]. Lipid bilayers have been known as a universal model for studying cell membrane structure and its properties. Almost 50 % of animal cell membrane mass consists of lipid bilayers and there are about $5 \cdot 10^6$ lipid molecules per every $1 \mu\text{m}^2$ of lipid bilayers. Lipids are amphiphilic molecules which means they are composed of a hydrophilic head and a hydrophobic end tail (Figure 1-1) [2]. Replacing the choline part with other functional groups modifies the surface charge of the lipid bilayer (*e.g.*, $-\text{CH}_2-\text{CH}(\text{OH})-\text{CH}_2\text{OH}$ would make the surface positively charged).

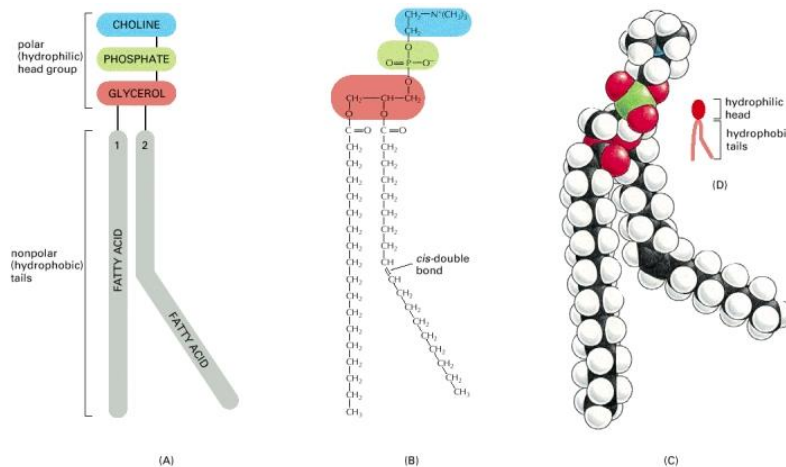


Figure 1-1 General phospholipid molecule structure presented by different models (figure adopted from ref [2]).

Liposomes are formed when lipids are dispersed in water where the lipid bilayers encloses an aqueous volume. Their size varies from nanometers to micrometers in diameter and they are considered to be a good model for studying cell membrane properties: liposome membrane bilayer is literally identical to the lipid portion of natural membranes as proposed by Singer and Nicholson in 1972 [3, 4].

Depending on the molecular structure and environmental conditions, lipids are capable of self-assembling into a variety of structures and phases when dispersed in water. When forming bilayers, the lipid phase state (*e.g.*, gel, crystalline or liquid crystalline) is also affected by temperature and to a lesser degree by pH. The nomenclature to designate lipid phases consists of the upper case Latin letters; for example, L is used for one-dimensional lamellar lattice and, P for the two-dimensional one. Subscripts are also used to describe chain conformations; for example, α stands for a disordered (liquid) and β for an ordered (gel) phases. Figure 1-2 shows the possible structures of lipids in aqueous media [5].

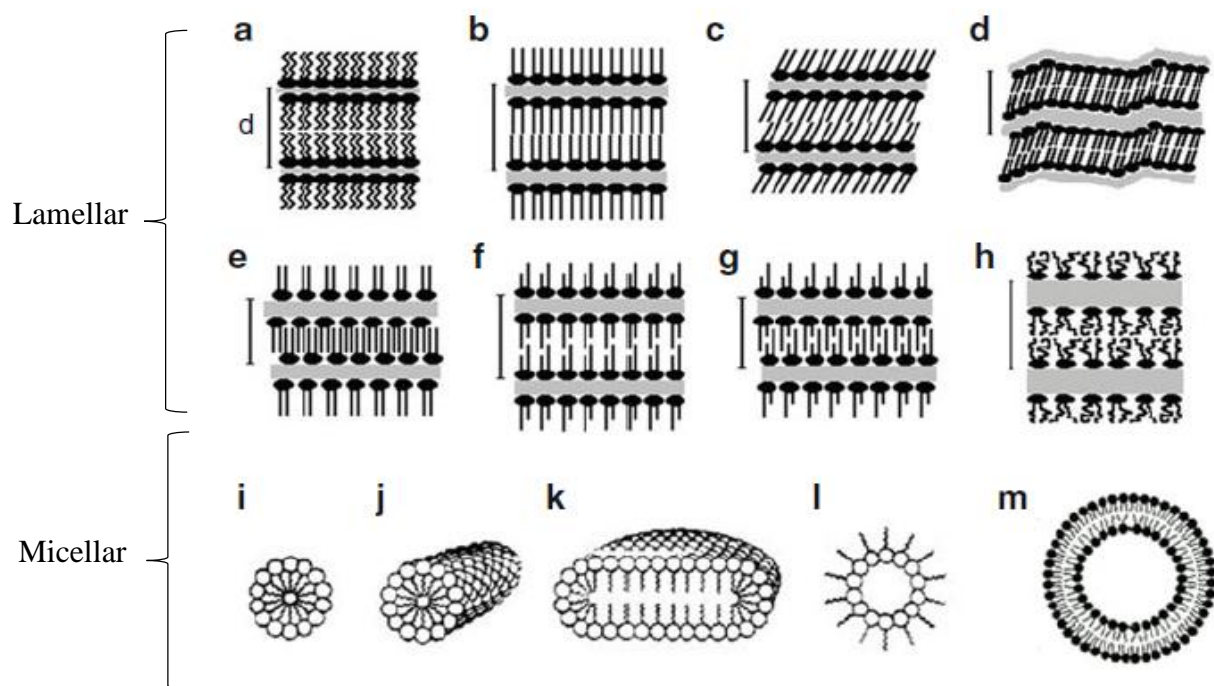


Figure 1-2 Structure of lipid phases in lamellar and micellar phases: a) subgel, b) gel untilted, c) gel tilted, d) rippled gel, e) fully interdigitated gel, f) partially interdigitated gel, g) mixed interdigitated gel, h) liquid crystalline, i) spherical micelles, j) cylindrical micelles, l) inverted micelles and m) liposome (reproduced from ref [5]).

The main and the most important lipid bilayer phase transition in biologically relevant systems is a transition between gel–lamellar and liquid-crystalline (L_{β} - L_{α}) phases. This transition, that will be one of the focuses of our study, occurs with a large enthalpy change [5]. The phase transition is not a single step process but involves in a pre-transition step. When a lipid bilayer undergoes a transition from L_{α} to L_{β} , the length of acyl chain increases due to the elimination of the chain tilt, resulting in an increase in the bilayer thickness. The intermediate “rippled” structure has an undulating surface appearing upon transition from L_{β} to L_{α} (Figure 1-3).

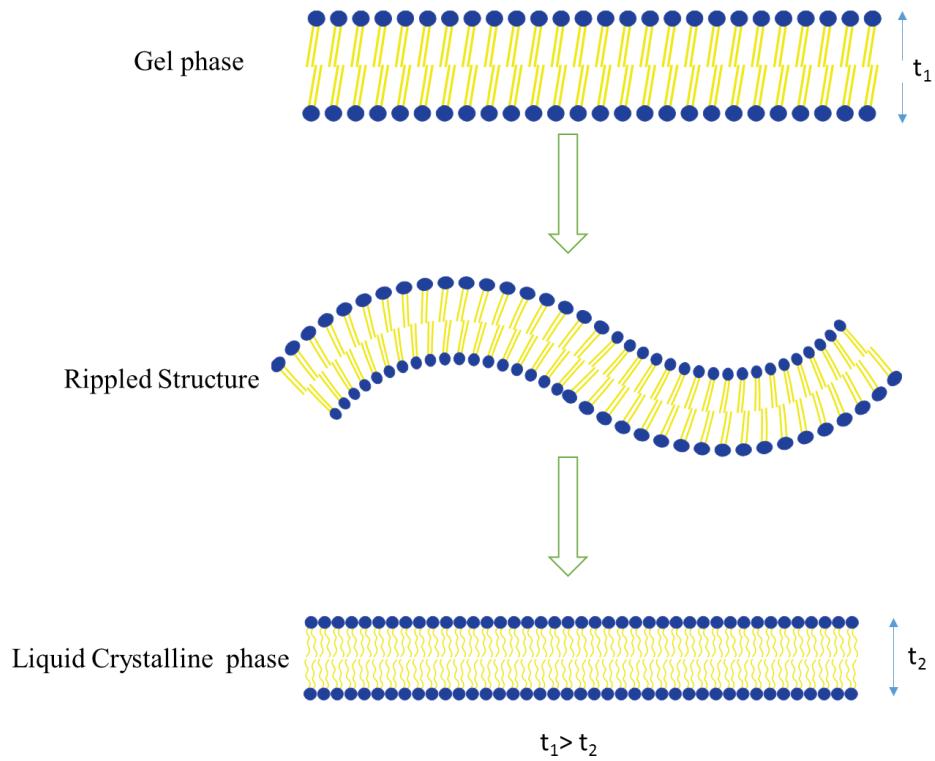


Figure 1-3 Phase transition of lipid bilayers from $L\beta$ to $L\alpha$. The rippled structure is formed upon transition and the thickness of bilayer decreases. Reproduced from ref [4].

In this work we mainly used unilamellar vesicles (liposomes) and studied phase, curvature and surface properties of such bilayers with different biophysical techniques.

1.2 EPR (Electron Paramagnetic Resonance)

EPR is a technique for studying molecular systems that have at least one unpaired electron in their structure and it is the most selective and highly sensitive spectroscopy for the characterization of such systems.

An unpaired electron with spin 1/2 in an external magnetic field, B, would occupy two energy levels. Figure 1-4 shows the energy diagram of an unpaired electron in an external magnetic field. The energy difference at the resonance condition can be expressed as:

$$h\nu = g_e\mu_e B \quad 1-1$$

where μ_e is Bohr magneton constant and ν is the resonance frequency of the transition. g factor is an important parameter in EPR spectroscopy and its value for a free unpaired electron in a vacuum is 2.0023. For molecular species g-factor depends on the radical environment and its electronic structure. EPR spectrum is acquired by monitoring the microwave absorption as the magnetic field is scanned while the frequency (ν) is constant [6]. Nowadays EPR spectra are acquired at different resonant frequencies such as X-band (9 GHz), Q-band (35 GHz) and W-band (95 GHz). In terms of minimal number of detectable spins EPR is much more sensitive than NMR because for the same temperature and magnetic field 1) the population difference between the spin states are higher than that for nuclei in NMR and 2) the energy of the absorbed electromagnetic quantum is greater by ca. 3 orders of magnitude [7].

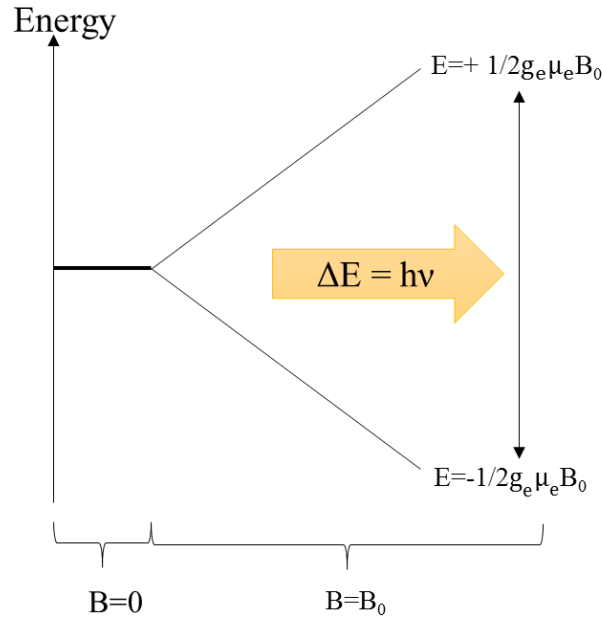


Figure 1-4 The energy diagram of an unpaired electron in an external magnetic field, B

The energy of paramagnetic species with electron spin, S , and a coupled nuclei with spin, I , can be expressed by spin Hamiltonian:

$$H = H_{EZ} + H_{ZFS} + H_{HF} + H_{NZ} + H_{NQ} + H_{NN} \quad 1-2$$

where the terms on the right side of the equation are respectively defined as the electronic Zeeman interaction (an interaction between the electronic spin and the external magnetic field), the zero-field splitting (energy splitting in the absence of magnetic field observed when $S > 1/2$), hyperfine couplings, nuclear Zeeman interactions, the quadrupole interactions (when $I > 1/2$, it is a weak interaction and can be observed in the nuclear frequency measured by EPR but they are hardly observable in EPR, and nuclear spin-spin interactions (they are too weak to be observed in the EPR spectra) [8]. One of the most important

parameters that can be obtained from EPR spectroscopy is the magnitude of the nuclear hyperfine interaction (H_{HF}).

In this work, we used nitroxide radicals as spin probes or spin labeled molecules, and many of these energy terms described in equation 1-2 can be neglected for ^{14}N ($I=1$). The spin Hamiltonian for an electronic spin interacting with ^{14}N nucleus breaks down to three main contributions: electronic Zeeman interactions, nuclear Zeeman interactions and hyperfine coupling interactions. In the high field approximation when the Zeeman terms dominates, the energy levels and the allowed transitions are given by ($\Delta M_I=0$ and $\Delta M_S=\pm 1$) [8, 9]:

$$E_{NO} = g_e \mu_e B M_S + g_N \mu_N B M_I + A M_S M_I \quad 1-3$$

$$\Delta E_{NO} = g_e \mu_e B + A M_S M_I \quad 1-4$$

where, M_S , M_I and A are electron spin quantum number, nuclear spin quantum number and the nitrogen hyperfine coupling constant respectively. The second term, the nuclear Zeeman interaction does not affect the transition frequencies in EPR; however, it can be observed in advanced pulsed EPR experiments [8]. The hyperfine interaction, which is the interaction of an unpaired electron with a nitrogen nucleus, produces small changes in the electronic spin energy levels (second term on the right side of the equation 1-4). Interaction of the nitrogen atom with the electronic spin results in splitting of EPR energy levels into three sublevels corresponding to different states of ^{14}N nuclei ($M_I = -1, 0, 1$). Spin labeled molecules may contain some other magnetic nuclei such as ^{17}O , ^1H and ^{13}C but the natural abundance of such isotopes are low and so the intensities of the corresponding lines (Figure 1-5) [10].

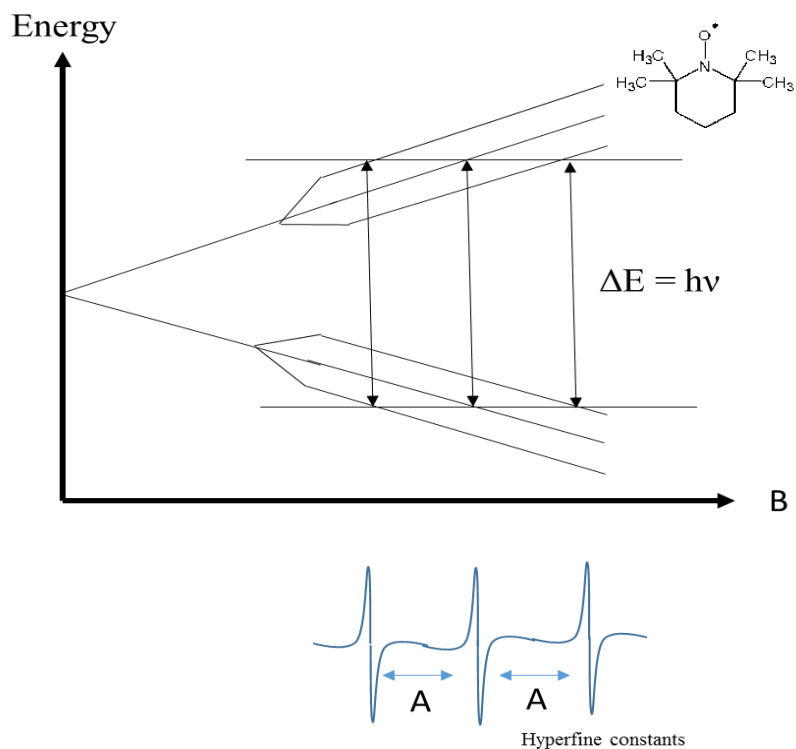


Figure 1-5 Chemical structure a nitroxide radical: TEMPO (2,2,6,6-Tetramethylpiperidin-1-yl)oxyl) and its three X-band EPR lines: each energy levels splits in three levels and resonance frequency gives rise to three lines in X-band EPR.

The electron density at the nucleus determines the magnitude of hyperfine interaction and any environmental or structural change affecting the electron density can be observed in hyperfine interaction. For example, water as a polar solvent increases the polarization at N-O bond resulting in an increase in the nitrogen isotropic hyperfine constant [10]. Hyperfine interaction could be isotropic or anisotropic (sample oriented dependent) and it depends on the

interaction origin; if it is due to dipole interaction between nucleus and electron spin then it predominates the anisotropic interaction and if the Fermi contact is the source of hyperfine interaction, the isotropic interaction is observed [6].

One of the useful information that we are able to obtain from EPR parameters is the rotational motion of the radical molecule. X-band EPR spectra reflect the radical rotational motion in the time scale of 0.1 to 100 nsec. Figure 1-6 shows how MTSL (S-(1-oxy1-2,2,5,5-tetramethyl-2,5-dihydro-1H-pyrrol-3-yl)methyl methanesulfonothioate) EPR spectrum changes when nitroxide radical experiences different local environments; generally, the slower rotational motion in radical, the broader EPR spectrum [10]. Therefore, any structural or local environmental properties that could affect the rotational motion of the radical in EPR time scale can be detected by EPR spectroscopy.

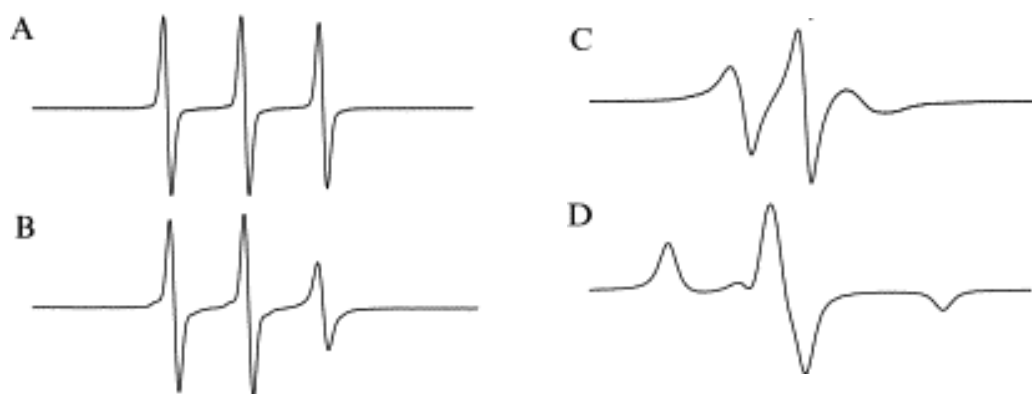


Figure 1-6 X-band EPR spectra sensitivity to the motion of the radical: A) MTSL in solution (fast motion) B) MTSL bound to a small peptide in solution, C) The same spin labeled peptide in B folded in a helix and D) a spin labeled peptide in frozen sample.

In this work, we employed X-band and W-band EPR to investigate the dynamics and electrostatics of vesicles (Chapter 3) and confined lipid bilayer (Chapter 4). Strong interactions can be observed by continuous wave EPR (CW) in which the magnetic field changes while microwave frequency is constant. To detect the weak interactions advanced pulsed-EPR techniques were used (Chapter 5).

1.3 Pulsed-EPR

Pulsed-EPR is an advance form of CW EPR in which a series of microwaves pulses excites the electron spin and the signal induced by those pulses is acquired in the absence of any microwaves. The pulsed EPR signal is directly related to the dynamic of electron state prepared by microwave pulses. The signal processing is needed to extract the spin relaxation and spectral information. Since the electron spin relaxation time is 10^6 faster than nucleus spin, the pulses in pulsed EPR have to be 10^6 times shorter than that of NMR [11].

In pulsed EPR, spin packet magnetization, an ensemble of many identical and noninteracting electron spins, is used to explain the pulse sequences and it can be defined by vector models as a vector sum of all the individual magnetic moments. The electron spins precess about external magnetic at the Larmor precession frequency [11]. The sum of individual magnetic moments, magnetization (M_0), is shown in Figure 1-7.

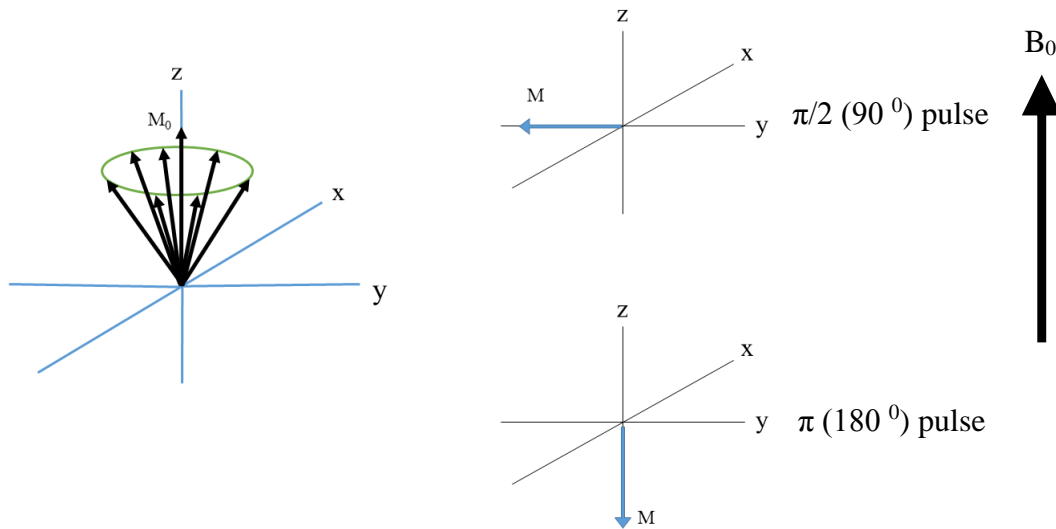


Figure 1-7 Vector model representing magnetization vector aligned with z -axis in the presence of magnetic field (B_0); and after π (180°) and $\pi/2$ (90°) pulses.

Additional field, B_1 , is required for applying pulses and it is much smaller than B_0 . The angle of the pulses respect to the z -axis determines their type; for example, the most common pulses are π and $\pi/2$ pulses which are shown in Figure 1-8. The sample is perturbed from thermal equilibrium by applying B_1 pulses, and then the magnetization returns to its equilibrium by relaxation process. Z -component of magnetization relaxes to its thermal equilibrium with time constant T_1 (spin-lattice relaxation) and M_x and M_y precess around z

axis while decaying to zero with relaxation time T_2 (spin-spin relaxation). The relaxation along x-y plane generates a signal called Free Induction Decay (FID). FID is a time domain signal and using Fourier transformation, frequency domain spectrum is obtained. Figure 1-8 shows how a single pulse can produce an EPR signal [11].

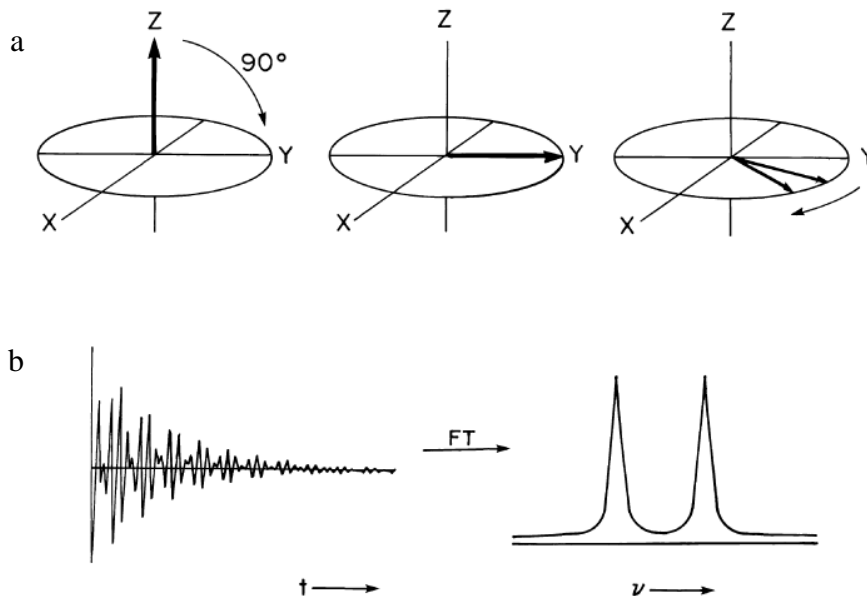


Figure 1-8 Single $\pi/2$ pulse EPR: a) decay of magnetization along x-y plane after $\pi/2$ pulse, b) FID converted to corresponding EPR spectrum by Fourier transform (adopted from ref[12]).

It is not possible to detect FID signal right after the pulse, and there is a dead time due to instrumental limitations. To overcome this limitation, multiple pulsed EPR are employed. After time “ τ ” from the first pulse, the second pulse is applied to regenerate the dissipated signal from the first pulse and it eventually produces the “echo”. First pulse ($\pi/2$) rotates the magnetization from z axis to y, following by de-phasing in x-y plane in interval time, τ . The second pulse inverts the M_y from y to $-y$ resulting in converting de-phasing spin motions

toward equal phasing motions and the echo builds up and then decays. These pulses are usually called excitation and refocusing pulses respectively [12].

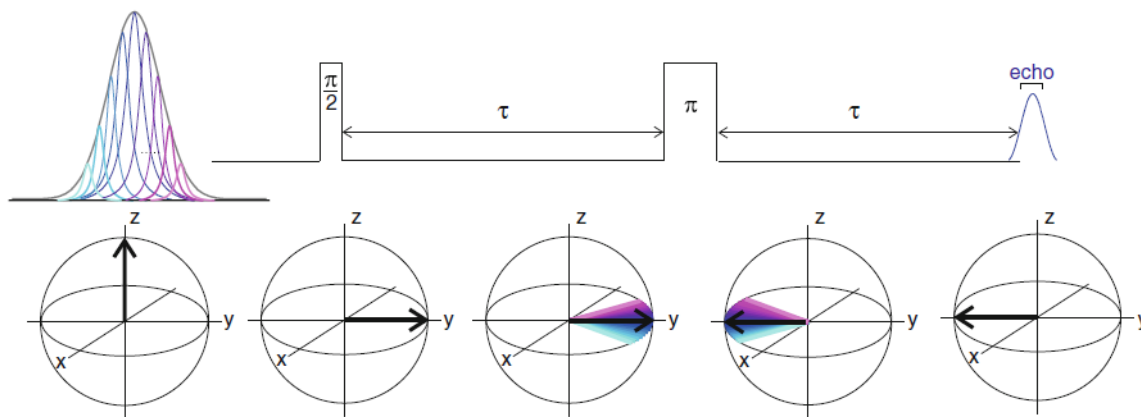


Figure 1-9 Two-pulse spin echo sequence; a $\pi/2$ pulse followed by a π pulse to generate signal (acquired from ref [13]).

HYSCORE (HYperfine Sub-level CORrElation), ESEEM (Electron Spin Echo Envelope Modulation), pulsed ENDOR (Electron Nuclear Double Resonance) and DEER (Double Electron-Electron Resonance) are some of the pulsed-EPR techniques and from those, HYSCORE and ESEEM were used (Chapter 5) to study hydrogen bonding and water penetration into lipid bilayers, therefore the basic introduction of those two techniques are provided here.

1.3.1 ESEEM

The principle of this technique is that the intensity of an electron spin echo is modulated by the transition frequencies of interacting nuclear spins. Decreasing the spin echo height at any point is measured as a function of the interval time, τ , between pulses. The plot of the

intensity versus τ yields to a complex superposition on a decay curve which is superimposed modulation onto the envelope. Echo intensity trace consists of some oscillations and their frequencies correspond to the nuclear spin transition frequencies, because this modulation comes from hyperfine interaction with nuclear spin moment, however it is only observed when anisotropic interactions are present. Hence, ESEEM spectroscopy is limited to the frozen or solid state samples where the couplings are anisotropic. ESEEM is able to provide some useful information about the weak interaction of neighboring nuclei with radical. The echo signal is maximum when π and $\pi/2$ pulses are applied and it provides the information about the nuclear-transition frequencies which eventually leads to hyperfine and nuclear quadrupole interactions. Information about the local charge densities can be obtained from quadrupole splitting and electron spin distribution [12, 14].

Two-pulse ESEEM depends on T_2 (electron spin-spin relaxation) which is usually very short resulting in boarder signals, but three-pulse ESEEM provides narrower signals because of T_1 dependency. In three-pulse ESEEM, an additional pulse is applied at the time T after the second pulse and the echo is recorded versus an increase of T (Figure 1-10) [12, 15]. We employed three-pulse ESEEM to study the interaction of water molecule with a nitroxide radical.

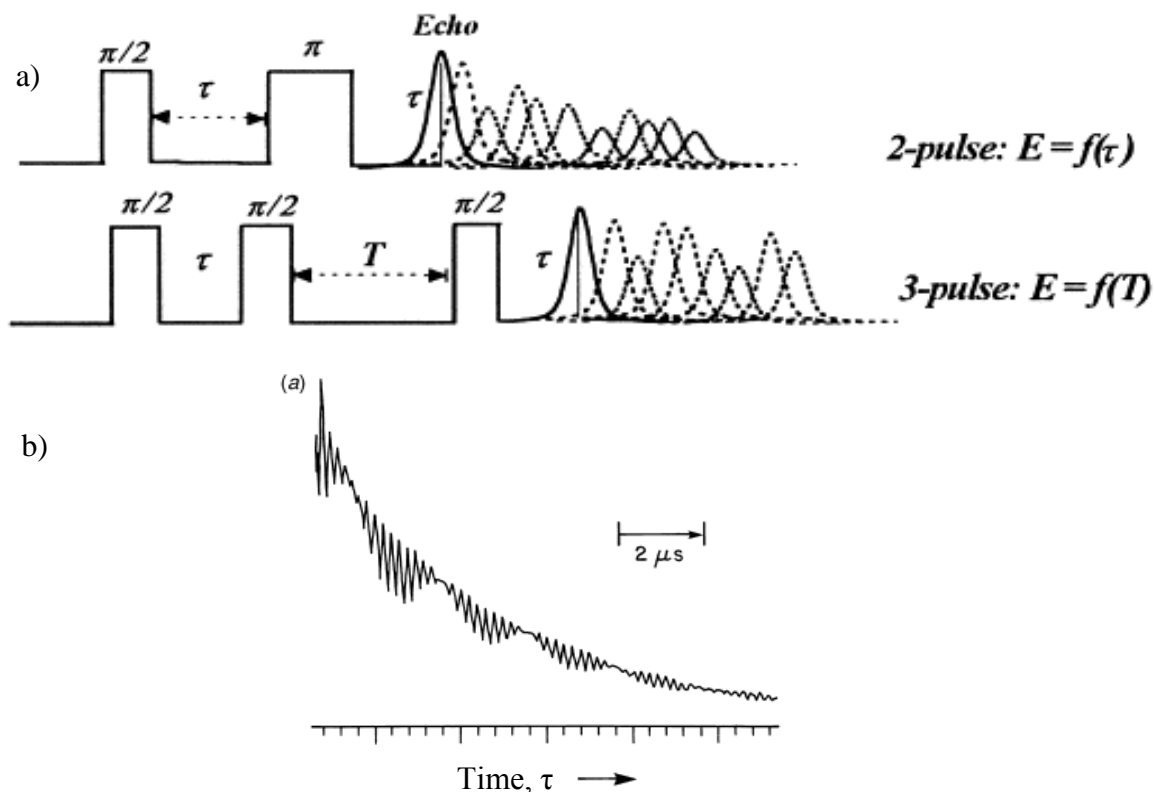


Figure 1-10 a) Pulse sequences for two and three-pulse ESEEM; at the time τ after the last pulse, modulation envelope is obtained. Echo is recorded while τ (for 2 pulse ESEEM) or T (for 3 pulse ESEEM) increases (reproduced from ref [15]) b) representative echo amplitude as a function of the interval between the pulses in two pulse ESEEM before Fourier transformation (acquired from ref [12]).

1.3.2 HYSCORE

To increase the resolution of a three-pulse ESEEM experiment and easier interpretation, ESEEM can be developed into a second dimension. HYSCORE is a two dimensional form of the three-pulse ESEEM in which the evolution time T is divided into two parts by a microwave non-selective- π pulse (Figure 1-11) [14].

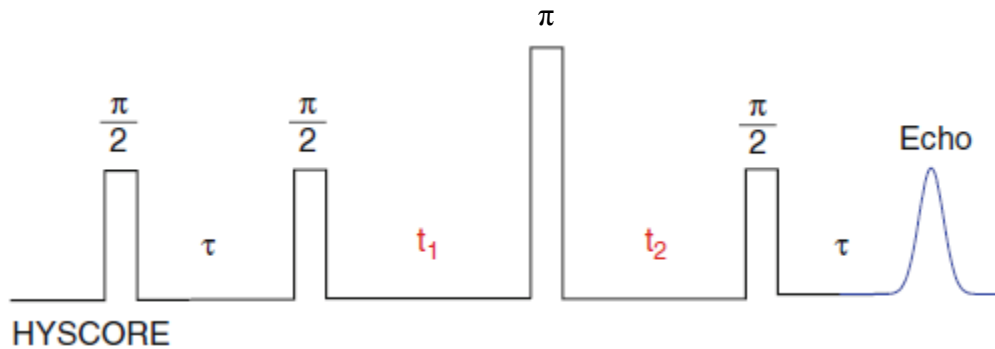


Figure 1-11 Pulse sequence for the HYSCORE technique. τ could be 30 to 500 ns [12], (reproduced from ref [14]).

HYSCORE is becoming one of the most popular 2D pulsed EPR techniques. In 1986, Hofer et al. proposed HYSCORE for the first time as a technique with capability of correlating the hyperfine sublevels [16]. The pulse sequence for HYSCORE experiments usually includes four pulses and the echo is obtained as a function of pulse separation times t_1 and t_2 (Figure 1-11).

Two dimensional Fourier transformation is applied to convert time domain HYSCORE spectrum to the frequency domain in which a pair of symmetric cross peaks with respect to the diagonal indicates a signal with two coordinates related to the nuclear spin transition frequencies in a different electron spin manifold. In HYSCORE and 3-pulse ESEEM, we are able to produce blind spots for certain frequencies, because the modulation of spin echo contains a cosine term that vanishes to zero at $\nu=2\pi n/\tau$. Therefore selecting the right time delay

(τ) is critical to observe the interaction frequencies. In addition, this might be useful to remove unwanted frequencies by placing them in blind spots [8, 14] (Figure 1-12).

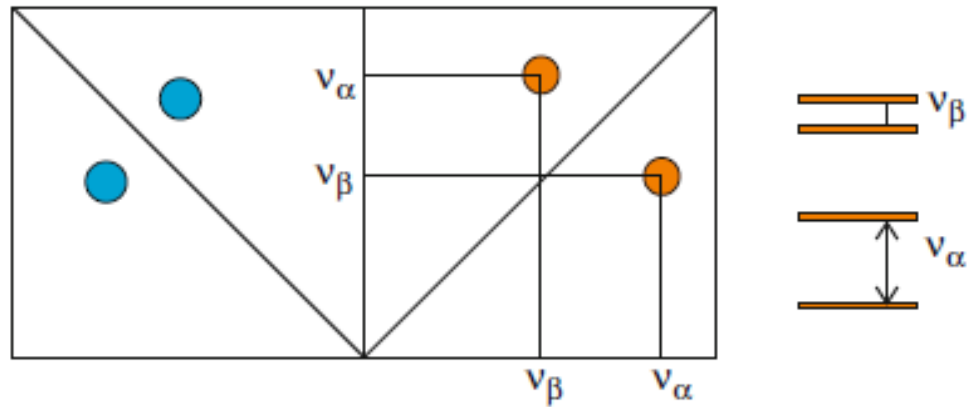


Figure 1-12 Left) A schematic HYSCORE spectrum for $I=1/2$ (nucleus). The hyperfine coupling for peaks appeared in the right quadrant is smaller than twice nuclear Larmor frequency (orange signal). If the hyperfine coupling is higher than twice nuclear Larmor frequency, signals are expected to be in left quadrant. Right) the nuclear transient states evolve in two different electron spin manifolds (acquired from ref [14]).

We employed HYSCORE to detect water molecules around nitroxide radicals inside lipid bilayers (Chapter 5).

Chapter 2. Materials and Methods

2.1 Materials

All lipids were purchased from Avanti Polar Lipids (Alabaster, AL) as chloroform solutions and stored at -80°C before use. Nanoporous membranes (AAO) were commercial Anodiscs (Whatman, U.K.) with specified pore size of 200 nm. All other AAOs were made by Antonin Marek at NCSU, chemistry department.

POPG lipid:

1-palmitoyl-2-oleoyl-*sn*-glycero-3-phospho-(1'-*rac*-glycerol) (POPG, Figure 2-1) is a negatively charged phospholipid which has been used as a model of fluid bilayer for experiments at room temperature. The main phase transition temperature of POPG is $T_m = -2^{\circ}\text{C}$.

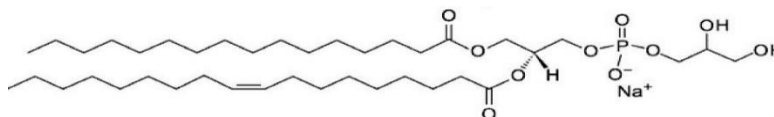


Figure 2-1 Chemical structure of POPG

DMPG lipid:

1,2-dimyristoyl-*sn*-glycero-3-phospho-(1'-*rac*-glycerol) (DMPG Figure 2-2) is a negatively charged phospholipid which has been used as a model of fluid bilayer at elevated

temperatures (48 °C) and gel phase bilayer at temperature that is slightly lower than typical ambient conditions (17 °C). The main phase transition temperature of DMPG is $T_m = 23$ °C.

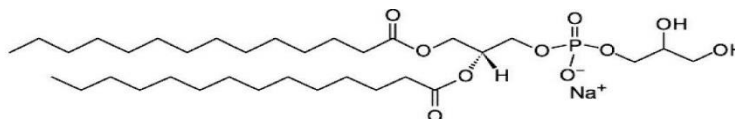


Figure 2-2 Chemical structure of DMPG

DMPC lipid:

1,2-dimyristoyl-*sn*-glycero-3-phosphocholine (DMPC) was used to study the phase transition and protein interaction. Its main phase transition is $T_m = 24$ °C.

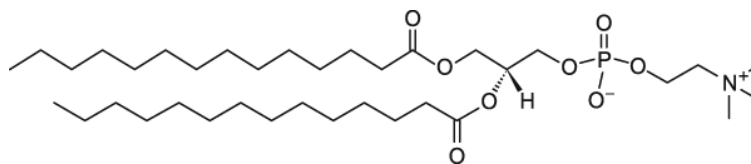


Figure 2-3 Chemical structure of DMPC

All other chemicals were purchased from Sigma-Aldrich (St. Louis, MO) or Acros Organics (Morris Plains, NJ) unless otherwise indicated.

2.2 Phospholipid Sample Preparation

2.2.1 Multilamellar Vesicle Preparation

Chloroform solutions of the desired lipids (4 ml of 25 mg/ml) with 1-2 mole % spin labeled phospholipids (e.g. IMTSL-PTE (Figure 3-4), 5PC (1-palmitoyl-2-stearoyl-(5-doxy)-

sn-glycero-3-phosphocholine) or 10PC (1-palmitoyl-2-stearoyl-(10-doxyl)-*sn*-glycero-3-phosphocholine) were prepared. Organic solvent evaporated under nitrogen gas flow yielding a thin lipid film on the surface of a 5-ml conical glass vial. Residual solvent was removed by evacuating the vial in a vacuum desiccator overnight by a rotary pump. Liposomes (phospholipid vesicles) are spontaneously formed when prepared thin lipid films were hydrated by adding 2 ml of a 50 mM phosphate buffer solution at pH = 7.0 solution (Figure 2-4). About 10 freeze-thaw cycles between liquid nitrogen and a water bath at 37 °C has been used to disrupt large aggregate of lipids and typically, the large multilamellar vesicles (MLV) with lipid concentration of ~5 w/v % are formed.

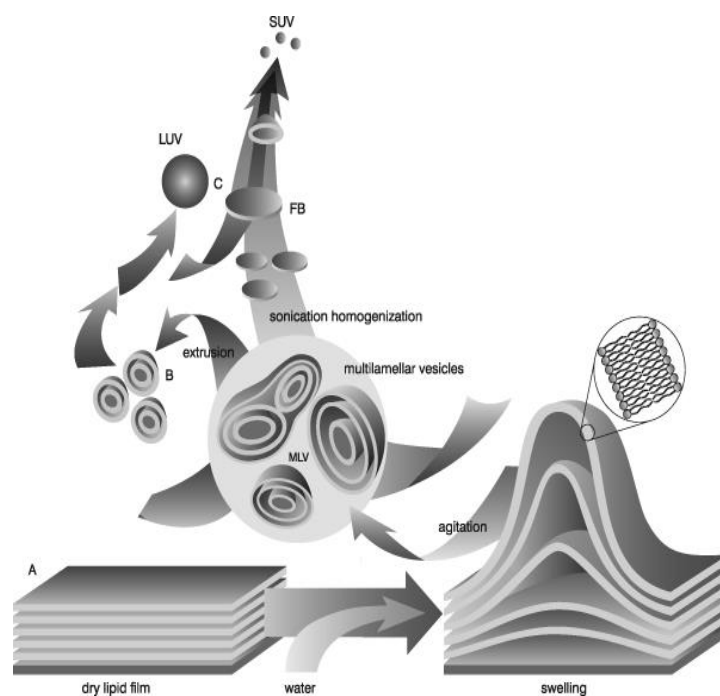


Figure 2-4 Cartoon illustrating the mechanism of lipid vesicle formation (acquired from ref [17]). SUV, LUV and MLV stand for small unilamellar vesicle, large unilamellar vesicle and multilamellar vesicles respectively.

2.2.2 Unilamellar Vesicle (ULV) Preparation

Small unilamellar vesicles (SUV) represent a good model of convex membrane surface with controlled curvature (diameter). SUVs with 100 nm diameters can be readily obtained by 10 cycles of MLVs extrusion through 100-nm nanoporous filters (Whatman, Nuclepore Track-Etched Membranes). SUVs with 50 nm diameters are prepared by extrusion of 100 nm SUVs through 50 nm filters using pressure extruder (Lipex Extruder, Northern Lipids INC. Canada). All extrusions were done at the temperature higher than phase transition temperature of desired lipid. Unilamellar liposomes can only be prepared by extrusion of multilamellar liposomal suspensions using membranes with a pore size smaller than 0.2 μ m. Liposomes obtained by passing through larger pore membranes (larger than 0.2 μ m) yield a polydisperse suspension of multilamellar liposomes.

Very small unilamellar vesicles (with diameters less than 50 nm) were prepared by sonicating the lipid suspension (5 w/v %) for 15 min with titanium tip sonicator (Misonix, Ultrasonic Processors, S-4000, USA) at 30 % power and with sequence programming of 50 sec sonication and 30 sec resting time. In order to prevent sample overheating during the sonication, the sample was placed into a 50 ml beaker filled with ice. The clear lipid suspension was then transferred to the centrifuge vial and was spun down for 30 min at 25000 \times g to remove the larger vesicles and titanium particles from sonication tip. The clear supernatant was transferred to a clean vial and diluted 20 times and characterized by dynamic light scattering (DLS), (Nano-ZS series, Malvern co, U.K) and it was later used for further experiments. For DLS measurement, diluted lipid suspension (0.25 w/v %) was placed into

polystyrol/polystyrene cuvette (10*10*45 mm) to measure the vesicle size. For zeta potential measurement, the same diluted lipid suspension was inserted into a Zeta cell and using zeta mode measurement in DLS instrument the zeta potential was measured.

2.2.3 Preparation of Small Unilamellar Vesicles (SUV) Doped with Gramicidin A

4 ml of 25 mg/ml chloroform POPG or DMPG solutions were mixed with 500 μ l of 400 μ M THF solution of gramicidin A (an ion channel peptide) to produce 1 to 3 gramicidin channels per vesicle. Organic solvents were partially removed under nitrogen gas flow. Lipid thin film was obtained by evacuating the vial in vacuum desiccator overnight. The multilamellar and unilamellar vesicles were prepared as described earlier in sections 2.2.1 and 2.2.2.

2.2.4 Nanopore Confined Lipid Bilayers Preparation

We employed two approaches to prepare nanopore-confined lipid bilayers:

1) A diluted (5 w/v %) lipid vesicle suspension in phosphate buffer at pH=7.00 (5 ml) was slowly (1 ml / min) passed through a hydrated AAO substrate using Syringe Lipid Extruder (Avanti Polar Lipids, Alabaster, AL). Typically, up to ten passes have been applied. The deposited lipids on Anodized aluminum oxide (AAO) were washed with one pass of phosphate buffer (pH=7.00) to remove the debris of the lipid.

2) A 10 w/v % lipid suspension (4 ml) was portion-wise deposited on both sides of AAO substrate placed on a pre-warmed (30 °C) hot plate. After the deposition was over, the

lipid debris stuck to the AAO surface were removed by briefly sonicating the sample with an excess of phosphate buffer (pH=7.00) in a bath sonicator at room temperature at the lowest power setting. After the sonication, the sample was subjected to 10 consecutive freeze-thaw cycles.

2.3 CW-EPR Measurements

Aqueous samples were drawn into polytetrafluoroethylene tubes (0.81 - 1.12 mm, Jaguar Industries, Stony Point, NY). Continuous-wave X-band EPR spectra were recorded at desired temperature by a Varian E-109 (Palo Alto, CA) spectrometer interfaced to a PC and digitized to 2048 data points. In the case of low temperature measurement, the sample in EPR tubes was placed inside a finger quartz dewar filled with liquid nitrogen and the spectra were then recorded at 77 K.

The AAO and nanopore confined lipid bilayer (AAO-lipid) were placed into microslides (0.4*8.0 mm I.D., VitroCom Inc. USA, NJ) and X-band EPR spectra were recorded.

2.4 Differential Scanning Calorimetry (DSC)

The thermal properties of the lipid were measured on a DSC (TA, Q2000). 5 μ l of lipid suspension (5 w/v %) was sealed in an Alod-Al Hermetic pan and was equilibrated for 15 min at 5.00 °C. The temperature was increased at 2 °C/min to 40°C and DSC trace was recorded.

2.5 Zeta Potential Measurement, UV-Vis and CD Spectroscopy of AAO

To measure the zeta potential for AAO pieces, the AAO slides (11 mg) were crushed down by mortar and pestle and suspended in a 10 ml phosphate buffer (50 mM, pH=7.4). The suspension was later inserted into a zeta potential cell and its zeta potential was measured by DLS instrument. The zeta potentials in various pH were obtained by titrating the AAO suspension with HCl (100 mM).

For UV-Vis and CD spectroscopy, the large AAO pieces were placed between two quartz cells and small ones were attached to a plastic slide by soldering up to 600 °C (Weller Soldering Station, WESD51, NC, USA). The AAO was kept wet by DI water during UV-Vis spectroscopy (Hewlett-Packard/ Agilent 8453 spectrophotometer, USA) and circular dichroism (CD) spectroscopy (Jasco J-815 CD Spectrometer). In CD spectroscopy and some cases in UV-Vis spectroscopy where UV range is the interest region, a black paper with a pinhole was attached to the surface of quartz cuvette (1 mm) to avoid light scattering (Figure 2-5).



Figure 2-5 Quartz cuvette (1 mm) used to measure CD and UV-Vis spectra for AAO based samples: a black paper attached to cuvette with a pinhole helps to avoid light scattering.

2.6 Quartz Crystal Microbalance (QCM) Measurement

Aluminum quartz crystal was anodized by Antonin Marek (NCSU, chemistry department) and characterized by water vapor adsorption/desorption isotherm. The isotherm was obtained by QCM installed to a vacuum chamber. The crystal resonant frequency and the conductance voltage from the controller output were measured using a QCM100 (Stanford Research Systems, Sunnyvale, CA, USA) quartz crystal microbalance system. A LabView (National Instruments, Austin, TX) PC-based data acquisition system was used to acquire water adsorption/desorption plot at 22 °C. The adsorption plot was obtained by opening the needle valve attached to the vacuum chamber where the quartz crystal was kept in vacuum. For the desorption plot, the same needle valve was used to decrease the pressure inside the chamber. Liquid nitrogen bath was used to desorb water vapor from chamber to obtain desired pressure in the desorption path.

QCM-AAO deposited with DMPC was prepared by adding 200-300 µL of DMPC lipid suspension (15 w/v %) to cover the AAO-QCM while crystal was kept at 30 °C. The deposited QCM-AAO was bath sonicated for 15 min and brushed with cotton tips to remove extra lipids. The lipid deposited QCM-AAO was stored at 4 °C when it is not used. Specialized Teflon holder was used to collect QCM data in solution and one side of crystal (lipid deposited side) was exposed to the solution. QCM v2.2 data acquisition software (written by Antonin Marek, NCSU) was used to record quartz crystal frequency and voltage in solution.

2.7 HYSCORE and ESEEM

HYSCORE and ESEEM spectra were recorded at cryogenic temperature. The sample was placed into a X-band EPR tube and later was shock frozen in liquid nitrogen and then transferred to the pre-cooled cavity at 78 K. Depending on the type and the purpose of the measurement, the time delay of 222 ns and 444 ns were used for HYSCORE and ESEEM. POPG vesicles labeled with 1 mole % 5PC (1-palmitoyl-2-stearoyl-(5-doxyl)-*sn*-glycero-3-phosphocholine) and 10PC (1-palmitoyl-2-stearoyl-(10-doxyl)-*sn*-glycero-3-phosphocholine) were used to investigate the water penetration into the lipid bilayer. The lipid/label mixture was hydrated with a phosphate buffer prepared with deuterated water (pH=7.4). D₂O/diglyme and CH₃OD/diglyme systems with 2 mM TEMPOL (4-hydroxy-2,2,6,6-tetramethylpiperidin-1-oxyl) were used to study the hydrogen bonding by HYSCORE and ESEEM.

2.8 pH Adjustment in Vesicles

Approximately 70 μ l of lipid dispersion (20 mg/ml) was placed into a 1.5-ml Eppendorf tube and pH of the solution was adjusted by titration with a 0.05 M HCl solution or a 0.1 M NaOH solution. The pH was measured by an Orion pH electrode 98 series (Thermo Scientific, Beverly, MA) at the temperature of the EPR experiment. The pH meter was calibrated at the temperature of the EPR experiment.

2.9 pH Adjustment in Lipid Nanopore Confined Bilayer

Nanopore-confined bilayers were placed into a desired buffer solution (5 ml) with required pH for 20 min to ensure complete pH equilibrium.

2.10 Oxygen Permeability

70 μ l of the freshly prepared lipid vesicles (5 w/v %) labeled with 1 mole % of 5PC (1-palmitoyl-2-stearoyl-(5-doxyl)-*sn*-glycero-3-phosphocholine) was placed into EPR polytetrafluoroethylene tubes and kept under nitrogen flow (3.5 LPM, 1 atm) and after 20 min X-band EPR spectra were recorded. The gas flow was then switched to the oxygen flow (3.5 LPM, 1 atm) and the X-band EPR spectra were recorded after 20 min.

2.11 Reduction of Spin Labeled Phospholipid: Kinetic Study

The freshly prepared vesicles (5 w/v %) labeled with 1 mole % IMTSL-PTE were placed in a 1.5-ml eppendorf vial and mixed with sodium ascorbate at pH=7.4 (in a 1:100 IMTSL-PTE to ascorbate ratio) and immediately transferred to a EPR Teflon tube and X-band EPR spectra were recorded versus time. The temperature of the cavity was set to the desired temperature using the Varian E-109 temperature controller attachment for low temperatures and a circulator (PolyScience 9710, USA, IL) for high temperatures.

2.12 Partitioning into Lipid Bilayers

100 μL freshly ULVs containing 80 μL TEMPO (2,2,6,6-Tetramethylpiperidin-1-yl)oxyl)) was placed and kept in an eppendorf vial for 20 min. The X-band and W-band EPR spectra were recorded at room temperature.

2.13 The Cytochrome C/Poly Glutamic Acid Layer Deposition

AAO (25mm, thickness: 64 micrometer, pore diameter: 75nm) made by Antonin Marek at NCSU (Chemistry department, Smirnov's lab) was placed and fixed into an extruder. AAO was washed by passing 10 ml deionized water using syringe pump (1 ml/min). The phosphate buffer (pH=7.4, 10 mM) solution of cytochrome c (1 mg/ml) was then passed through AAO using syringe pump (0.5 ml/min) to absorb the first layer of cytochrome c and after passing 10 ml deionized water (1 ml/min), it was dried out under nitrogen flow for 15 min. The phosphate buffer (pH=7.4, 10 mM, 10 ml) solution of poly glutamic acid containing 0.1 M NaCl, was injected into the nanoporous AAO (0.5 ml/min) to create the second layer. The membrane was then washed with 10 ml deionized water (1 ml/min) and dried out under nitrogen flow for 15 min. The extrusion process was cycled three times in order to make three layers of cytochrome c/poly glutamic acid.

The AAO/ cytochrome c/ poly glutamic acid for each cycle was placed between two quartz plates and 1 ml of deionized water was added in between to keep the sample wet during measurement. The UV-Vis spectrum for each cycle was then recorded as described earlier in section 2.5. The UV-Vis spectrum of AAO without any deposition was obtained for the

reference. The quartz plates with deionized water in between was selected as a blank for this measurement.

2.14 Melittin Interaction with Lipid Bilayers

The QCM-AAO deposited with DMPC lipid was placed in a QCM crystal holder. The crystal was immersed into a 100-ml beaker containing 40 ml deionized water and its frequency and voltage change were recorded versus time. After one hour to reach the equilibrium, a 300 μl of melittin solution (5 mg/ml) was added into the beaker and the frequency was recorded every 10 sec for about 10 hr after the addition of melittin.

Chapter 3. Electrostatic, Phase Properties and Dynamics of Phospholipid Vesicles

3.1 Introduction

Charged lipids play critical roles in many biological phenomena. For example, phosphatidylserine is a negatively charged phospholipid at body pH (pH=7.4) and it is mostly located in inner leaflets of cellular membranes. About less than 10 percent of the membrane phospholipids in platelets cell membrane are phosphatidylserine lipids [18]. These lipids play an important role in blood coagulation in case of injury. Coagulation cascade depends on the number of the phosphatidylserines in outer leaflets where the binding of activated platelets to the prothrombinase complex needs to occur (these lipids flip-flop to the outer leaflet in case of injury) [19, 20]. It has been reported that the presence of negatively charged lipids (Phosphatidylglycerol (PG) lipids) in a bilayer facilitates an insertion of charged peptides [21]. In this work we use the negatively charged lipid vesicles to investigate the surface electrostatics, molecular rotational dynamics and the lipid bilayer phase properties.

Among many interactions involved in protein-lipid binding such as a hydrophobic interaction, hydrogen bonding, and an interaction through salt bridge, electrostatic interactions play the key roles in lipid-protein associations [22-24]. Membrane excitability and insertion of membrane active toxins are some of the phenomena that can be influenced by local electrostatic potentials [25]. Electrostatic interactions affect the conformation and function of many molecules and also control intercellular and intracellular recognition and transport [26].

Because of these very important roles, it is imperative to develop and measure lipid bilayer electrostatic potential at well-defined positions with respect to the bilayer-water interface to order to further decipher the mechanisms of electrostatically-driven biological phenomena in cells.

In lipid bilayer membranes the charge on the surface creates the electric field. Fluidity or the structure of the membrane depends on the fields created by surface charges. Transport of a charged or polar molecule through the membrane can be governed by electric fields. Long range columbic electrostatic fields promote gathering the counter ions close to membrane and repulse the solutes with the same charges [27].

Three contributions to the electrical potentials across the membrane and their potential profiles across the membrane are shown in Figure 3-1. The main assumption for such a model is that the potential is coming from the fixed charged or oriented dipoles. The surface electrostatic potentials (Ψ_s) arise from charges fixed at the membrane solution interface or, in other words, it is resulted from charges bound to the membrane-solution interface. Ψ_d and $\Delta\Psi$ are dipole potentials and transmembrane potentials, respectively. The transmembrane potential is in the order of 300 mV [28].

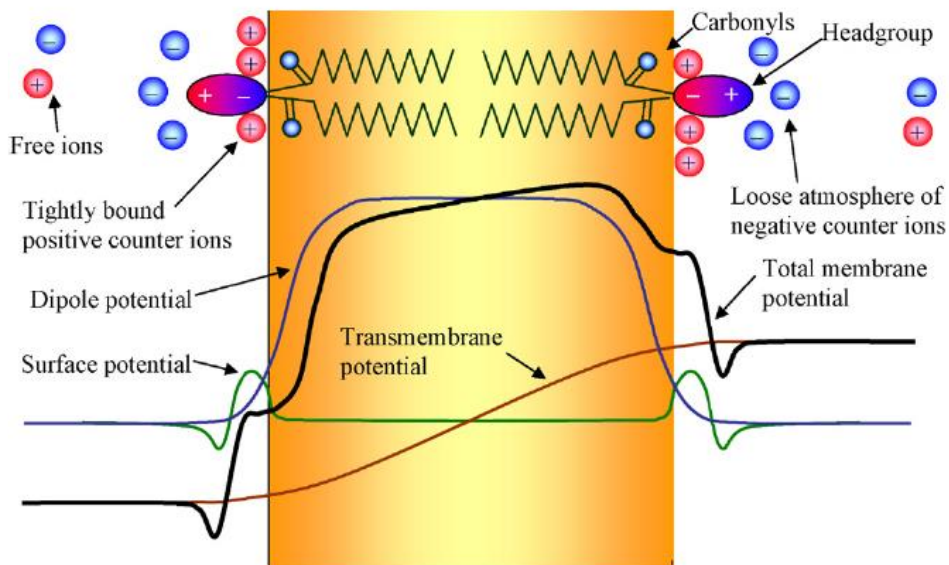


Figure 3-1 Electrostatic potentials across phospholipid bilayers; the surface potential Ψ_s due to charged groups at the interface, the transmembrane potential ($\Delta\Psi$) results from the net separation of charge across the membranes, and Ψ_d is the membrane dipole potential which is due to molecular dipole layer at the membrane-solution interface. Reproduced from ref [29].

Surface potential is an important factor for adsorption of extrinsic proteins [25]; it indicates the difference between the electric potential of membrane surface and the bulk aqueous solution. The surface potential is much smaller than the transmembrane potential and plays an important role in controlling enzymatic components of the second messenger system such as protein kinase C, in which the surface potential is controlling the binding the proteins to the membrane surface [28]. It has been shown that negative surface electrostatic potentials promote the protein to fold at the surface of membrane and cause an insertion of the protein into the lipid bilayers [30].

The source for the surface electrostatic potential in biological systems is discrete electrical charges on the surface of membrane. The acidic phospholipids, gangliosides and membrane protein are carrying these charges. Adsorption of various charged molecule or ions onto the surface of the membrane is another contribution to the membrane surface charge. These charges on the surface induce the electrostatic potential in the adjacent aqueous environment [31]. Electrical potential at the surface of membrane affects the concentration of ions in the immediate vicinity to the membrane surface. For charged phospholipids, the ions adjacent to the membrane form a “diffuse double layer” (Figure 3-3) [32]. The surface electrostatics of lipid bilayer determines the repulsive force between two membranes [33].

In the past several analytical methods have been employed for determining electrostatic parameters of lipid bilayer membranes. Currently, NMR [34], fluorescence spectroscopy [31, 33, 35], interaction force measurement [36], electron-electron double resonance (ELDOR) [37] and electron paramagnetic resonance (EPR) [38-40] are the most widely used techniques for such biophysical studies.

Spin label EPR method is a common biophysical method for studying biological system including cellular membranes. Sensitivity of EPR allows for measurements at relatively low concentrations of EPR-active label molecules per lipid (typically from 1:100 to 1:300) so the molecular probes would not alter the lipid bilayer electrostatic surface potential and other properties. In addition, in systems where the optical methods are at a disadvantage, such as studying of photosensitive and opaque systems, EPR is a feasible method to study electrostatics.

Spin probe is a small molecule bearing an unpaired electronic spin that gives a distinct EPR signal. Some of such probes can be bound to the external surface of the lipid bilayer while other will remain in solution (Figure 3-2) [41]. Typically, charged molecular probes are used in EPR studies of the lipid bilayer interface. The partition coefficient of such probes between the lipid and the aqueous phases is dependent upon the surface electrostatic potential [42-44]. Partition coefficient can be determined from an analysis of EPR spectra and then the surface potential is derived from the Boltzmann equation (Eq. 3-1). However, the main problem of this method is that the exact location of spin probe with respect to lipid bilayer surface is unknown [41, 45, 46].

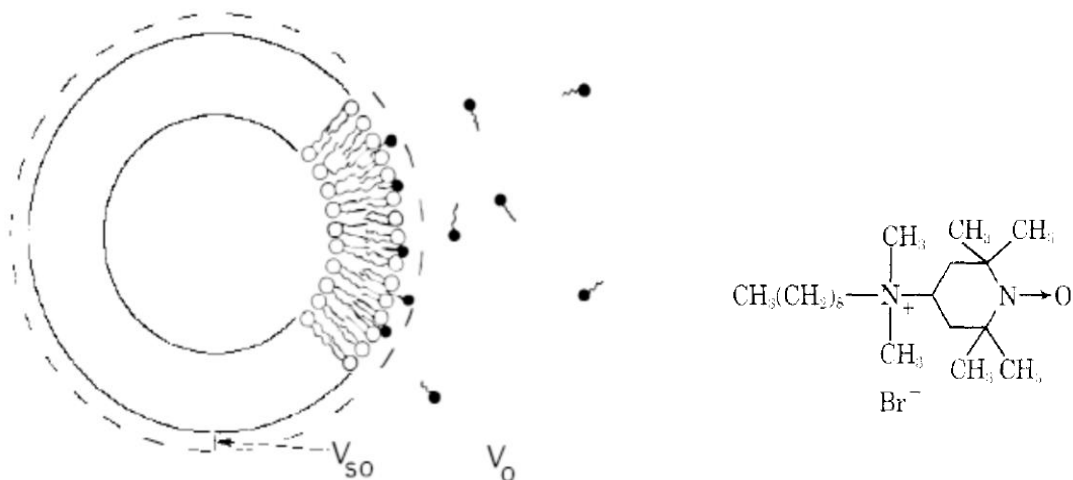


Figure 3-2 A cartoon shows the association of spin probes with the surface of lipid bilayer. Chemical structure of the probe, *N,N*-dimethyl-*N*-nonyl-*N*-TEMPOylammonium bromide is shown. Reproduced from ref [41].

EPR is very sensitive method to the rotational motion of the nitroxide probe (see Chapter1. General introduction). The distribution of a spin probe between the membrane phase and an aqueous medium is a function of the charge density. When associated with the membrane phase, the spectral lines in its EPR are broadened relative to the free spin probe in solution. Based on the population of spin labeled molecule present in each environment , the ratio of free and bound labeled molecule can be measured by analyzing EPR spectra and then used for calculating surface electrostatic potential calculation using Eq. 3-1:

$$\lambda = \lambda_0 \exp\left(-\frac{\psi_s ZF}{RT}\right) \quad 3-1$$

where λ_0 and λ are the ratio of the bound to the free form of spin probes in the absence and the presence of a surface potential respectively [41].

Another EPR method to determine the surface electrostatic potential is based on using a pH sensitive probe, a molecule containing protonatable functionalities within the radical structure. A close proximity of ionizable groups to the radical center of the probe leads to a difference in EPR spectra of the protonated and nonprotonated forms of the radical. Imidazoline radicals are one of the most promising structures as pH-sensitive spin-probes [47].

In 1940, Harley and Rose described diphenylazo-*o*-nitrophenol as a pH probe absorbed to the charged micelles [48]. They attribute the shifts from the intrinsic *pK* to the local interfacial activity of the protons at the charged surface of micelles. The Boltzmann formula relates the observed pH shift and the interfacial electrical potential as [35];

$$a_{H^+}^i = a_{H^+}^w e^{-F\Psi/RT}$$

3-2

where, $a_{H^+}^i$ and $a_{H^+}^w$ are the activity of proton in membrane interface and water respectively.

In 1973, the first lipid pH indicator (4-heptadecylumbelliferone) based on fluorescence probe was introduced and placed into monomolecular lipid films and the effect of lipid mixtures on probe proton equilibrium was studied [49]. Consequent studies of lipid bilayer systems using such a probe remarkably large p*K* shifts for anionic lipids and, surprisingly, the shifts for even neutral lipids have been observed [35, 50].

Electrostatic surface potential of lipid bilayer can be calculated using the Gouy-Chapman theory, which predicts for the electrical potential to decrease exponentially away from the surface [35]. This theory is based on a diffuse model of the ion double layer formed at a charged surface (Figure 3-3). Dissociation of membrane-bound acid into the bulk solution is dependent upon electrostatic energy difference between the proton in the bulk aqueous media and at the interface. Surface electrostatic potential is defined as a difference between the potential at the interface and the bulk.

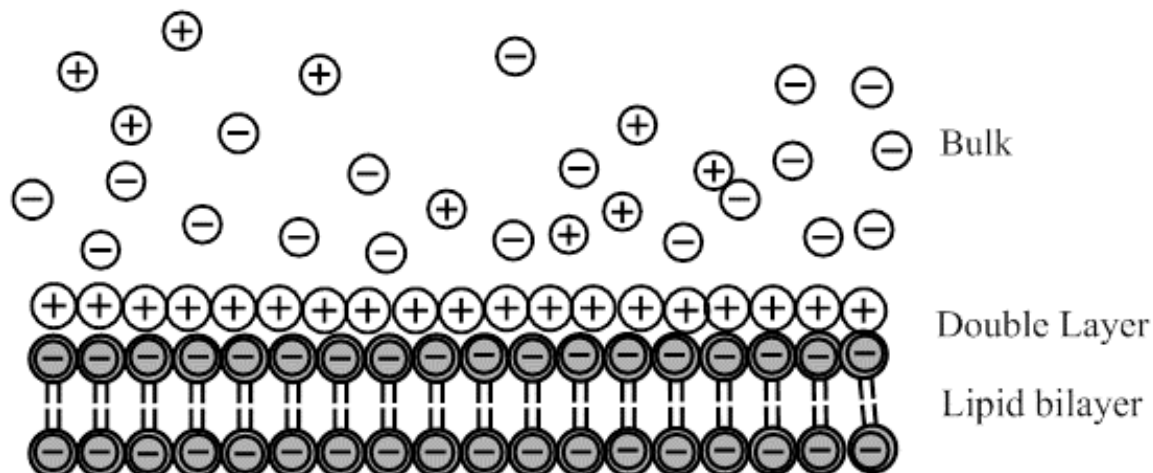


Figure 3-3 A cartoon illustrating formation of diffuse double layer formed at a negatively charged surface based on the Gouy-Chapman theory.

The difference between the interfacial pK_a^i and the intrinsic pK_a^0 of a probe depends on the amount of energy required to bring the acidic or basic form of the label from water to the location at the membrane interface. This difference includes the electrostatic potential at the surface for transferring the charges (A^+ , B^-) from bulk to the interface [35] and hydration shift due to a change in the local dielectric permeability upon transferring ions from bulk into the membrane interface.

The polarity shift or hydration shift is expected to be between 0.9 ± 0.2 of pH units corresponding to the interfacial dielectric constant $\epsilon=30$. In biological membranes such as charged glycoposomes the interfacial ϵ is about 60 to 70. Polarity induced and electrostatic pK shifts are highly temperature dependent especially for systems where the phase transition may occur during the titration [27].

Another method for evaluating bilayer electrostatics is based on observing reversible ionization of fluorescent and/or EPR molecular probes upon pH titration [51]. The first time that method was used to measure surface electrostatic potential was in 1991 [40].

In this work we used an EPR titration method described in ref [51] to access surface electrostatic potential. Spin labeled phospholipid bearing a pH-sensitive nitroxide was introduced into lipid bilayer and the pKa of the ionizable group of this nitroxide which is a function of the bilayer surface electrostatics potential determined by analyzing EPR spectra of the nitroxide affected by changes in rotational dynamics and magnetic parameters upon the probe protonation. The nitroxide radical was tethered to the lipid head group to ensure the location of spin probe at the bilayer interface [51, 52]. This spin labeled phospholipid has a lipid-like structure providing for insertion into the bilayers.

Chemical structure of synthetic spin-labeled phospholipid (IMTSL PTE) is shown in Figure 3-4. IMTSL-PTE is a pH-sensitive spin probe, and its titration results in changing the acid-base equilibrium at the interface between protonated and nonprotonated forms of the nitroxide. The protonated and nonprotonated forms have different rotational motion and those forms can be detected from EPR spectra.

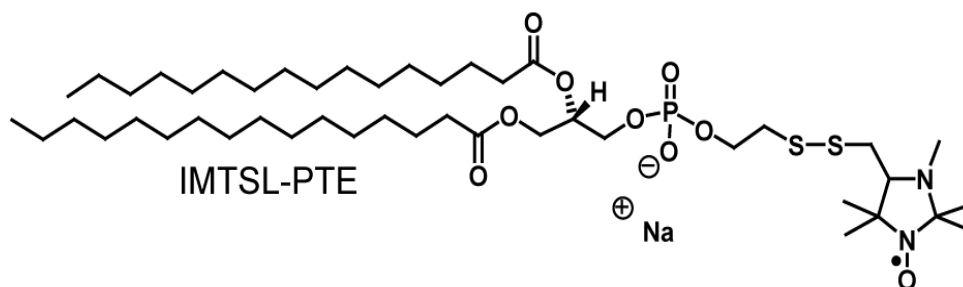


Figure 3-4 Chemical structure of a synthetic spin-labeled phospholipid (IMTSL PTE).

Many proteins are known to have strong binding preferences to curved lipid bilayer surfaces. Effect of curvature on binding has been determined by a fluorescent probe [20]. ArfGAP1, a Golgi-associated protein, a membrane-binding amphipathic α -helix is able to sense curvature and strongly prefers binding to the positively curved lipid membranes over the flat ones [53]. R. R. Middleton *et al.* studied the effect of curvature and size of POPS/POPC unilamellar vesicles (ULVs) and showed that alpha-Synuclein (a small neuronal protein) binds more strongly to higher curved vesicles (smaller vesicles). The electrostatic interaction between the negatively charged bilayer and a positively charged N-terminus of alpha-Synuclein is also an important factor in its binding to the charged lipid bilayers [54].

The property of proteins to sense membrane curvature has a number of implications in cellular processes including endocytosis, exocytosis, and vesicle trafficking as well as pathogenic processes associated with viral infections or protein aggregation disorders. However, the available experimental methods for measuring surface electrostatic potentials and associated curvature in membranes are rather limited [52]. Binding the proteins and even inserting toxins into the lipid bilayer are dependent on electrostatic interactions with lipid

bilayers. For example, membrane import of colicin channel domain can be controlled by the electrostatic potential at the interface of lipid bilayers. The rate of protein unfolding of C-terminal channel polypeptide of colicin E1 at the membrane surface increases with increasing the magnitude of the negative membrane surface potential [55]. Here we use a spin probe EPR method to measure electrostatic potentials right at the interface of lipid bilayers and provide data on effects of the membrane curvature on surface potential, phase properties, and dynamics of vesicles.

3.2 Results and Discussion

3.2.1 Dynamic Light Scattering (DLS) and Differential Scanning Calorimetry (DSC)

Dynamic Light Scattering: DLS was used to measure the vesicle size and zeta potential for every unilamellar vesicles (ULVs) in this work. The diameters reported here are Z-Average diameters that are intensity-weighted. Since one may expect larger vesicles in the sample, Z-Average diameter is usually larger than the maximum in the intensity size distribution; however, this is the most common parameter reported in the DLS literature. If the particles are assumed to be point scatterers, then Z-Average diameter ($\overline{D_z}$) can be expressed as:

$$\overline{D_z} = \frac{\sum_i N_i M_i^2 D_i}{\sum_i N_i M_i} \quad 3-3$$

where N_i , M_i and D_i are the number, weight and diameter of a particle i respectively [56].

For consistent comparison of the vesicle diameters, we used Z-average diameters for all the vesicles in this work; however, the intensity size distributions for all the samples were also obtained to check for the sample homogeneity.

Since some of the experiments were carried out at different temperatures, the size distributions upon increasing temperature were checked by measuring DLS for DMPG ULVs at different temperatures. As it is shown in Figure 3-5, the Z-average diameters do not change significantly upon increasing temperature. The size distributions get narrower but the peak

location did not change (Figure 3-5). Note that DMPG undergoes the main phase transition at $T=23\text{ }^{\circ}\text{C}$.

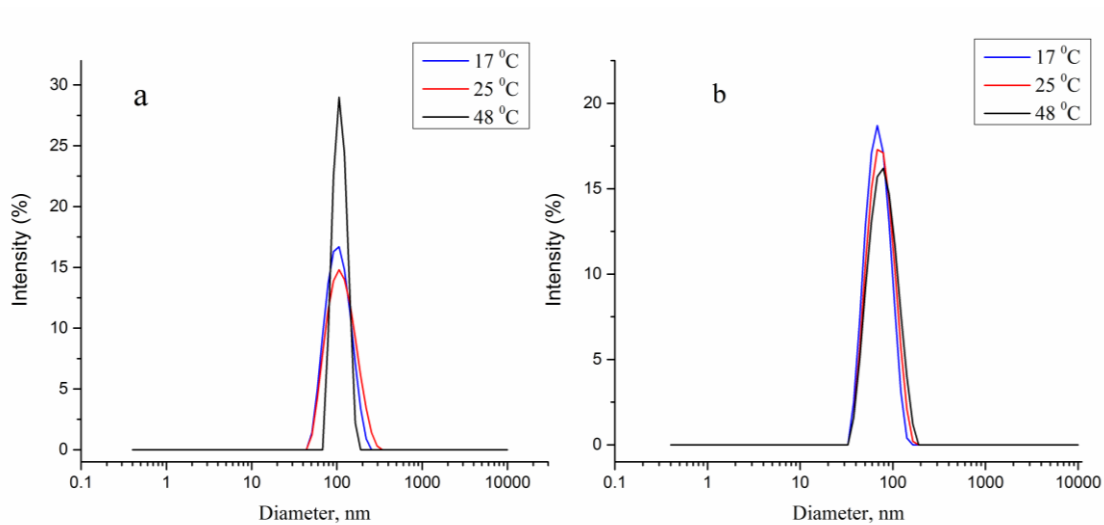


Figure 3-5 Intensity size distribution of DMPG ULVs at different temperature: a) DMPG ULVs prepared by passing through 100 nm membrane and b) DMPG ULVs prepared by passing through 50 nm membrane.

Table 3-1 Size stability of DMPG ULVs at different temperatures

Vesicle type	T, °C	Z-average Diameter, nm
DMPG passed through 100 nm membrane	17	97
	25	105
	48	109
DMPG passed through 50 nm membrane	17	66
	25	70
	48	74

In order to maintain at the temperature higher than the main phase transition temperature for DMPG ULVs, some of the experiments were carried out at 48 °C. The stability of DMPG vesicles at this temperature was investigated by tracking the diameter change of DMPG ULVs at 48 °C (Figure 3-6).

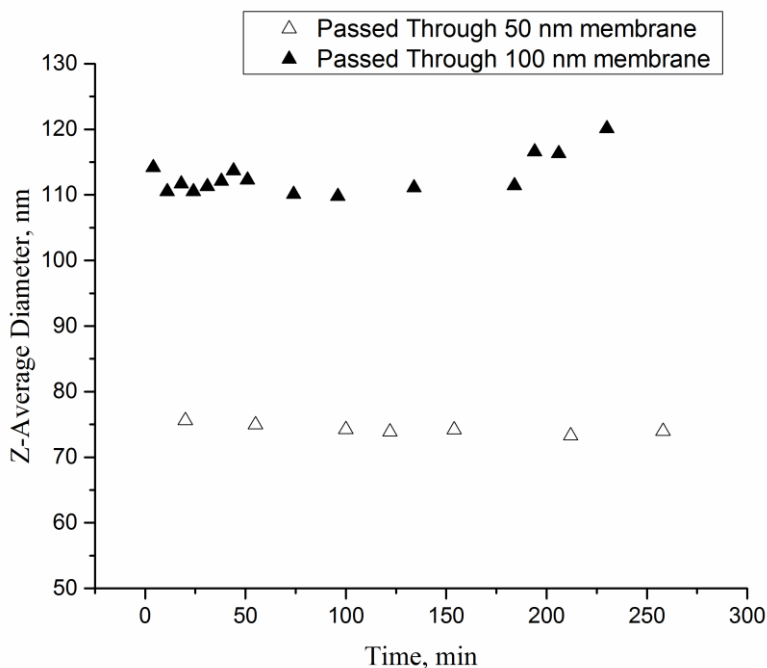


Figure 3-6 Z-Average diameters of DMPG ULVs measured by DLS at 48 °C. The DMPG vesicle concentration is 0.25% w/v.

Differential Scanning Calorimetry (DSC): DMPG ULVs undergo transition from gel phase to liquid phase at 23 °C. We investigated the main phase transition when vesicle type and diameter change. DSC traces for DMPG unilamellar and multilamellar liposomes show

the difference between the main phase transition peak in multilamellar and unilamellar vesicles (Figure 3-7).

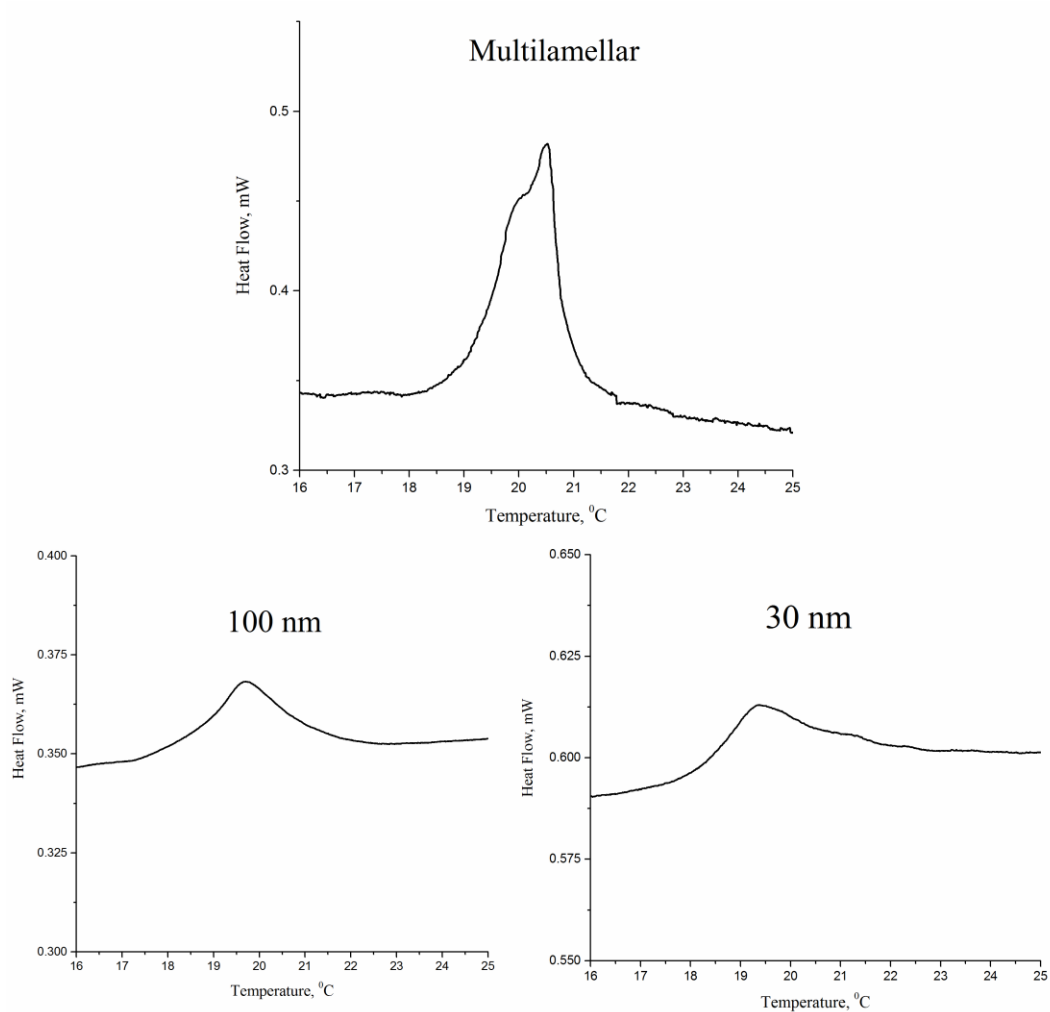


Figure 3-7 DSC traces of 5 % w/v DMPG multilamellar and unilamellar vesicles (30 and 100 nm). The DSC was performed with scan rate of 2 °C/min.

It has been reported that the main phase transition for small vesicles is broader [57] and not detectable for sonicated vesicles [58]. Our results showed that there is a phase transition in small unilamellar vesicles and it becomes broader compared to multilamellar liposomes

(MLVs), which likely due to a higher cooperativity of the transition in multilamellar vesicles. The main phase transition temperature also shifts to the lower values for ULVs.

The cooperative unit (CU) is the number of lipids undergoing phase transition and it is proportional to the width of the transition at half height of the peak [59]. CU can be calculated by following equation [60]:

$$CU = \frac{\Delta H_{vH}}{\Delta H_{cal}} \simeq \frac{4RT_m^2}{\Delta T_{1/2}\Delta H_{cal}} \quad 3-4$$

where R, ΔH_{vH} , ΔH_{cal} , T_m , and $\Delta T_{1/2}$ are gas constant, van't Hoff enthalpy, the enthalpy of the transition, the main transition temperature and the width of the transition at half height of the peak respectively. CU is directly proportional to T_m^2 and inversely to $\Delta T_{1/2}$, therefore, the broader DSC traces (higher $\Delta T_{1/2}$) and smaller T_m are indicative of a less cooperative phase transition.

For smaller vesicles, the peak is broader and vesicles are less cooperative and they do not undergo the phase transition at a narrow temperature range. Decrease in diameter from 100 to 30 nm showed slight increase in peak broadening as a result of less cooperative transition in smaller vesicles.

3.2.2 Surface Electrostatic Potential Measurement

pK_a of a spin probe at the lipid bilayer interface will be different from pK_a of the probe in the bulk water because of a measurable Gibbs free energy required to transfer a charged probe from the bulk aqueous phase to an interface with an electrical potential Ψ . This overall

Gibbs free energy, ΔG , has two major additive components: ΔG_{pol} , required to transfer a spin probe from a bulk aqueous solution onto an interface with a different local dielectric permittivity, ϵ , but at zero electrical potential, and ΔG_{el} corresponding to the local electrostatic potential, Ψ . Therefore, the resulting pK_a^i of a spin probe located at a charged interface is different from that of in pure water (pK_a^0) [51].

$$pK_a^i = pK_a^0 + \Delta pK_a^{el} + \Delta pK_a^{pol} \quad 3-5$$

where ΔpK_a^{pol} and ΔpK_a^{el} are polarity and electrostatic contributions, respectively [35].

The surface electrostatic potential Ψ can be calculated as:

$$\Delta pK_a^{el} = \frac{-e\Psi}{\ln(10) kT} \quad 3-6$$

where e is the elementary charge, k is the Boltzmann constant, and T is the absolute temperature.

In order to determine ΔpK_a^{el} one has to measure ΔpK_a^{pol} and pK_a^0 at required temperatures. While intrinsic pK_a^0 is typically obtained by titrating a spin probe in a buffer solution at the same ionic strength, such a procedure cannot be applied to spin-labeled phospholipids as those are essentially insoluble in water. In order to overcome the insolubility of such spin probes, IMTSL- mercaptoethanol (IMTSL-ME) adduct was used as a water-soluble model and intrinsic pK_a^0 was determined by EPR titration [52].

Specifically, EPR spectra of IMTSL-ME were measured as a function of pH and showed three well-resolved nitrogen hyperfine coupling components of almost equal peak-to-

peak height as one would expect for a small nitroxide freely tumbling in a solution. Such fast motion EPR spectra were least-squares simulated to measure the nitroxide isotropic nitrogen hyperfine coupling constant, a_N , as a function of pH. Then the intrinsic pK_a^0 was obtained by fitting experimental a_N to a modified Henderson-Hasselbalch Eq. 3-7 [52].

$$a_N = \frac{A(R\cdot H^+) + A(R\cdot)10^{pK_a-pH}}{1 + 10^{pK_a-pH}} \quad 3-7$$

where $A(R\cdot H^+)$ and $A(R\cdot)$ are the isotropic nitrogen hyperfine coupling constants for the acidic and the basic forms of IMTSL-PTE respectively (Figure 3-8).

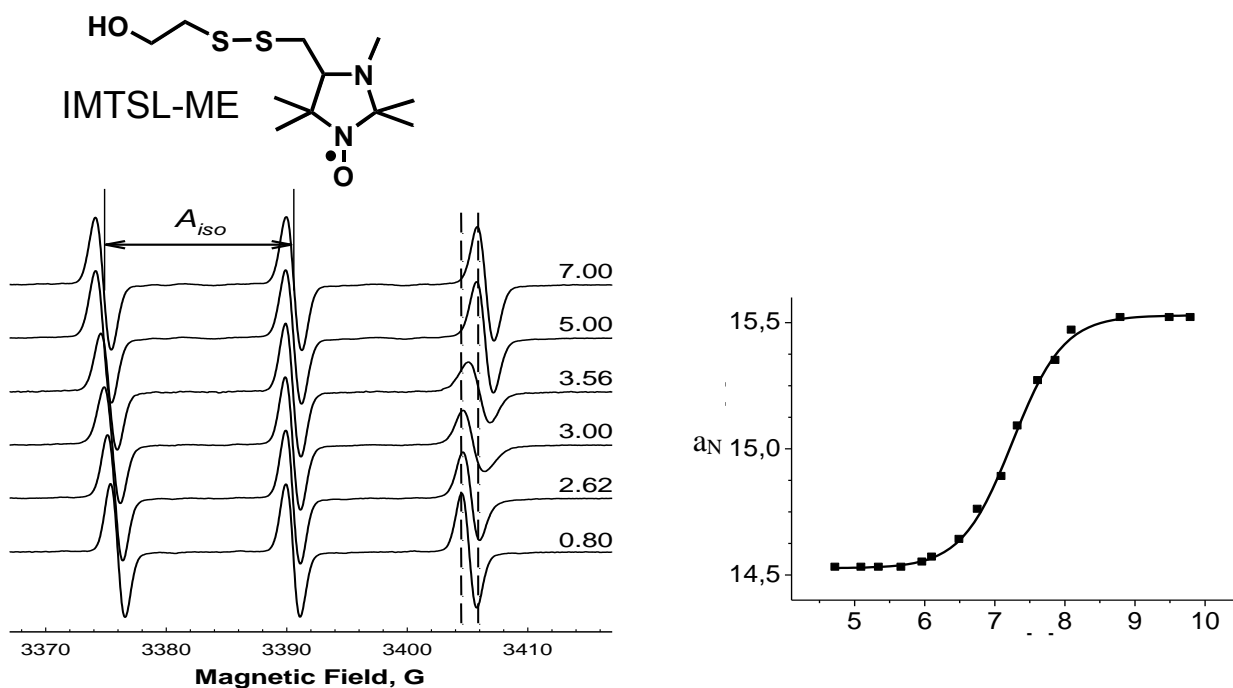


Figure 3-8 Left: Experimental X-band EPR spectra of IMTSL-ME at 17 °C as a function of pH indicated next to the spectra. Right: An EPR titration curve obtained by fitting experimental a_N (filled squares) to a modified Henderson-Hasselbalch equation shown as a solid line [52].

The intrinsic pK_a^0 was reported to be 3.33 ± 0.03 at 17°C [52]. Polarity-induced shift, ΔpK_a^{pol} , can be obtained by using an uncharged model interface that has structure similar to that of the lipid bilayers. Small surfactant Triton X-100 (shown in Figure 3-9) is considered as a good model for the fully uncharged interface and allowed the authors of ref [27] to calculate the polarity induced shift of pK_a (ΔpK_a^{pol}).

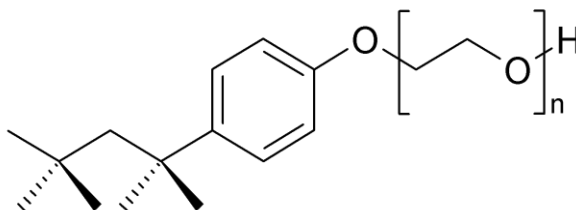


Figure 3-9 Triton X-100 chemical structure

For micelles formed with Triton X-100 and doped with 1% IMTSL-PTE, the interfacial pK_a can be calculated as:

$$pK_a^i = pK_a^0 + \Delta pK_a^{pol} \quad 3-8$$

Since there is no electrostatic contribution for Triton X-100, the only shift that can be measured is the polarity induced shift, ΔpK_a^{pol} , which was obtained at 20 and 48°C for this model and we used these values for the electrostatic potential shift calculation.

Table 3-2 Interfacial pK_a^i and polarity induced shifts measured for Triton-X-100 with 1% IMTSL-PTE [52].

T, °C	pK_a^i	ΔpK_a^{pol}
20.00 ± 0.02	2.52 ± 0.01	-0.81 ± 0.03
48.00 ± 0.04	2.39 ± 0.03	-0.94 ± 0.04

To measure the surface electrostatic potential, we used an “EPR titration” method, in which the pH-induced changes in EPR spectra of IMTSL-PTE were followed to determine the interfacial pK_a^i of its ionizable group. Electrostatics of the bilayer affects the equilibrium between charged and uncharged species, and, thus, the pK_a^0 of the probe (Figure 3-10).

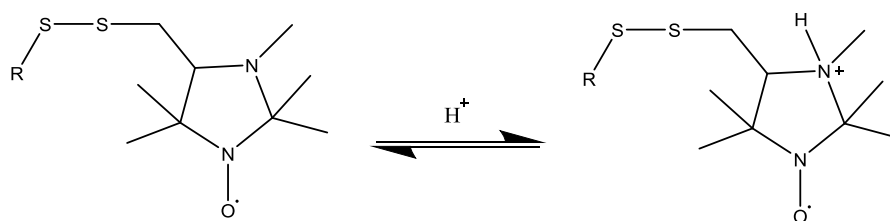


Figure 3-10 Protonation of IMTSL-PTE at the interface of vesicles.

Figure 3-11 shows two examples of representative EPR spectra obtained by titrating POPG and DMPG SUVs prepared by passing through 100 nm membrane.

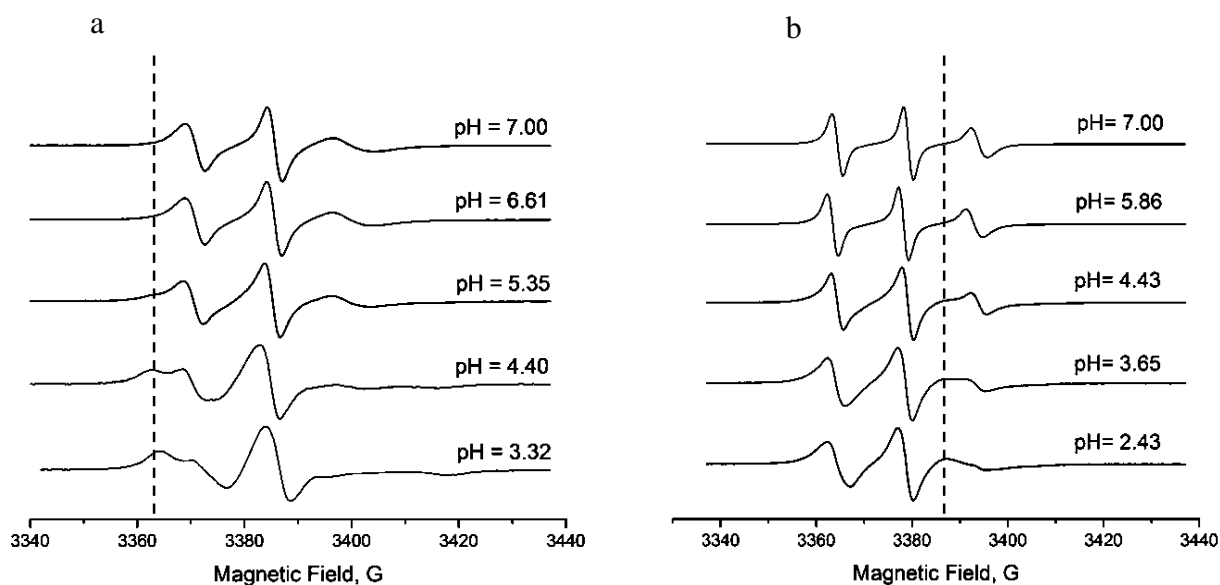


Figure 3-11 Representative X-band (9.5 GHz) EPR spectra of unilamellar phospholipid vesicles composed of a) POPG (106 nm at 17 °C), b) DMPG (112 nm at 48 °C) doped with 1 mol % of IMTSL-PTE and measured at various pH. Dashed lines represent a guide for an eye to highlight the appearance of the protonated form at lower pH.

EPR spectra of DPMG and POPG unilamellar vesicles in liquid phase doped with 1 mol % of IMTSL-PTE indicate an additional component during titration that corresponds to the protonated form of the spin probe. We relate this new spectral component with the protonated fraction of the nitroxide. This protonated form is expected to experience additional electric interactions with the negative charges of POPG at the bilayer interface causing a decrease in the probe rotational tumbling. Since EPR is very sensitive to the rotational tumbling of the probe with transition from fast to slow motion limit occurring at about 1-2 ns rotational correlation time, τ_c , the EPR spectra of protonated form are broader than that of the nonprotonated form.

Sometimes, there is a very small amount (<1%, based on the double-integrated EPR intensity) of a free (unbound) spin label in solution which appears in EPR spectra. The appearance of this small peak in the high magnetic field region can make spectra simulation less accurate; therefore, we tried to remove these unwanted EPR-active species when they appear in EPR spectra.

Two methods were used: 1) spinning down the lipid suspension and 2) dialysis, we found that spinning down the sample at a temperature that is below main phase transition of lipid vesicles is applicable to DMPG. For POPG we have to employ a dialysis of the sample to remove the free label because the main phase transition temperature for POPG is lower than 0 °C, which complicates spinning down sample the lipid sample in the gel phase while it still remains liquid. The vesicle diameter was measured after spinning down and dialysis and usually the vesicle size is stable. However if there is a change in diameter, vesicles are subjected to 10 cycles of extrusion with desired filters.

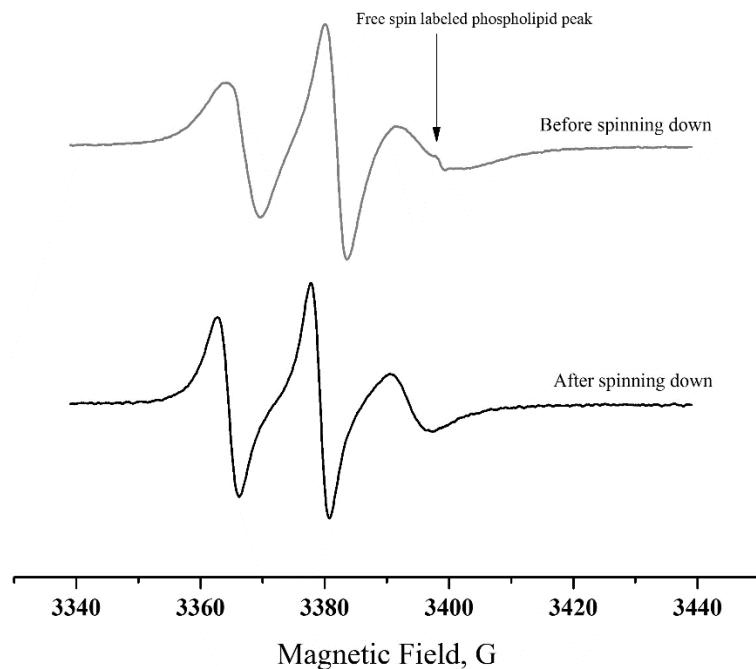


Figure 3-12. X-band EPR spectra of DMPG unilamellar 100 nm vesicles with appearance of free spin label at pH=7.00 (note the arrow) before and after spinning down.

Figure 3-12 shows EPR spectra of DMPG lipid before and after spinning down. EPR spectrum after spinning down shows that the free spin label is no longer present in the sample (arrow shows an EPR signal originating from the free label).

As it is shown in Figure 3-11 when pH is approaching pK_a of the probe, EPR spectra clearly reveal two components which are protonated and nonprotonated nitroxide forms. In order to decompose each spectrum and to determine the fraction of the protonated form, spectra simulations using the approach described by Alex I. Smirnov in ref [33] were employed. Two spectra corresponding the highest and the lowest pH have been selected as the reference spectra for the nonprotonated and the protonated forms of spin-labeled phospholipid, respectively.

Using EPR spectra of the nonprotonated and the protonated forms of the probe as the reference spectra, the experimental two-component EPR spectra acquired at intermediate pH were least-squares-decomposed into the spectra of the individual components. Figure 3-13 shows an example of a decomposition of an EPR spectrum of IMTSL-doped POPG SUVs (109 nm) at pH= 4.88 into two (protonated and nonprotonated) components. The residual of the fit (*i.e.*, the difference between the experimental (A) and the simulated (D) spectra) confirms the applicability of this slow exchange model. B and C are the experimental reference spectra scaled by amplitude to yield the spectrum in A.

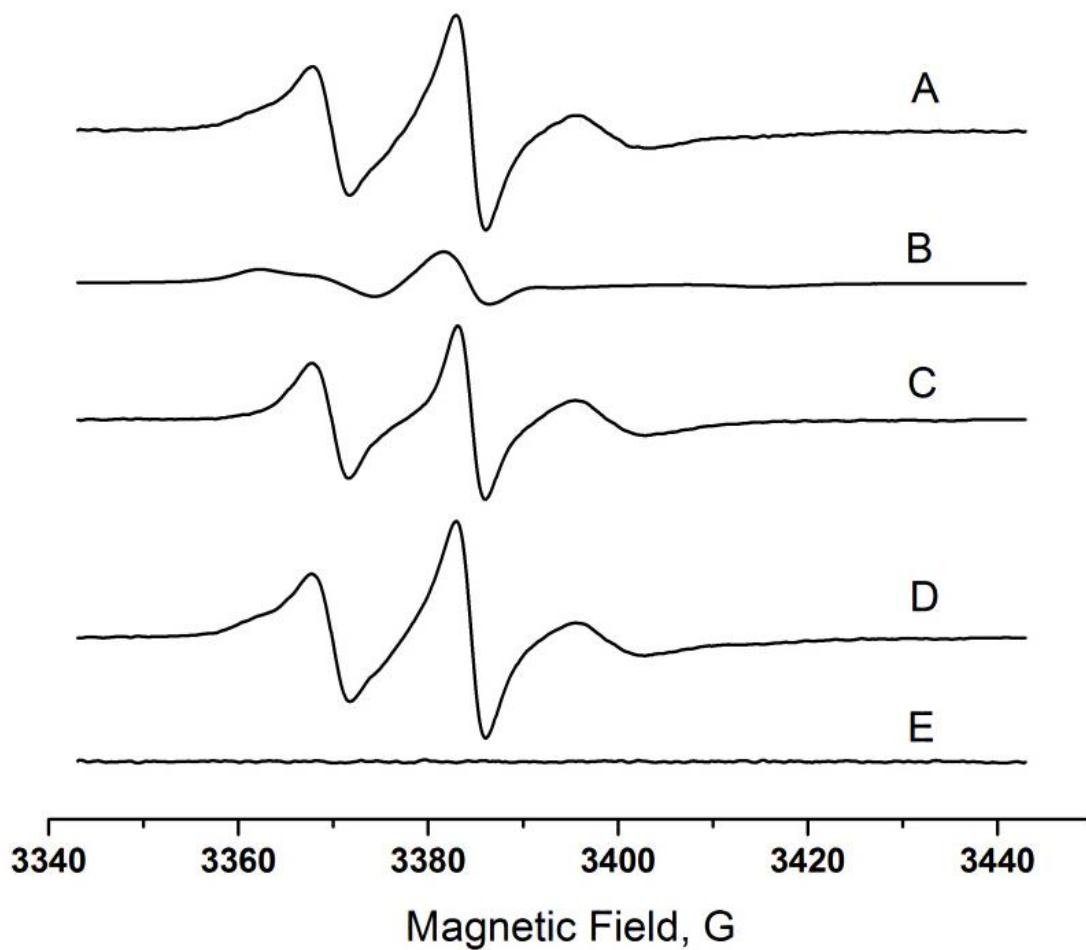


Figure 3-13 Least-squares decomposition of the experimental X-band (9.5 GHz) EPR spectrum acquired from IMTSL-PTE 1%-doped 109 nm unilamellar POPG vesicles at pH=4.88 and 17 °C. A: Experimental spectrum; Least-squares simulated spectra of (B) nonprotonated and (C) protonated forms of the nitroxide; (D) simulated spectrum; (E) residual of the fit.

Fraction f of the nonprotonated form was calculated as:

$$f = I(R)/[I(R) + I(RH^+)] \quad 3-9$$

where $I(R)$ and $I(RH^+)$ are the double integrals of the individual decomposed spectra components for the nonprotonated and the protonated forms, respectively.

Experimentally measured f (fraction of the nonprotonated form) data were plotted against pH and fitted into the Henderson-Hasselbalch equation yielding the interfacial pK_a of the nitroxide probe:

$$f = \frac{10^{(pH-pK_a)}}{1 + 10^{(pH-pK_a)}} \quad 3-10$$

Figure 3-14 shows an example of a typical fitted titration curve for POPG unilamellar vesicles with the diameter of 109 nm. The titration curves for all the vesicles were acquired with the same approach.

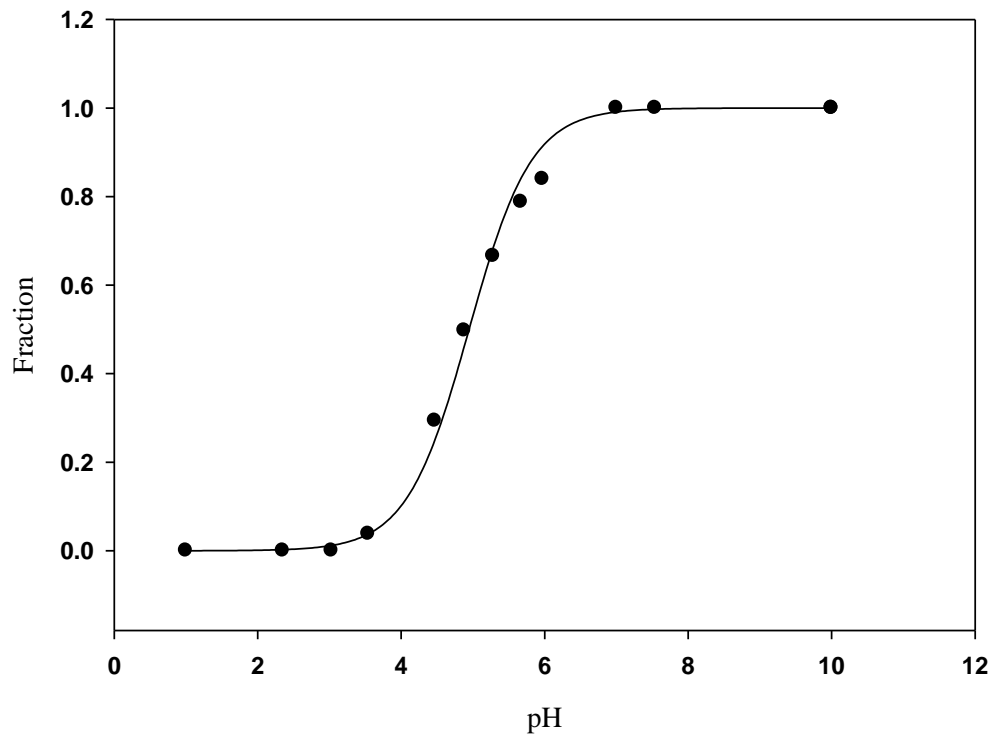


Figure 3-14 Titration curve of POPG small unilamellar vesicles (SUVs) doped with IMTSL-PTE 1% with diameter of 109 nm at 17 °C.

Using the values in ref [52] and measured interfacial pK_a^i , surface electrostatic potentials for POPG, DMPG unilamellar vesicles with different diameters were calculated by equations and summarized in the Table 3-3.

Table 3-3 Interfacial pK_a^i , polarity-induced and electrostatic shifts, ΔpK_a^{el} , measured for POPG SUVs doped with 1% IMTSL-PTE at 17 °C. Data for MLV was reported in ref [26].

Vesicle type	T	Diameter	pK_a^i	ΔpK_a^{el}	Ψ	A_L
	°C	nm			mV	nm ²
POPG ¹	17	31	5.42±0.03	2.90±0.04	-167±2	0.44±0.02
POPG ²	17	49	5.22±0.04	2.69±0.02	-155±1	0.56±0.01
POPG	17	65	5.02±0.06	2.50±0.07	-144±4	0.70±0.06
POPG	17	107	4.90±0.05	2.38±0.07	-137±4	0.80±0.06
POPG(MLVs)	17		5.49±0.03	2.97±0.05	-171±3	0.40±0.02
DMPG	17	69	5.46±0.01	2.94±0.04	-169±3	0.41±0.02
DMPG	17	107	5.44±0.03	2.92±0.05	-168±3	0.42±0.02
DMPG(MLVs)	17		5.70±0.05	3.18±0.11	-183±5	0.32±0.03
DMPG	48	78	5.08±0.02	2.69±0.05	-172±3	0.39±0.02
DPMG	48	112	4.72±0.04	2.33±0.06	-148±4	0.80±0.02

1. Titration data for POPG with 31 nm size was obtained by Maxim. Voinov.
2. Titration data for POPG with 49 nm was obtained from vesicles prepared by extrusion and sonication method and both showed the same result.

The surface area per lipid polar head group, A_L , is calculated from the Gouy-Chapman electrostatic potential equation as [61]:

$$\Psi = \frac{2kT}{e_0} a \sinh\left(-\frac{\lambda e_0^2 \sigma}{A_L 2 \epsilon \epsilon_0 kT}\right) \quad 3-11$$

Where σ is the lipid surface charge density, λ is the Debye screening length, ε_0 is the permittivity of vacuum, and ε is the dielectric constant of the medium.

The Debye screening length is given by:

$$\lambda = \sqrt{\frac{\varepsilon_0 e k T}{2000 \varepsilon_0^2 N_A C_{el}}} \quad 3-12$$

where N_A is Avogadro's number and C_{el} is the bulk molar electrolyte concentration.

When the electrolyte concentration is 0.05 M, the Debye screening length is 1.34 nm at 17 °C and 1.41 nm at 48 °C [51].

With rearranging Eq. 3-12, the surface area per lipid polar head group, A_L , is calculated from:

$$A_L = \frac{\lambda \sigma e^2 e^{\frac{\psi e_0}{2kT}}}{\varepsilon \varepsilon_0 k T \left(e^{\frac{\psi e_0}{kT}} - 1 \right)} \quad 3-13$$

The last column in Table 3-3 shows the surface area per polar head groups for a series of vesicle diameters calculated from the surface electrostatic potential data. As seen from the Table 3-3, the vesicles with lower diameters have a lower surface area per polar head group, indicating a higher packing density. These values are close to the data reported in the literature (for POPG in fluid phase: $A_L=0.53 \text{ nm}^2$ [62], $A_L=0.65 \text{ nm}^2$ [63], $A_L=0.70 \text{ nm}^2$ [64], for DMPG: gel phase: 0.48 nm^2 fluid phase: 0.53 nm^2 [65]).

To ensure that the bilayer remains in the fluid phase over the entire pH range of the titration, temperatures of 17 °C and 48 °C were chosen for experiments with POPG and DMPG SUVs respectively. The reason for selecting those two temperatures is to assure the fluid phase stability during the titration. It has been known that there is a dependency between the main phase transition temperature and pH for DMPG lipids. Figure 3-15 shows pH dependence of the chain-melting phase transition temperature of bilayers with various lipid compositions [27]. At very low pH, the phase transition temperature increases to around 43 °C, therefore 48 °C was selected for DMPG lipids to ensure having the lipid bilayers in a fluid phase during the EPR titrations.

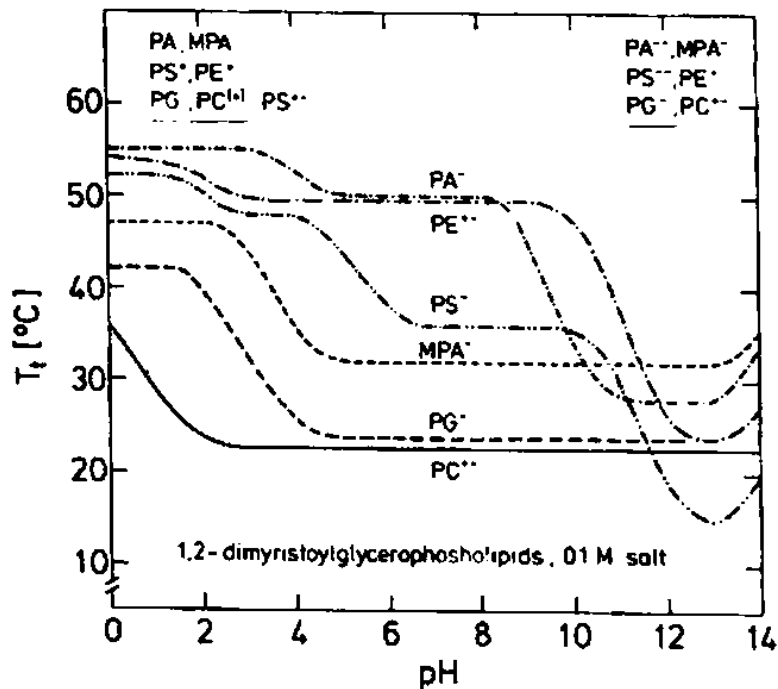


Figure 3-15 Phase transition temperature at various pH in DMPG lipid (adopted from reference [27]).

Zeta potentials were measured for a series of ULV with various diameters and no significant change was observed. -Figure 3-16 shows the graphs representing the effect of the vesicles diameter (a parameter that characterizes bilayer curvature) on the surface electrostatic potentials and the vesicle zeta potentials.

Table 1.3 shows that a decrease in the vesicle diameter results in an increase of the interfacial pK_a^0 , the electrostatic contribution to the interfacial pK_a^i , and therefore the surface electrostatic potential, Ψ . It is worthwhile mentioning that ULVs composed from POPG at 17 °C and DMPG at 48 °C are in the fluid phase, which is a biologically relevant bilayer phase state. DMPG at 17 °C is in the gel phase, in which changing the curvature did not show any significant difference in the vesicle surface electrostatic potential.

We speculate that a decrease in the vesicle diameter (an increase of positive curvature) increases the local packing density of the lipid polar head groups, thus, increasing the surface charge density. Data for DMPG ULVs in a more tightly packed gel phase (17 °C) serve as a partial proof of this hypothesis. Data for DMPG ULVs in the fluid phase (48 °C) show the same trend as POPG ULVs at 17 °C, thus, illustrating that this effect is related to the physical state of the lipid bilayer but not to the lipid chain length.

Zeta potential, on the other hand, is not affected by curvature. Zeta potential is the electric potential in the interfacial double layer (DL) at the location of the slipping plane versus a point in the bulk fluid away from the interface, therefore it is far enough from the vesicle surface to not be affected. A cartoon in Figure 3-17 shows where the surface potential and the

zeta potential are located with respect to the surface of the lipid bilayer and the bulk aqueous phase.

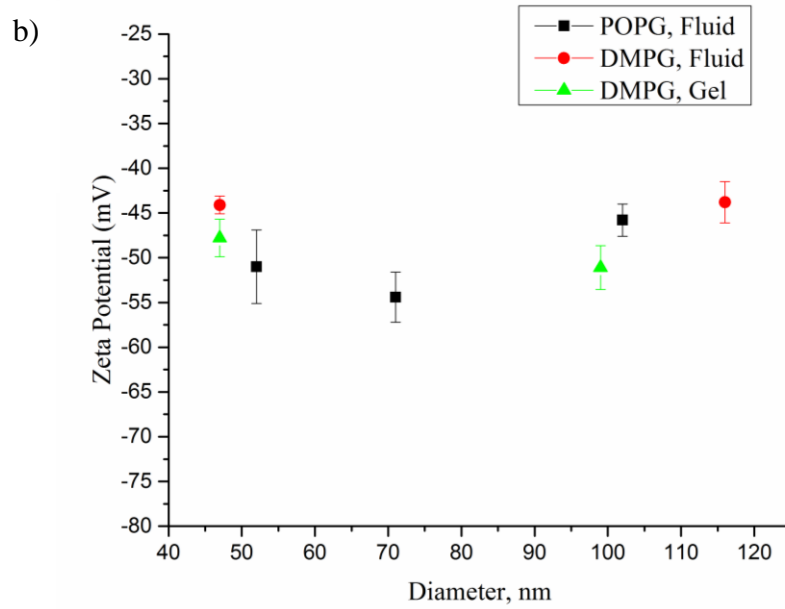
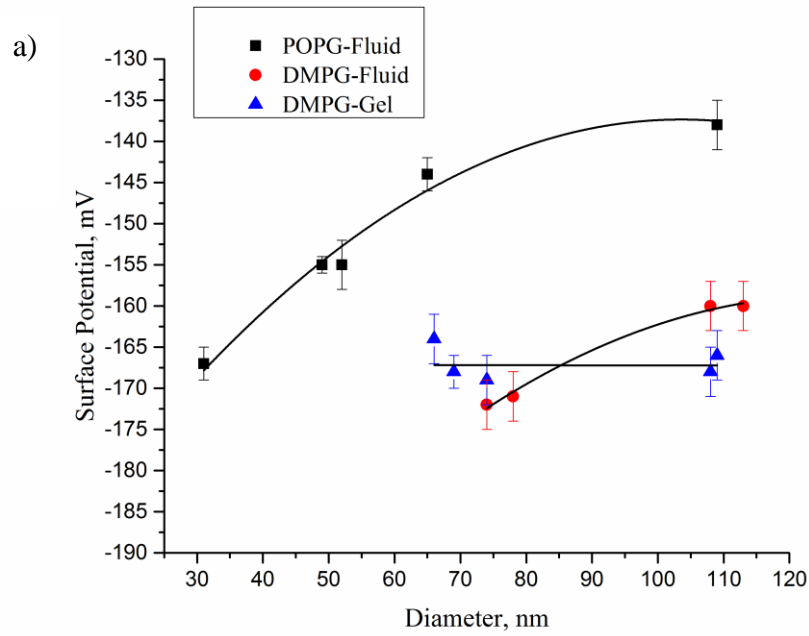


Figure 3-16 a) Effect of curvature (vesicle diameter) on the surface electrostatic potential in lipid unilamellar vesicles; b) Zeta potentials for unilamellar vesicles vs. vesicle diameter.

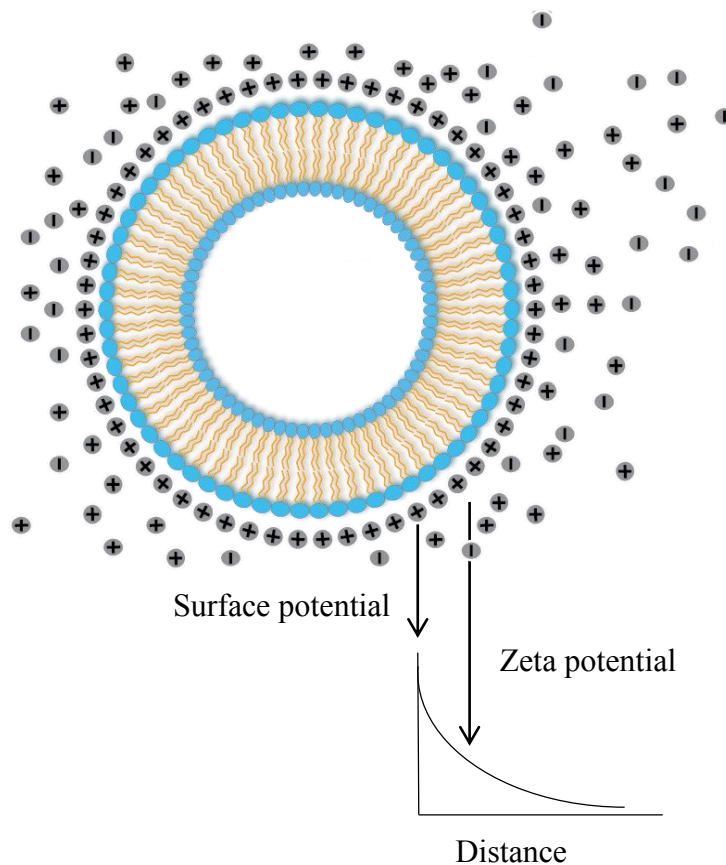


Figure 3-17 A cartoon illustrating zeta and surface potentials in curved lipid bilayers.

3.2.3 pH Equilibration of Both Inner and Outer Leaflets

To assure a complete probe pH equilibration in both the inner and the outer leaflets a small peptide gramicidine A (gA) was inserted into SUVs to form as proton channels [66]. In lipid bilayers gramicidin A dimerizes to form an ion channel to assure proton transfer between the inside and the outside of lipid bilayers. POPG lipid doped with gA (1-3 channels per vesicle) and IMTSL-PTE (1 %) was titrated using the EPR titration method described earlier in the section 3.2.2.

Figure 3-18 shows a series of EPR spectra taken at 17 °C and various pH for POPG SUVs (107 nm in diameter) containing gramicidin A channels. EPR titration curve shows essentially the same interfacial pK_a as that of 109 nm POPG SUVs without gA..

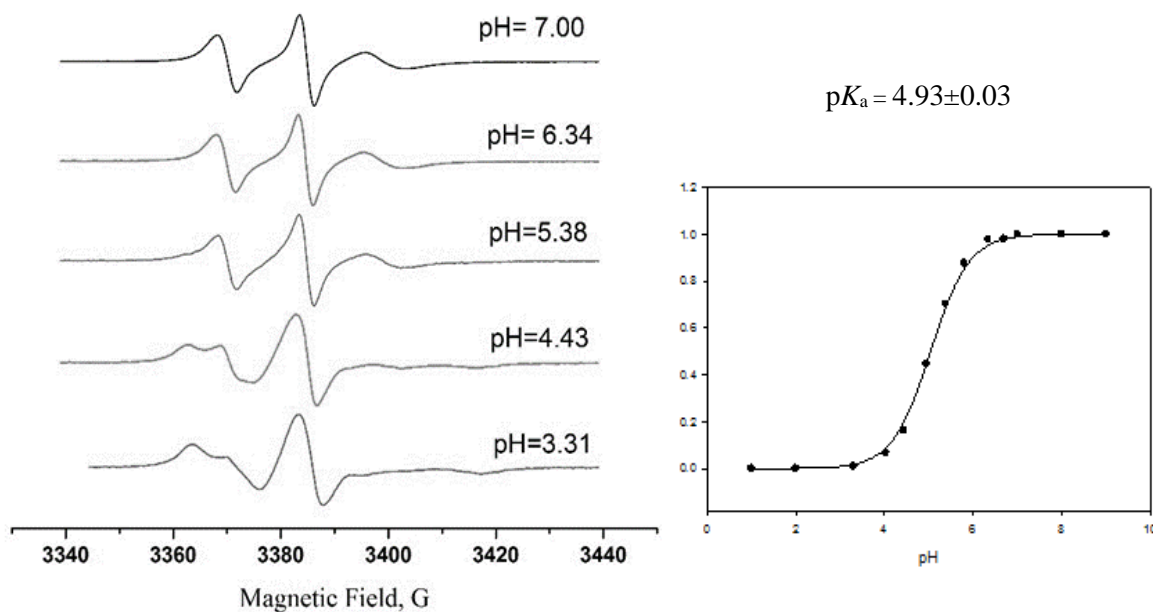


Figure 3-18 Left: X-band EPR spectra at various pH; 107 nm POPG with gramicidin A at 17 °C, right: EPR titration curve fitted into Henderson-Hasselbalch equation.

Table 3-4 summarizes the results of EPR titrations of POPG lipid with and without gramicidin A.

Table 3-4 EPR titration results for POPG SUVs prepared by extrusion through 100 nm membrane with and without gramicidin A.

Vesicle type	T, °C	Diameter, nm	pK_a^i	ΔpK_a^{el}	Ψ , mV
POPG	17	109	4.92±0.03	2.39±0.07	-138±3
POPG (w/Gra A)	17	107	4.93±0.03	2.41±0.06	-139±3

These results show that addition of gramicidin A to POPG lipid does not change the surface electrostatic potential significantly. The data also indicates that the proton equilibrium between the inner and the outer bilayer leaflets is establishing in the system over a relatively short time (20 min) employed to change pH in the bulk aqueous phase. Since proton cannot transfer through the hydrophobic core of the lipid bilayers that fast, we speculate that it is likely that the lipid transverse diffusion also known as flip-flop (Figure 3-19) is responsible for proton equilibrium across lipid bilayers. Lateral diffusion is a fast diffusion in lipid bilayers (in order of 10^{-9} s⁻¹) in comparison with transverse diffusion (in order of 10^{-3} - 10^{-4} s⁻¹), therefore, flip-flop can be considered as a slow process [67].

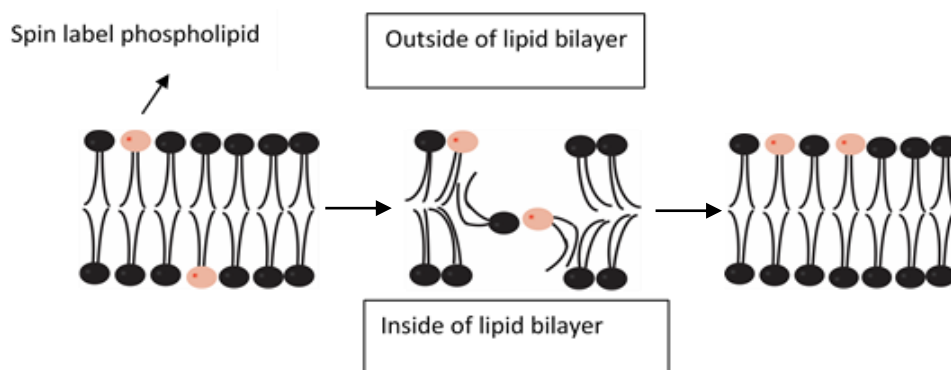


Figure 3-19 Schematic representation of the phospholipid transverse diffusion

3.2.4 Kinetics of Lipid Flip-Flops in Unilamellar Vesicles

In order to calculate the ratio of spin label phospholipids between the inner and the outer leaflets and study the flip-flop kinetics, a nitroxide reduction experiment with sodium ascorbate (shown in Figure 3-20) was performed. In this experiment, the sodium ascorbate as a nitroxide reducing agent was added to the vesicles doped with spin labeled phospholipid and the decrease of EPR intensity was recorded over time at 0 °C and 17 °C.

The EPR method to measure the lipid flip-flop is based on monitoring the reduction of nitroxide attached to outer leaflet lipid head group by EPR intensity. It is been shown that lipid bilayer membrane is essentially impermeable to sodium ascorbate at 0 °C [68]. It would be useful to add sodium ascorbate as a reducing agent in vesicles at a temperature (such as 0 °C) at which the transverse diffusion (flip-flop) process is slow compared with the rate constant of nitroxide reduction. Flip-flop rate in vesicles was studied by techniques other than EPR such as fluorescence spectroscopy [69] and small-angle neutron scattering [70, 71], however, only relative and/or approximate rate constants were obtained and no effects of lipid bilayer curvature was investigated to the best to the author's knowledge.

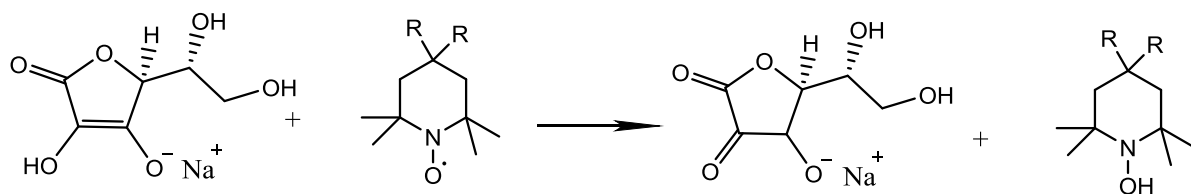


Figure 3-20 Reduction of a nitroxide radical with sodium ascorbate produces an EPR-silent hydroxylamine.

It should be noted that the EPR flip-flop nitroxide reduction experiment should be performed in nitrogen atmosphere to prevent re-oxidation of the hydroxylamine back to nitroxide radical by molecular oxygen present in air.

The following kinetics scheme was used. A spin-labeled phospholipid is flipping from inner leaflet to the outer leaflet through transverse diffusion with a rate constant k_1 and then reacts with ascorbate with a rate constant k_2 .



where Nr_{out} , Nr_{in} , NrH are concentrations of spin label phospholipids located in the outer and the inner bilayer leaflet respectively; only the outer leaflet spin-labeled lipids are reduced by ascorbate

If we assume that each reaction is the first order and $k_2 \gg k_1$, then one can write the rates for spin-labeled phospholipids in the inner and the outer leaflets as:

$$\frac{d[Nr_{in}]}{dt} = -k_1[Nr_{in}] \quad 3-16$$

$$\frac{d[Nr_{out}]}{dt} = k_1[Nr_{in}] - k_2[Nr_{out}] \quad 3-17$$

By solving these two differential equations, the concentrations of spin-labeled phospholipids the inner and the outer bilayer leaflets is:

$$[Nr_{in}] = [Nr_{in}]_0 \exp(-k_1 t) \quad 3-18$$

$$[Nr_{out}] = [Nr_{out}]_0 \left[\exp(-k_2 t) + \left(\frac{[Nr_{in}]_0 / [Nr_{out}]_0}{1 - k_2/k_1} \right) (\exp(-k_2 t) - \exp(-k_1 t)) \right] \quad 3-19$$

The signal detected in EPR is directly proportional to the sum of the signals coming from spin-labeled phospholipids located in the bilayer inner and leaflets. At higher temperature (17 °C) both reactions occur and the EPR intensity (double integral) can be written as a function of the inner and the outer leaflet concentrations, time and rate constants:

$$I_t = a([Nr_{in}] + [Nr_{out}]) + b = A \exp(-k_1 t) + B \exp(-k_2 t) + b \quad 3-20$$

where I_t is the EPR intensity at time t . a and b are constants used to correlate the EPR signal intensity to the spin labeled phospholipid concentrations.

A and B can be expressed as:

$$A = a([Nr_{in}]_0 - \frac{[Nr_{in}]_0}{1 - k_2/k_1}) \quad 3-21$$

$$B = a([Nr_{out}]_0 + \frac{[Nr_{in}]_0}{1 - k_2/k_1}) \quad 3-22$$

Double integrals for each of the signals were obtained by least-squares simulation of experimental X-band spectra, and the ratio of EPR intensity (at time t) to the initial intensity was plotted against time at 17 °C. Analysis of this kinetic data using Eq. 3-20 yielded kinetic constants k_1 and k_2 at 17 °C that are listed in Table 3-6.

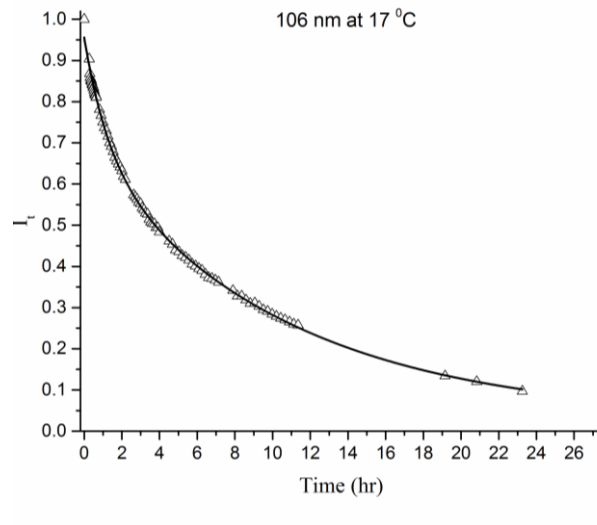


Figure 3-21 Experimental data fitted into eq. 3-20: POPG unilamellar vesicles (diameter: 106 nm) at 17 °C.

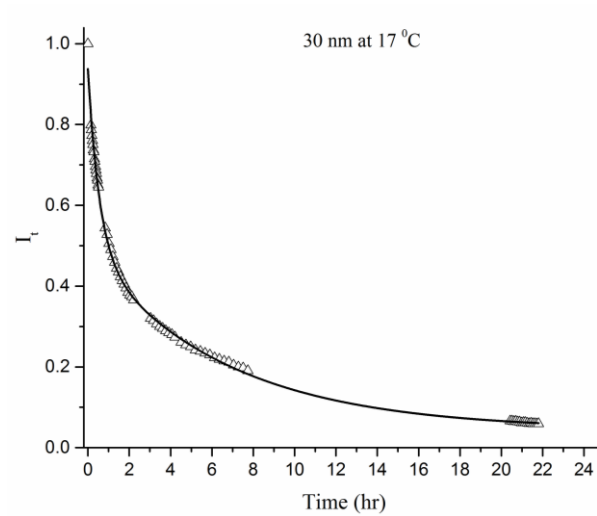


Figure 3-22 Experimental data fitted into eq. 3-20: POPG unilamellar vesicles (diameter: 30 nm) at 17 °C

If an EPR reduction experiment is performed at a low temperature (around 0 °C), the transverse diffusion would be negligible and the decay of EPR intensity is attributed only to the reduction of nitroxides in the outer leaflet. The EPR signal change at low temperature then is given by:

$$I_t = a[Nr_{out}] + b = a[Nr_{out}]_0 \exp(-k_2 t) + b \quad 3-23$$

The experimental data obtained at 0 °C was fitted into Eq. 3-23 (Figure 3-23 and Figure 3-24). At $t = \infty$, $I_t = b$ which is the EPR intensity of nitroxides located in the inner leaflet (since the inner leaflet nitroxide cannot flip-flop at this low temperature). If we define “ α ” as a ratio of the EPR intensities corresponding to the inner leaflet lipids to the total signal intensity (totally intensity at $t=0$ was normalized to 1), then $\alpha = b$ when $t = \infty$.

Numerical values for α values were obtained from fitting the EPR kinetic data at 0 °C and listed in Table 3-5. If one assumes that spin label phospholipids are distributed in the inner and outer bilayer leaflets homogeneously, one can calculate the theoretical value of α as the ratio of outer surface area to the sum of inner and outer ones. The bilayer thickness of POPG ULVs was reported to be about 3.7 nm [72]. The bilayer thickness and vesicle radius were used to calculate “theoretical α ” from Eq. 3-24 (Figure 3-5) and its values are listed in Table 3-5.

Table 3-5 The theoretical and experimental ratio of inner leaflet lipids to the total number of lipids in one vesicle.

POPG vesicle diameter, nm	Theoretical α	Experimental α
106	0.451	0.464±0.012
30	0.308	0.356±0.005

These values are close to the experimental parameters from fitting the EPR data and the remaining difference might be due to distribution of sizes instead of exact values (30 and 106 nm) we assumed for all vesicles.

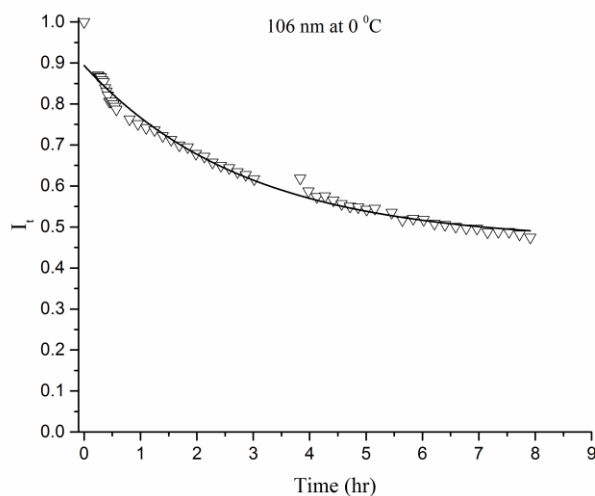


Figure 3-23 Experimental EPR nitroxide reduction data fitted into eq. 3-23: POPG unilamellar vesicles (diameter: 106 nm) at 0 °C.

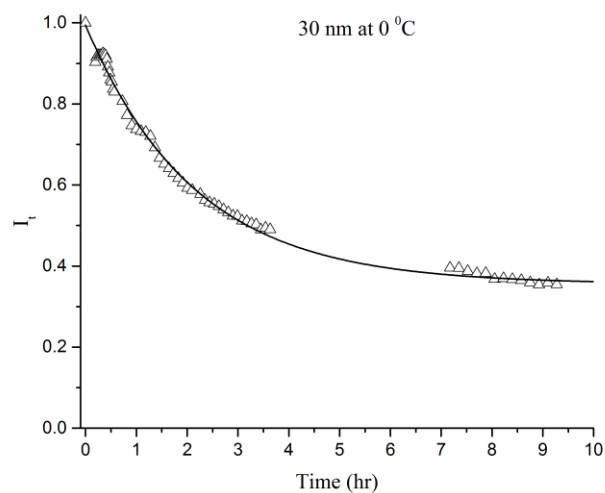


Figure 3-24 Experimental EPR nitroxide reduction data fitted into eq. 3-23: POPG unilamellar vesicles (diameter: 30 nm) at 0 °C.

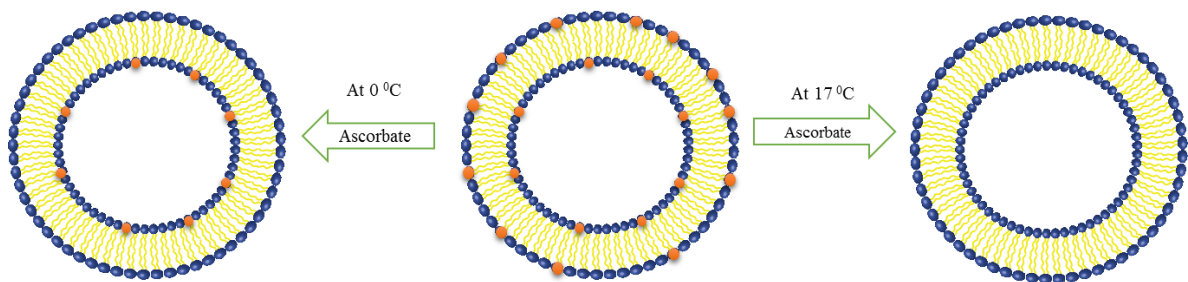
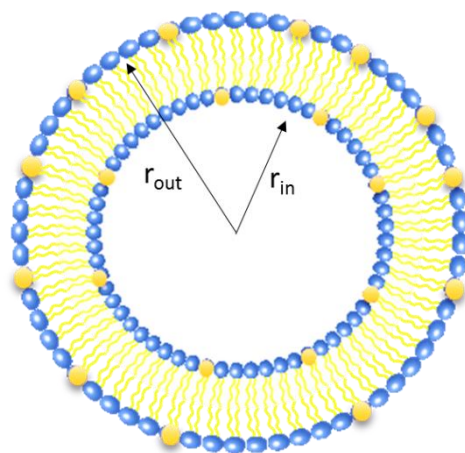


Figure 3-25 A cartoon of an EPR nitroxide reduction experiments to determine the phospholipid flip-flop rate. Sodium ascorbate reduces the outer spin labeled phospholipids and due to the lack of flip-flop at a low temperature, the EPR intensity of the inner leaflets remains (orange circles represent nitroxide radicals).



$$\alpha_{theoretical} = \frac{4\pi r_{in}^2}{4\pi r_{out}^2 + 4\pi r_{in}^2}$$

$$r_{out} - r_{in} = 3.7nm$$

3-24

Figure 3-26 Calculation of theoretical “ α ” for POPG ULVs. Yellow circles represent spin labeled phospholipids.

Table 3-6 Rate constants for the outer leaflet ascorbic acid reduction and transverse diffusion in POPG unilamellar vesicles at various size and temperature.

Vesicle Diameter, nm	T, °C	k ₁ , hr ⁻¹	k ₂ , hr ⁻¹
106	17.0±0.1	0.094±0.006	0.780 ±0.053
30	17.0±0.1	0.151±0.008	1.795±0.096
106	0.0±0.2	-	0.350±0.028
30	0.0±0.2	-	0.467±0.011

The k_1 and k_2 values show that a decrease of vesicle diameter increases the rate constant for the lipid flip-flop and the reduction of the nitroxide located in the outer leaflet. The change

in the flip-flop rate is likely to be related to defects in vesicles. When the vesicle size decreases, an appearance of defects in the lipid bilayer provides easier path and faster reduction rate and flip-flop rate. The obtained flip-flop rate constants (k_1) are consistent with those values reported before, for instance, flip-flop rate constant for DMPC unilamellar vesicles (100 nm) was reported to be of 0.12 hr^{-1} in liquid phase [70] and for sonicated lipid mixtures was measured to be from 0.11 to 0.40 hr^{-1} depending on the lipid composition [73].

3.2.5 Dynamics inside Lipid Bilayers

- **Oxygen Permeability:**

It has been known that oxygen permeability coefficient in phospholipid bilayers can be measured by EPR [74]. The oxygen permeability in lipid bilayers doped with 5PC in different curvatures was measured. Molecular oxygen is unique because of its small size and appropriate level of hydrophobicity and can enter to the packed lipids therefore changing the structure and packing would be detectable.

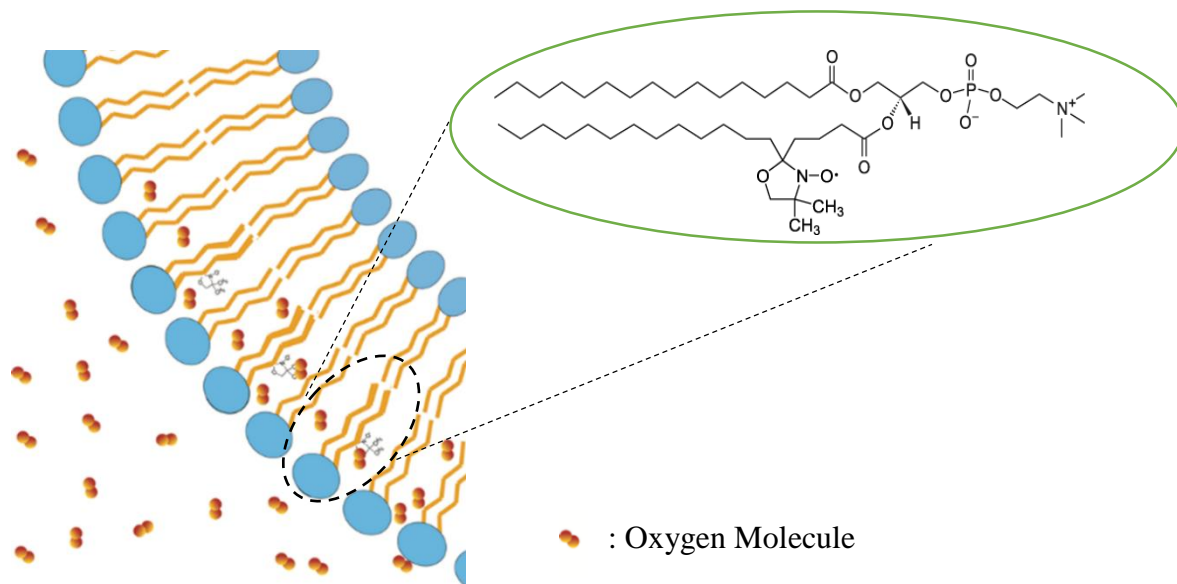


Figure 3-27 Graphical presentation of lipid bilayer oxygen permeability and chemical structure of 5-Doxyl-PC (1-palmitoyl-2-stearoyl-(5-doxyl)-sn-glycero-phosphocholine).

Heisenberg spin exchange is dominant mechanism for the interaction between oxygen molecule and a spin probe. The bimolecular collisions of molecular oxygen with spin probe can be detected with continuous-wave (CW) EPR from either changes in electronic relaxation times (by power saturation experiments) or spectral line broadening. For slow tumbling motion (such as nitroxide radical inside lipid bilayers) the oxygen broadening can be expressed as [74]:

$$F(B) = \int_{-\infty}^{+\infty} F_0(B')m(B - B')dB' \quad 3-25$$

where $F_0(B)$ and $F(B)$ are the experimental EPR spectra taken in the absence and presence of oxygen and $m(B)$ is the homogenous (Lorentzian) broadening. The fitting method based on this equation was carried out using EWVOIGT software developed by Alex Smirnov. The Lorentzian broadening was measured by comparing two spectra in the presence of nitrogen and oxygen.

Permeability of oxygen through the lipid bilayers could be stronger affected by bilayer packing rather than the rotational dynamics of phospholipids. X-band EPR spectra of unilamellar vesicles doped with spin-labeled lipid 5-Doxyl-PC (1-palmito-yl-2-stearoyl-(5-doxyl)-*sn*-glyce-ro-3-phosphocholine) show significant oxygen-induced spectral line broadening (Lorentzian line width broadening).

The result of oxygen permeability experiments are summarized in Table 3-7. With a decrease in the vesicle size, the oxygen permeability through the lipid membrane reduces suggesting that the lipid molecules in the smaller vesicles are more tightly packed. Figure 3-28

shows how CW X-band EPR spectra are changing upon oxygen penetration into lipid bilayers; the spectrum becomes broader when oxygen concentration around nitroxide radical increases.

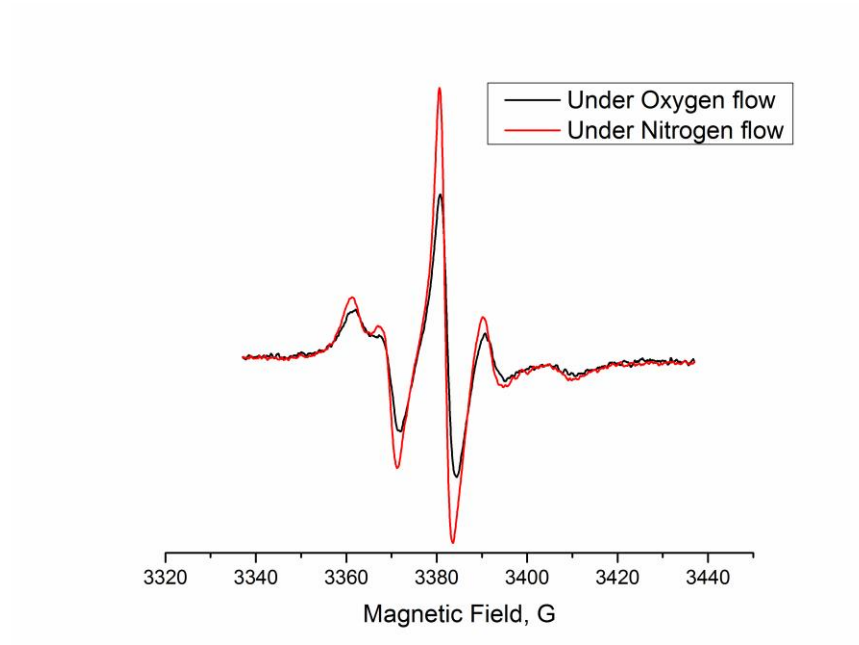


Figure 3-28 Experimental X-band EPR spectra of DMPG ULVs (108 nm) labeled with 5- PC at 1 mol% in the presence of 100% O₂ (black line) and 100% N₂ (red line) at 1 atm and 30.5 °C.

Table 3-7 Oxygen permeability measured as Lorentzian broadening (peak-to-peak) for POPG and DMPG unilamellar vesicles doped with 1 mol% 5PC. The error was calculated from fitting of the experimental spectrum.

Vesicle type	Phase	T, °C	Diameter, nm	Lorentzian, mG
POPG	Fluid	23	37	377±4
POPG	Fluid	23	103	441±4
DMPG	Fluid	30.5	47	516±4
DMPG	Fluid	30.5	108	586±4
DMPG	Gel	17	47	183±4
DMPG	Gel	17	108	152±4

It is interesting to mention that upon increasing the size of the vesicles in the gel phase, the oxygen permeability parameter would decrease, but when vesicles are in fluid phase, the oxygen permeability increases with vesicle diameter increase. The transition from gel to fluid phase increases the oxygen permeability as demonstrated for DMPG vesicles and is in agreement with the data published previously [74].

- ***Partitioning of TEMPO into the lipid bilayer***

Small nitroxides partitioning from aqueous solution to the lipid bilayers could be affected by the lipid packing. Partitioning of small probes into lipid bilayers results in a partial splitting of the high field component of X-band EPR. The ratio of nitroxide in the lipid and aqueous phase can be determined by comparing the magnitude of this splitting [75].

One way to estimate the fraction of nitroxide probe dissolved in the lipid phase is to estimate by a visual evaluation of EPR spectrum. The fraction of lipid phase can be estimated using equation [75, 76]:

$$f = H/(H + P) \quad 3-26$$

Where H and P are as shown in Figure 3-29. EPR spectra of TEMPO in POPG ULVs in two different diameters (27 and 100 nm) are shown Figure 3-29. Using Eq. 3-26, the value of f is approximately equal to the fraction of TEMPO in lipid phase and it is been shown that spectra simulation provides more accurate value for lipid phase fraction [76], therefore we employed spectra simulation to calculate the lipid phase fraction upon partitioning. TEMPO partitioning experiments were carried out at X-band by measuring EPR spectra from unlabeled lipid vesicles mixed with a stock solution of TEMPO to the final concentration of 80 μM .

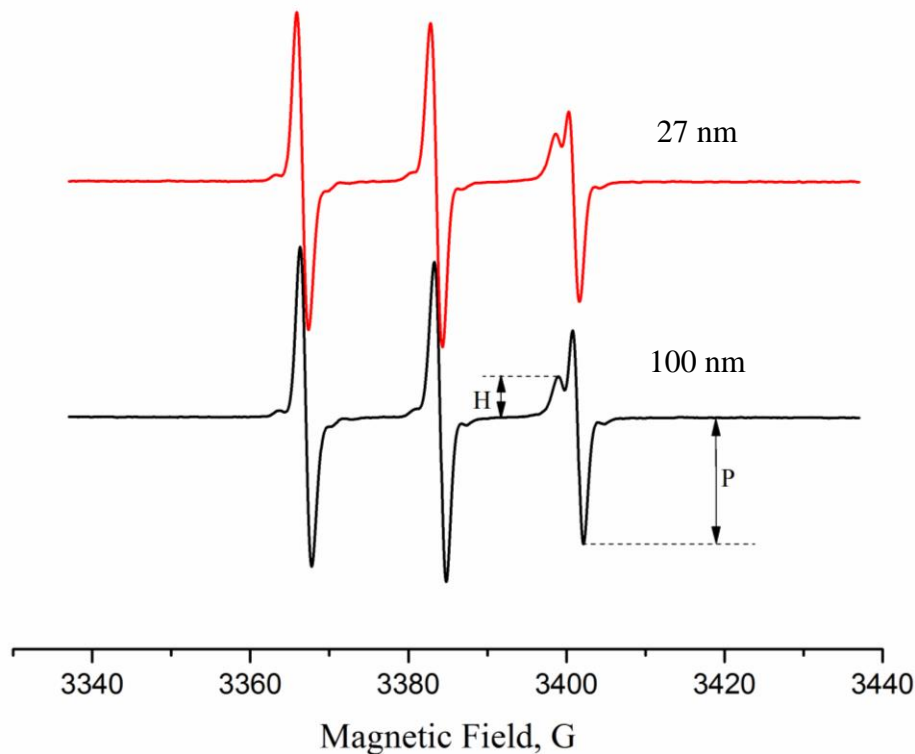


Figure 3-29 Experimental X-band EPR spectra at 22 °C of POPG UUVs (27 and 100 nm) and TEMPO. The amplitudes of the splitting in high field (H and P) can be used to calculate partitioning coefficient. Amplitude of H and P are approximately proportional lipid and aqueous phases respectively as discussed in ref [76].

In order to calculate the partitioning coefficient more accurately, we simulated and decomposed X-band EPR spectra into the lipid and aqueous phases. Then the double integral of each spectrum was used to calculate the fraction of TEMPO in lipid phase. Figure 3-30 shows a decomposition of X-band EPR spectrum measured for 27 and 100 nm POPG ULVs. As indicated by the fit residual (i.e., difference between the experimental and simulated spectra), the modelled spectra fit the experiment well, thus, allowing for more accurate measurements of the TEMPO partitioning coefficient between the lipid and aqueous phases.

Simulated and experimental spectra are essentially identical which is an indication of a good fit.

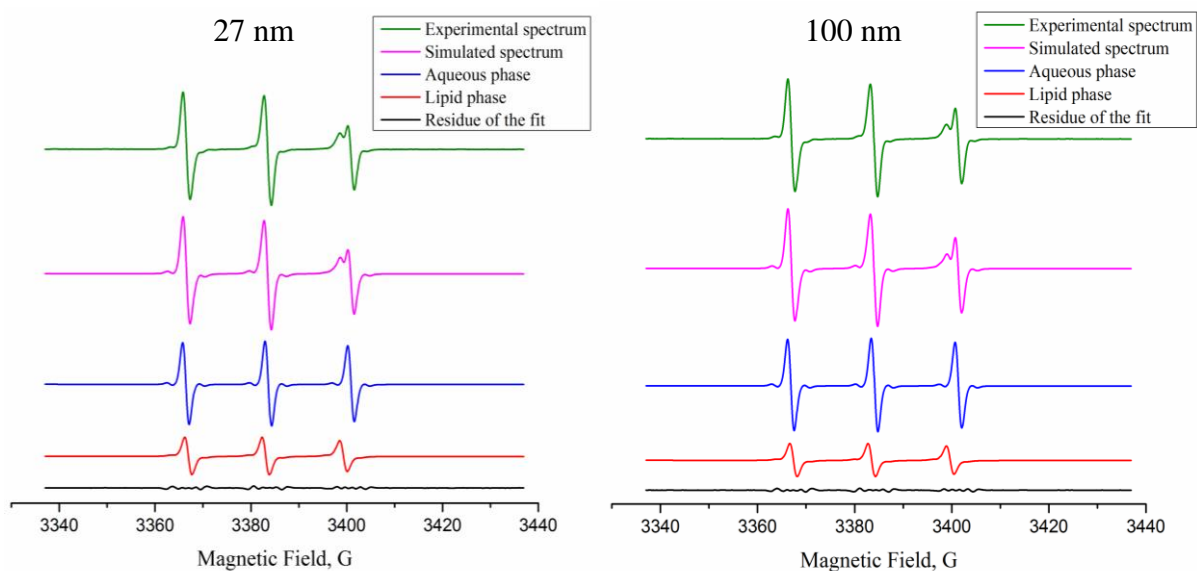


Figure 3-30 Decomposition of X-Band EPR spectra of TEMPO partitioning into POPG ULVs (left: 27nm and right: 100nm)

We used the intensity of each phase EPR spectra to calculate the percentage of TEMPO in lipid phase. The results of X-band EPR simulation/decomposition are listed in Table 3-8.

Table 3-8 Partitioning of TEMPO between lipid and aqueous phases of POPG ULVs measured by X-band EPR at 22 °C.

Size, nm	N_{hyperfine} (aqueous phase), G	N_{hyperfine} (lipid phase), G	Lipid Phase %
27	17.230± 0.002	16.174± 0.008	47.0±1.6
40	17.262± 0.001	16.175± 0.003	44.2±0.6
92	17.268± 0.001	16.166± 0.003	41.4±0.5
100	17.251± 0.002	16.130± 0.009	41.5±1.6

Our result showed that when the curvature increases partitioning of TEMPO into the lipid bilayers would increase. This might be due to a higher concentration of local defects that are capable of accommodating more TEMPO molecules. One might expect to observe a lower partitioning due to a higher packed lipids in smaller vesicles; however, a higher curvature produces more tension and defects in lipid bilayers. These defects have been known to have significant impacts on binding of some proteins such as alpha-Synuclein to the lipid bilayers [77]. Increase in number of defects in highly curved bilayers releases some stress and provides conditions for better local packing of phospholipids. We speculate that it is those defects formed between ordered patches of lipids in the outer leaflets of curved bilayers that allow TEMPO for more effective partition.

TEMPO partitioning into POPG ULVs was also investigated by W-band CW EPR (95 GHz). W-band EPR provides tenfold better g-factor resolution than X-band EPR and allows for clearly resolving the EPR signals originating from the lipid and the aqueous phase

(Figure XCX). The three intense lines are related to the nitroxide probe partitioned in water and three broad lines represent TEMPO molecules tumbling in a more viscous lipid phase. In order to obtain the intensity of spectrum for each phases, we employed simulation and decomposition of W-band EPR for each vesicle size by EWVOIGTN software.

Results of W-band EPR experiments confirmed the initial observations by X-band EPR: a decrease of the vesicle diameter promotes partitioning TEMPO in the lipid phase (Figure 3-31, right; TEMPO in lipid phase).

Magnetic interactions and EPR spectral line shapes of nitroxides spectra are affected by the angular motions relative to the external magnetic field making spin-labeling EPR a suitable technique to study rotational diffusion. The time scale of nitroxide rotational diffusion can strongly affects the spectral line shapes. For isotropic motion rotational correlation time (τ_c) is related to the rotational diffusion coefficient D_R as [8]:

$$\tau_c = \frac{1}{6D_R} \tag{3-27}$$

Then, if a nitroxide EPR spectrum falls into a fast motion regime, the homogeneous line width of an individual nitrogen hyperfine components can be written as [76]:

$$T_2^{-1}(m_I) = A + Bm_I + Cm_I^2 \tag{3-28}$$

where A, B and C are line width parameters. m_I is the z-component of nuclear spin quantum number. B can be calculated from high field (L_1) and low field (L_{-1}) components from spectra simulation:

$$B = \frac{L_1 - L_{-1}}{2}$$

3-29

The B values for 120, 97, and 41 nm POPG ULVs were found to be 50 ± 7 , 58 ± 6 , and 100 ± 9 mG respectively. B is directly proportional to the correlation time, τ_c [76], and B values showed that the rotational diffusion slows down when vesicles are smaller. It has been shown that TEMPO is located very close to the aqueous phase when diffusing into the lipid bilayer [76, 78]. When TEMPO goes into the smaller vesicles, higher packed lipids affects the rotational correlation time making it longer. This is another indication of a higher packing of the phospholipids inside smaller vesicles.

W-band EPR allows for clearly resolving TEMPO EPR signals originating from aqueous and lipid phases with the spectrum related to the lipid phase being shifted to a lower field. This indicates that g_{iso} for TEMPO in the lipid bilayers is greater than that of in water [76, 79].

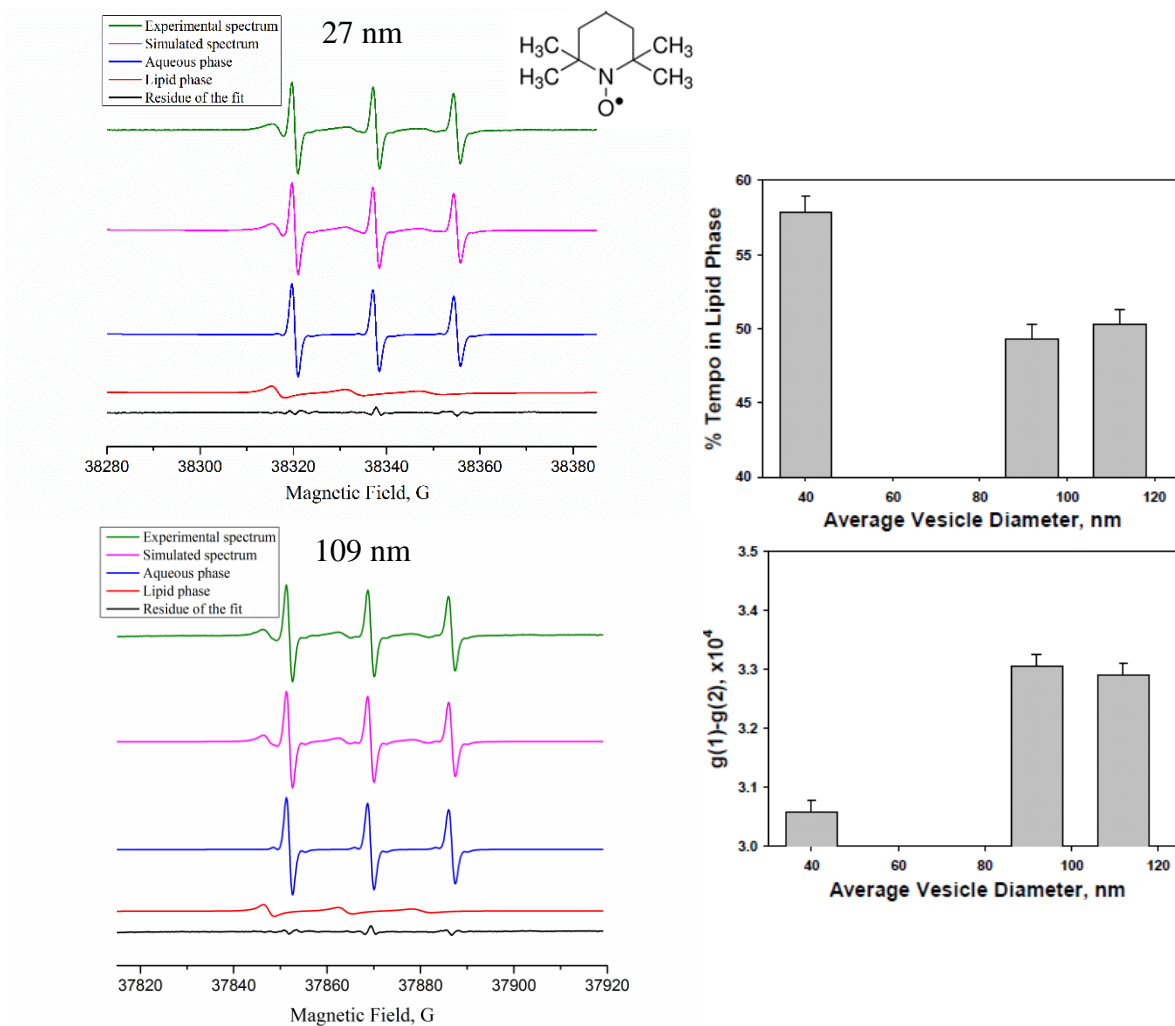


Figure 3-31 Left) Least-squares decomposition of an experimental W-band (95 GHz) EPR spectrum of TEMPO for partitioning in 100 and 27 nm POPG ULVs: Experimental EPR, simulated EPR in lipid phase, simulated EPR in aqueous phase and residual of the fit. **Right)** Partitioning of TEMPO into the lipid phase in different diameters for POPG ULVs at 22 °C.

3.2.6 Conclusions

A series of unilamellar vesicles (POPG and DMPG) were prepared by extruding through nanopore membrane or sonicating (for smaller size) multilamellar vesicles. The DSC measurements for the unilamellar and multilamellar vesicles showed that in smaller unilamellar vesicles, the phase transition was broader indicating a decrease in the cooperativity number with increase in the bilayer curvature.

The surface potential of lipid bilayers is an important factor in cell functionality. X-band EPR spectroscopy and pH-sensitive head-group labeled phospholipids were employed to determine the local electrostatic surface potential as a function of the vesicle diameter. EPR titration method was used to measure the changes in the interfacial pK_a of the probes that was evident from changes in its spectra with pH. Each spectrum was decomposed into the protonated and nonprotonated form and surface potential was measured from the change of electrostatic contribution of interfacial pK_a . Effect of curvature on the electrostatic surface potential as well as dynamics of lipid bilayer was studied. Specifically, the magnitude of the negative surface electrostatic potential, Ψ , for POPG unilamellar vesicles (ULVs) in the fluid phase (17 °C) increased from -137 to -167 mV upon decrease in the vesicle diameter from 107 to 31 nm. This effect could be rationalized by assuming different lipid packing upon increase in the ULVs' curvature. For DMPG ULVs at 48 °C (liquid phase), the same trend was obtained. Interestingly, no significant differences in zeta-potential for POPG ULVs of different diameters were observed. For DMPG ULVs in the gel phase (17 °C) the observed effect is not that pronounced. We speculate that biologically relevant fluid bilayer phase allows for a larger

variability in the lipid packing density in the lipid polar head group region than a more ordered gel phase. To assure a complete probe pH equilibration in both inner and outer leaflets a gramicidin A (gA) proton channel was inserted into SUVs. The electrostatic potentials determined for vesicles of the same diameter both with and without gA were found to be nearly identical. It is likely that the lipid flip-flop is responsible for pH equilibration of IMTSL-PTE. To measure the flip-flop (transverse diffusion) in curved bilayers, sodium ascorbate as a nitroxide reducing agent was added to the SUVs. The kinetic study of reduction showed that the rate of flip-flop is of the order of 10^{-5} s^{-1} . The rate constant increases when vesicle size decreases. This might be due to higher defects and tension in smaller vesicle which results in faster flip-flop rate.

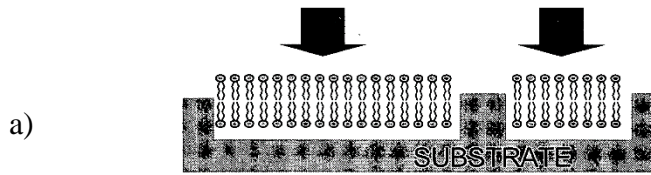
The packing of lipids inside bilayer was investigated by carrying out a series of EPR oxygen accessibility experiments by comparing X-band EPR spectra in the presence and absence of molecular oxygen but at the same temperature. A higher oxygen permeability into the lipid bilayer results in a further broadening of X-band EPR spectra of spin labels located inside the bilayer. The Lorentzian broadening parameter was obtained by simulating each spectrum and we observed an increase in the oxygen permeability coefficient inside larger vesicles. This could serve as another proof of a denser lipid packing inside smaller vesicles. Gel phase vesicles compared to the liquid phase vesicles of the same diameter showed a lower oxygen permeability, which can be explained by more packed and rigid lipids when the bilayer is in a gel phase.

TEMPO partitioning into ULVs was studied by X- and W-band EPR spectroscopy. In both experiments, the unlabeled vesicle suspension was equilibrated with TEMPO before recording X- and W-band EPR spectra. Decomposition of each spectrum provides the ratio of TEMPO molecules partitioned into the lipid phase vs. that in the aqueous phase. A higher partitioning was observed in smaller vesicles that can be rationalized by assuming a higher number of defects in more curved lipid bilayers. However the rotational correlation time for TEMPO in smaller vesicles increases, which is related to the highly packed lipids around the TEMPO radical.

Chapter 4. The Surface Electrostatics and Phase Properties of the Nanopore-confined Lipid Bilayers

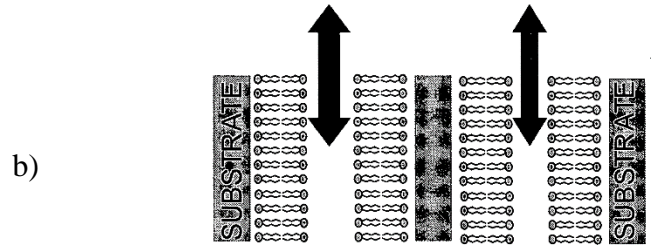
4.1 Introduction

Nanopore-confined lipid bilayers have found many practical applications, including modeling of negative curvature of cellular membranes and stabilizing membrane proteins in functional conformations [80]. It is known that phospholipid vesicles fuse spontaneously into planar membranes on specific surfaces (*e.g.*, silica, glass plates). Self-assembly of lipid bilayers on inorganic substrate can be used in studying of protein membrane interaction. There are two types of lipid arrays attached to the substrate: in planar design such as deposition on glass substrate [81] or in inorganic nanochannels such as nanoporous anodic aluminum oxide (AAO) which is developed by Alex. I Smirnov et al (Figure 4-1) [82, 83].



a)

Figure 1
(Prior Art Planar Lipid Array)



b)

Figure 2
(Lipid Nanotube Array)

Figure 4-1 Two types of lipid bilayer depositions on inorganic substrate: a) deposition on a planner substrate, b) deposition into inorganic substrate nanochannels (nanotube array: arrows show the area exposed to the aqueous media. Reproduced from ref [83].

Some of the disadvantages in planar substrate-supported lipid bilayers are their fragile structure and sensitivity to the small contamination of the surface which makes a catastrophic consequence the bilayer phospholipid assembly. In addition, the amount of lipid deposited on the surface is limited by surface area exposed to the lipid suspension. In our work we used self-assembling cylindrical phospholipid structures inside the nanopores aluminum oxide (AAO) because this structure is well-studied material and exhibits aligned through-film porous structure. The AAO pores are macroscopically homogeneous and hexagonally packed with the pore diameter tunable from 4 to 200 nm [82].

The structure of nanopore-confined lipid bilayer was characterized by EPR [82]. In order to do that, lipid bilayer doped with 1-palmitoyl-2-stearoyl-(5-doxy)-*sn*-glycero-3-phosphocholine (5PC) as spin probe was inserted into the AAO nanochannels. DMPC Lipid alignment in AAO nanochannels was confirmed by comparing the W- band EPR (95 GHz) spectra of randomly dispersed vesicles and those of AAO substrate with deposited DMPC:5PC (Figure 4-2). The differences in intensities of characteristic peaks indicate the lipid alignment in AAO substrate.

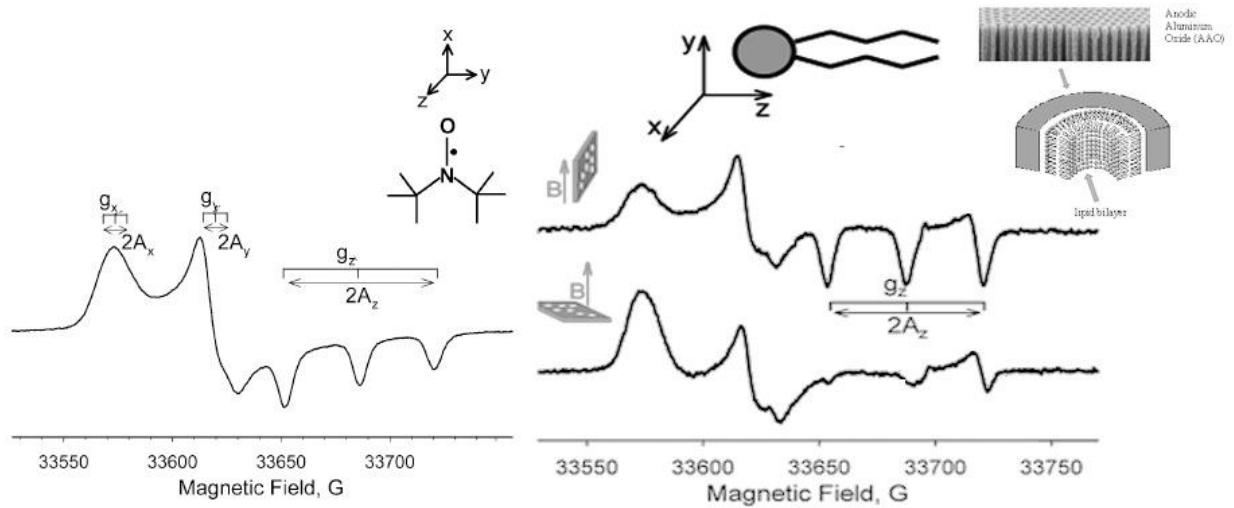


Figure 4-2 Left: high-resolution 94.4 GHz (W-band) EPR spectrum of randomly dispersed vesicles (in rigid limit) and the orientation of nitroxide magnetic axes with respect to molecular frame. Right: high-resolution 94.4 GHz (W-band) EPR spectrum of AAO substrate with deposited DMPC: 5PC (100:1) at two orientations of the substrate surface in the magnetic field. Cartoon shown is the structure of lipid bilayer inside AAO nanopores. Reproduced from [82].

When the surface of the AAO substrate containing nanopore-confined bilayer is perpendicular to the external magnetic field, the principal axis z-component of spectrum is disappeared. The z-axis in the nitroxide magnetic axes of 5PC is approximately aligned along the phospholipid chain; therefore, phospholipids are oriented along axis perpendicular to the magnetic field and perpendicular to the direction of pores. In fully hydrated samples, the lipids are organized in bilayers rather than in monolayers because the AAO surface is known to be hydrophilic [82].

However, only little is known about interaction between the lipids and the substrate surface and the properties of the confined lipid bilayer-water interface. Spin probe EPR is one of the methods that could be used to investigate various properties of heterogeneous nanostructures including local molecular structure, dynamics, and polarity. This method was used to determine the phospholipid surface potential inside AAO nanopores. Along with EPR, we used quartz crystal microbalance (QCM) to characterize AAO and study the phase properties of nanopore-confined lipid bilayers. Protein interaction with lipid bilayers also might be different when it comes to the lipid inside the pores. Protein interaction with AAO and lipid in AAO was also studied.

4.2 Results and Discussion

4.2.1 Surface Potential Measurement of Confined Lipid Bilayers

In this part, we used the same approach as described in Chapter 3 (section 3.2.2) to measure the surface electrostatic potential in a negative curvature model. We determined the surface electrostatic potential of the lipid bilayer composed of POPG confined within nanoporous anodic aluminum oxide (AAO: 200nm). Two methods were used to deposit phospholipid suspension into the wall of nanopore AAO. In one of the methods lipid suspension was passed through AAO nanopores and due to interaction of lipid head group with AAO surface, bilayer can form inside the pores. In another method lipid suspension was placed on top of the AAO and kept at the temperature higher than phase transition until it was dried. The capillary forces inside the pores makes the diffusion of lipid suspension into the pores easier. In order to have a good deposition of lipids inside the pores, the temperature has to be higher than phase transition temperature to allow liquid crystalline lipids diffuse into the pores.

X-band (9.5 GHz) EPR spectroscopy was utilized to follow pH-induced changes in magnetic parameters of the spin-labeled phospholipid (Figure 4-3).

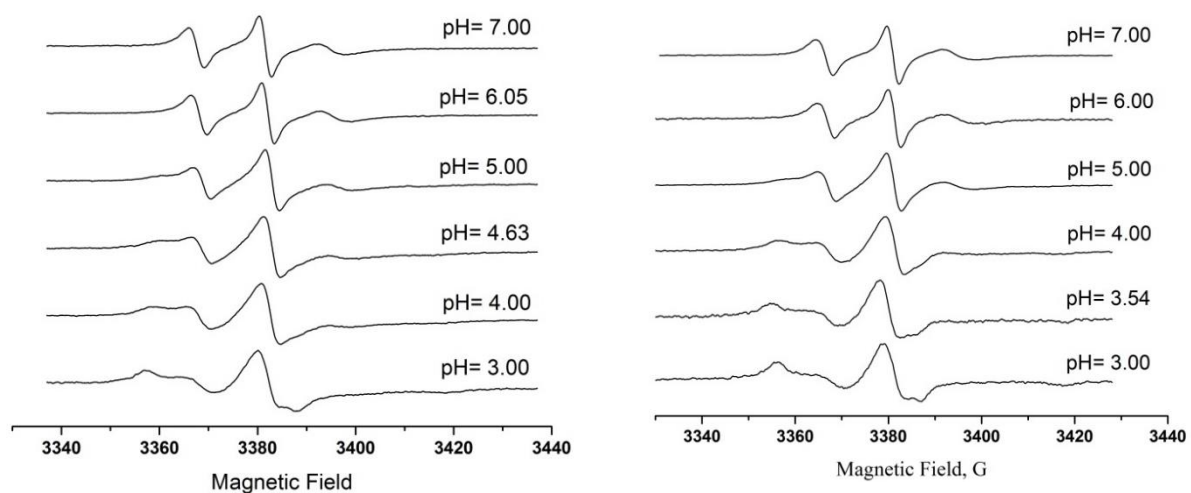


Figure 4-3. EPR spectra from AAO-supported POPG lipid bilayer doped with 1 mol. % of IMTSL-PTE measured at various pH. Left: Supported bilayers were obtained through hot plate deposition/freeze-thaw cycling. Right: Supported bilayers were prepared through syringe lipid extruder.

EPR spectra of POPG doped with 1 mol % of ionizable IMTSL-PTE show significant changes within a pH range from ≈ 5.0 to ≈ 3.5 units.

Appearance of the additional broad component in the low-field part of the EPR spectrum (Figure 4-3) must be attributed to a protonated fraction of the nitroxide. Note that with lowering the pH an additional splitting in the central component of the spectrum from the sample obtained through the lipid extrusion has appeared (at pH = 4.5). We speculate that this splitting resulted from the lipid bilayer distortion caused by pH change and illustrates a lower rigidity of the bilayer formed through the lipid extrusion.

Using EPR spectra of the nonprotonated and protonated forms of the probe as reference spectra, the experimental two-component EPR spectra acquired at intermediate pH were least-squares-decomposed into the spectra of individual forms. Figure 4-4 shows an example of decomposition of EPR spectrum at pH= 5.00.

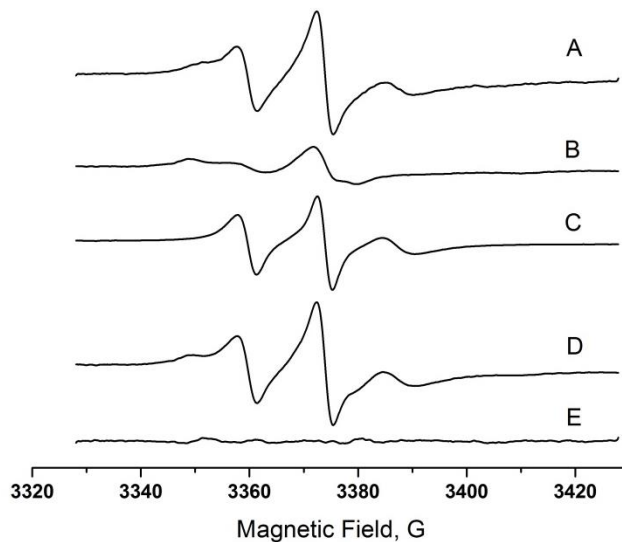


Figure 4-4 An example of a least-squares decomposition of an EPR spectrum acquired from IMTSL-PTE lipid in POPG bilayer confined within the 200 nm AAO nanopore and equilibrated with a buffer solution at pH = 5.00 into individual spectra of the protonated and the nonprotonated forms. (A) Experimental spectrum; Least-squares simulated spectra of (B) nonprotonated and (C) protonated forms of the nitroxide; (D) simulated spectrum; (E) residual of the fit.

By fitting the data into Henderson-Hasselbalch equation, titration curve is obtained. One example of this titration curve is shown in Figure 4-5.

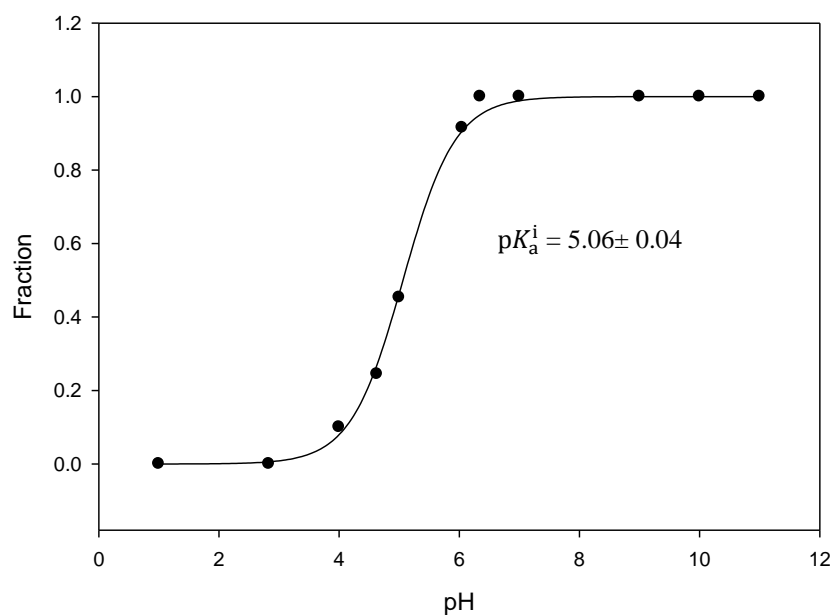


Figure 4-5. Fraction of the nonprotonated form of the IMTSL-PTE plotted as a function of pH. Solid line represents the least-squares Henderson-Hasselbalch titration curve. POPG lipids were deposited into AAO through the hot-plate method.

AAO sample with lipids deposited on was immersed into a buffer solution with required pH for 20 min. Samples equilibrated at pH ranging from 7.0 to 2.0 were acquired in this way.

Table 4-1 shows the surface electrostatic potential measured for nanopore-confined lipid bilayers.

Table 4-1 Surface electrostatic potential and interfacial pKa of nanopore-confined POPG (AAO pore size: 200nm).

Deposition Method	pK_a^i	ΔpK_a^{el}	$\Psi(\text{mv})$
Extrusion	5.18 ± 0.03	2.79 ± 0.06	-177 ± 3
Hotplate	5.06 ± 0.04	2.67 ± 0.06	-170 ± 4

As it is shown, the method of deposition is not affecting the surface electrostatic potential significantly. However, to optimum the equilibration of proton into the nanopore-confined lipid bilayer, sonication at low power during the titration was applied. If one compared the result obtained surface potential in vesicles (see chapter 3) with the one for nanopore confined bilayer, it can be seen that the charge density on the surface lipid bilayers inside the pores is higher than the one on vesicles which might be due to higher packing of lipids located inside the pores and less flexibility compared to liposomes.

4.2.2 AAO Surface Charge

The surface charge on the surface of AAO was investigated by measuring zeta potential of AAO powder. When AAO powders are in 50 mM phosphate buffer at pH=7.00 (the same buffer used to prepare lipid suspension), the zeta potential was found to be -37.8 ± 2.9 mV which means that the surface charge of AAO is negative at this pH. We have used two types of AAO; commercial Whatman AAO and homemade AAO (Antonin Marek prepared the homemade AAO in Smirnov's lab at NC State University). For NCSU AAO (70 nm), the zeta potential was obtained to be -29 ± 0.64 mV in phosphate buffer at pH=7.00 (50mM). The zeta potential

for white powder of porous alumina as reference was found to be -35.1 ± 0.6 mV in the same buffer.

Zeta potential is dependent on the type electrolyte and pH. Commercial AAO zeta potential titration in 50 mM phosphate buffer is shown in Figure 4-6. The isoelectric point (pH_{iso}) where the net surface charge is zero can be determined from this plot. pH_{iso} is 2.27 for commercial AAO in 50 mM phosphate buffer, which means that we have to be at pH lower than 2.27 to assure the surface charge is positive.

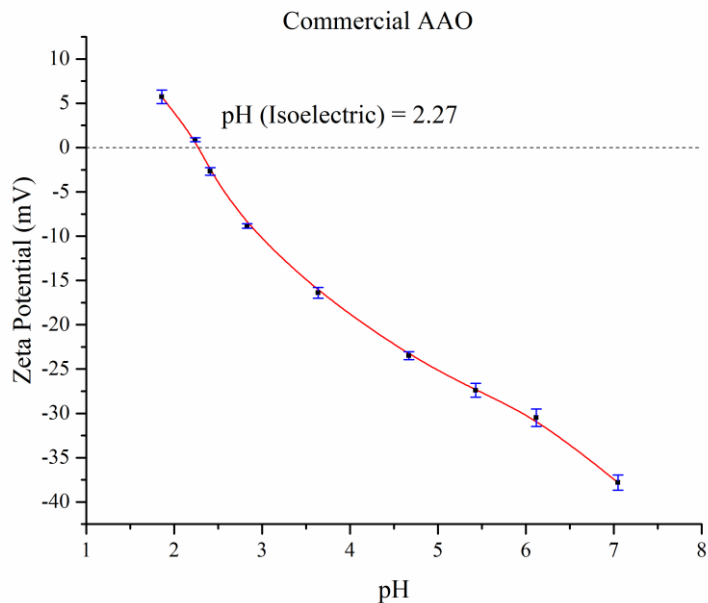


Figure 4-6 Zeta potential titration of AAO (200 nm) in 50 mM phosphate buffer.

The charge on the AAO surface allows us to deposit charged molecules into the AAO nanopores.

4.2.3 Protein Deposition into AAO

Protein nanotubes has been prepared widely to produce systems with different characteristics and these biocompatible structures have advantages over other nanotubes (e.g. carbon nanotube) to be used as in biomedical applications such as biosensors and bioseparation [84-88]. Layer by layer deposition was used to prepare protein nanotubes. They were prepared by extruding different protein solutions into AAO nanopores. AAO has been used to deposit proteins inside the pores [89]. As we have found that the AAO surface charge is negative at pH higher than 3, therefore with depositing proteins with different isoelectric points, we are able to make multilayer protein nanotubes, because depending on isoelectric point for each protein, they can carry different charges. The interaction is mostly electrostatic which comes from opposite charges from one layer to another one.

Extrusion was used to deposit proteins inside the AAO. Proteins deposited into AAO was studied by CD and UV-Vis spectroscopy. Since the AAO surface charge is negative, the first layer should be positively charged to have maximum electrostatic interactions.

The cytochrome C (cyto-c) as very important electron transfer and redox protein [88] was used as first layer at pH 7.4. At this pH, cytochrome C is positively charged since its isoelectric point is 10.7 [90]. The deposited AAO has red color which is an indicative of cyto-c deposition. The next layer which needs to be negative at pH=7.4 is poly glutamic acid having the isoelectric point at pH=3.2.

Three cyto-*c*/poly glutamic acid layers were deposited into AAO. CD and Uv-Vis spectroscopy clearly shows building up these layers inside AAO. The UV-Vis spectroscopy shows an increase of adsorption lines upon increase of layers deposited. CD spectrum of deposited cyto-*c* inside AAO pores shows a peak around 237 nm. This peak is different from usual minima of cyto-*c* at 220 nm and 210 for helical structure in solution (Figure 4-7) [91]. These results showed that the interaction of AAO surface with proteins changes the structural properties of cyto-*c*.

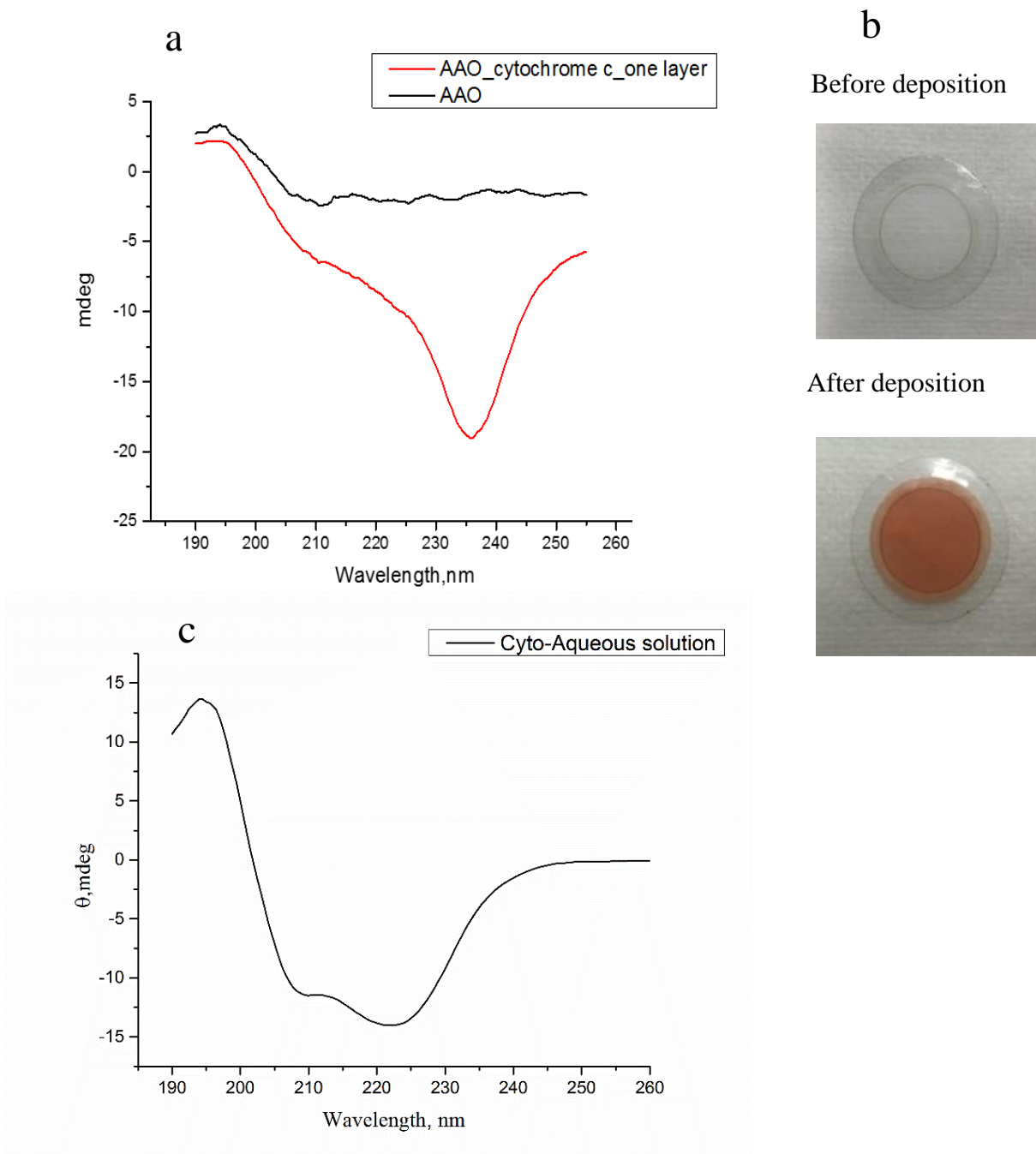


Figure 4-7 a) Far-UV CD spectra of AAO before and after deposition of cyto-c b) AAO membrane before and after deposition and c) far-UV CD spectrum of cyto-c in aqueous solution (0.2 mg/ml). Spectra were taken at 22 °C with scan rate of 20 nm/min.

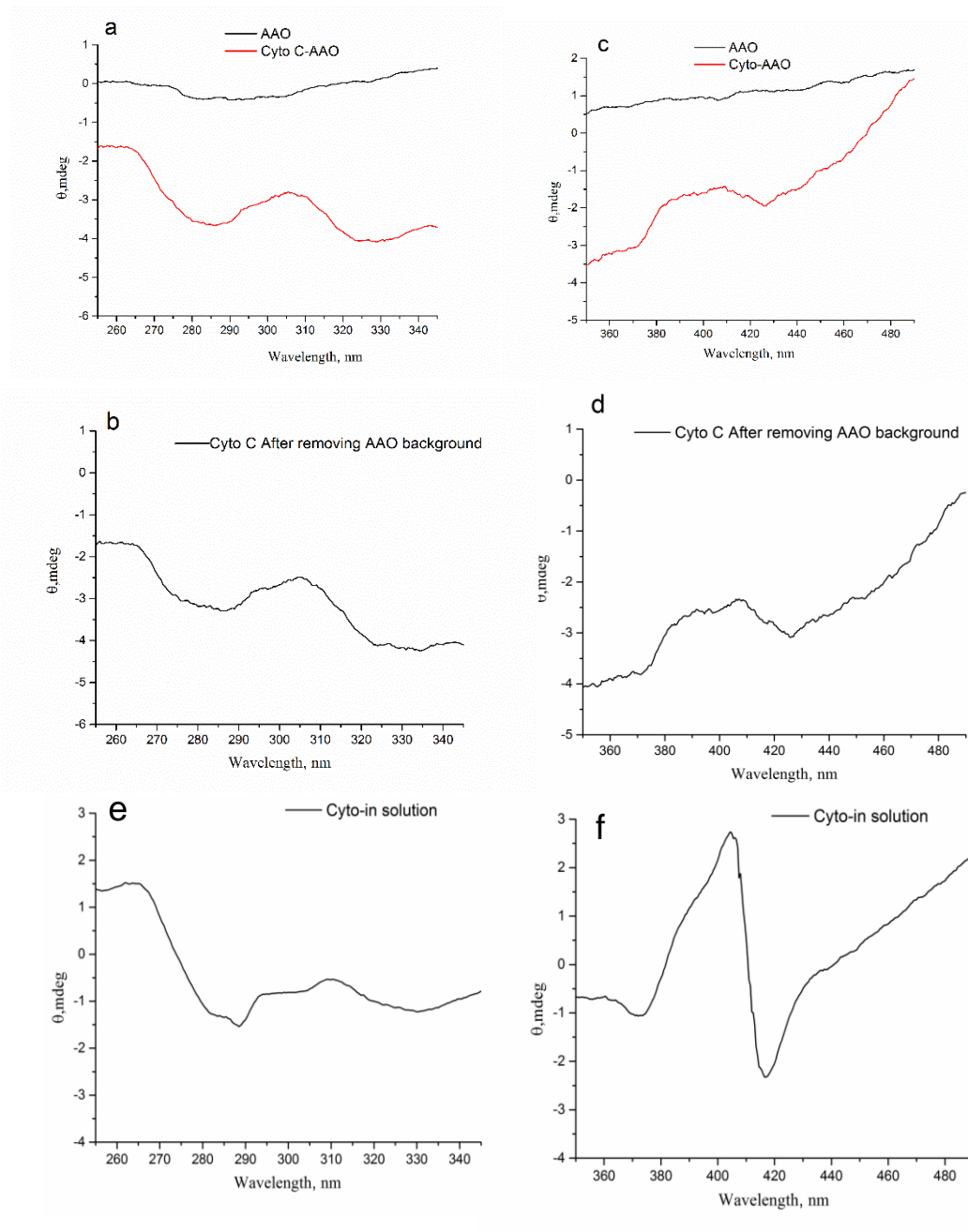


Figure 4-8 **Right:** Near UV CD spectra and **Left:** Soret region CD spectra; **a)** before and after deposition of cyto-c, **b)** “a” after subtracting AAO background, **c)** before and after deposition of cyto-c, **d)** “c” after subtracting AAO background. **e and f)** cyto-c in aqueous solution (1 mg/ml). Spectra were taken with scan rate 20 nm/min at 22^o C.

Information on packing in aromatic side chain can be obtained from CD spectrum between 250 and 330 nm (near UV). Two minima at 282 and 288 nm are expected to be observed for cyto-c in solution but those minima were not clearly observed in our spectra which means that cyto-c is bonded to AAO surface and do not show the same structure as in solution (Figure 4-8). This spectrum is similar to the one reported for cyto-c bonded to lipid vesicles. The packing of core residues of cyto-c can be disrupted upon bonding to the AAO surface resulting in disappearance of minima observed in solution [92].

The Soret region is where the wavelength are in the range of 350 to 490 nm, and its absorbance depends on spin state of hem iron. The Soret region absorbance plot for native cyto-c shows a maximum absorbance at 410 nm corresponding to the low state iron connecting to two ligands (Figure 4-9-left) [92], however the absorbance peak in AAO- cyto-c was observed to be at 407 nm (Figure 4-9-right) , a blue shift compared to the native cyto-c. This blue shift might be related to the binding of cyto-c to AAO where a disruption of ligand attached to hem iron occurs.

Soret region in CD spectra (Figure 4-8 c and d) provides some information about coupling of electric dipole transition moment in hem with aromatic residues in cyto-c [92]. The Soret region of CD spectrum for cyto-c deposited into AAO shows a peak at 407 nm (Figure 4-8 c and d). For native cyto-c, a sharp minima at 418 nm and for bonded cyto-c to the lipids, a single positive peak at 408 nm were reported. Any change in soret region compared to native proteins, can be interpreted as a disruption of coupling between hem transitions and

nearby aromatic residues in the protein [92, 93]. The solet region of CD spectrum for AAO-cyto-c is different from native structure and close to bonded cyto-c to lipid vesicles [92].

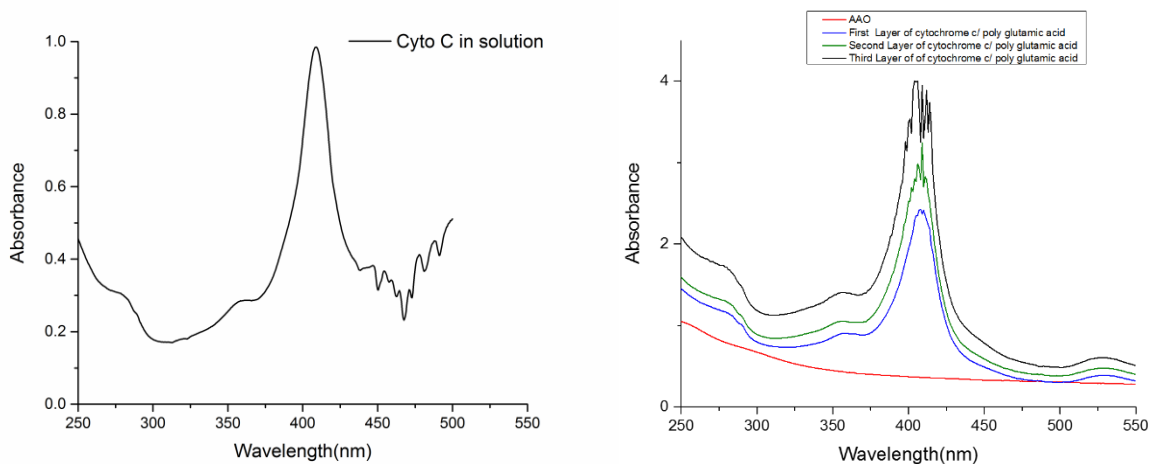


*Figure 4-9 Cyto-c absorbance in **left**) aqueous solution (1mg/ml) **Right**) Cyto-C layers deposited into AAO. Red line represents the he AAO absorbance. Absorbance peak in cyto-c solution is 410 nm and for one layer cyto-c deposited on AAO (blue line) is 407 nm.*

Protein-lipid mixture was also deposited into the AAO to study the oriented samples. WALP21 (contains tryptophan (W), alanine (A), and leucine (L) amino acids) as a hydrophobic transmembrane helix integrated in a lipid bilayer, DMPG, was prepared by Matthew P. Donohue in Smirnova's lab at NCSU, and we deposited this mixture into AAO. The oriented sample was reported to show the alignment of the helix respect to the bilayers with a broad peak at 225 nm to 230 nm [94, 95]. The CD spectrum of AAO-WALP-DMPG shows the same peak and shape as the oriented samples which implies the existence of ordered deposited lipid-

peptide inside the AAO pores, however the peak we observed in nanoporous AAO is more intense than those reported in planner quartz.

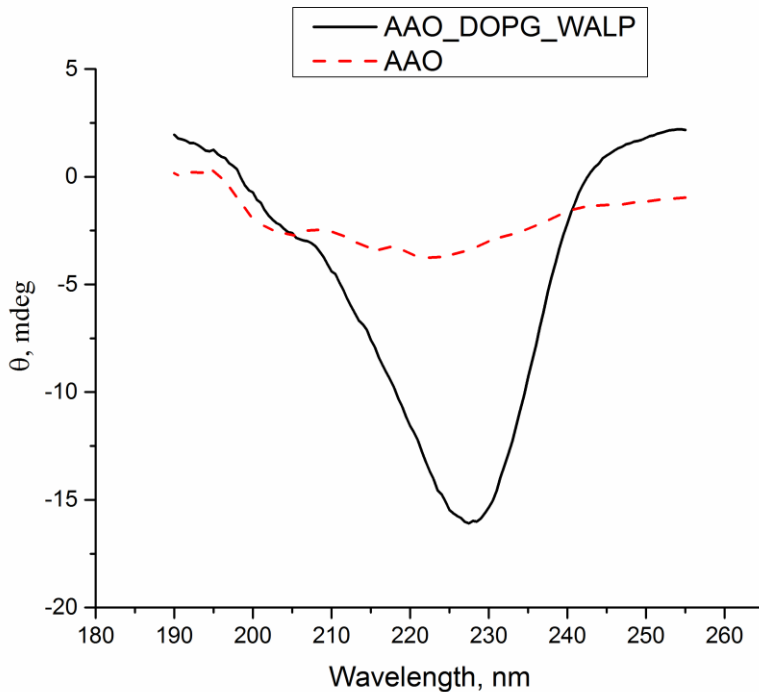


Figure 4-10 CD Spectra of AAO with (solid line) and without DOPG (dashed line) adopted with WALP peptide. The molar ratio of peptide to lipid was 1:150.

4.2.4 EPR and UV-Vis Spectroscopy of AAO

It was reported that AAO prepared by tartaric acid has a carbon radical and its intensity initially increased and then decreased by heating [96] but we observed a weak EPR signal in AAO prepared by phosphoric acid which might not be due to the carbon content and , and its intensity decreased by heating. Heating AAO to 900 °C removes the paramagnetic center in AAO, however it becomes fragile (Figure 4-11). The result of this study combined with UV-

UV-Vis spectroscopy would help anyone to use proper heat treatment when UV-Vis and CW and pulse-EPR spectroscopy are required for experiments involving AAO. The result of heat treatment shows that AAO is almost without any EPR signal when heated till 900 °C and heating up to 600 °C decreases the EPR signal intensity more than 50%. Some experiments such as DEER (Double Electron-Electron Resonance) in which the small signal of AAO impacts the result, AAO heat treatment is required before depositing lipid into the pores. The UV-Vis spectroscopy indicates that AAO shows different absorption lines when treated in various temperature. There is a signal appearing at 250 nm when AAO is heated up to 700 °C. This signal starts to decrease at 800 °C. This peak is close to peptide bond absorption, so if one needs to characterize peptides and proteins inside the pores in UV region, the AAO has to be heated up to at least 800 °C to obtain a transparent AAO in that region.

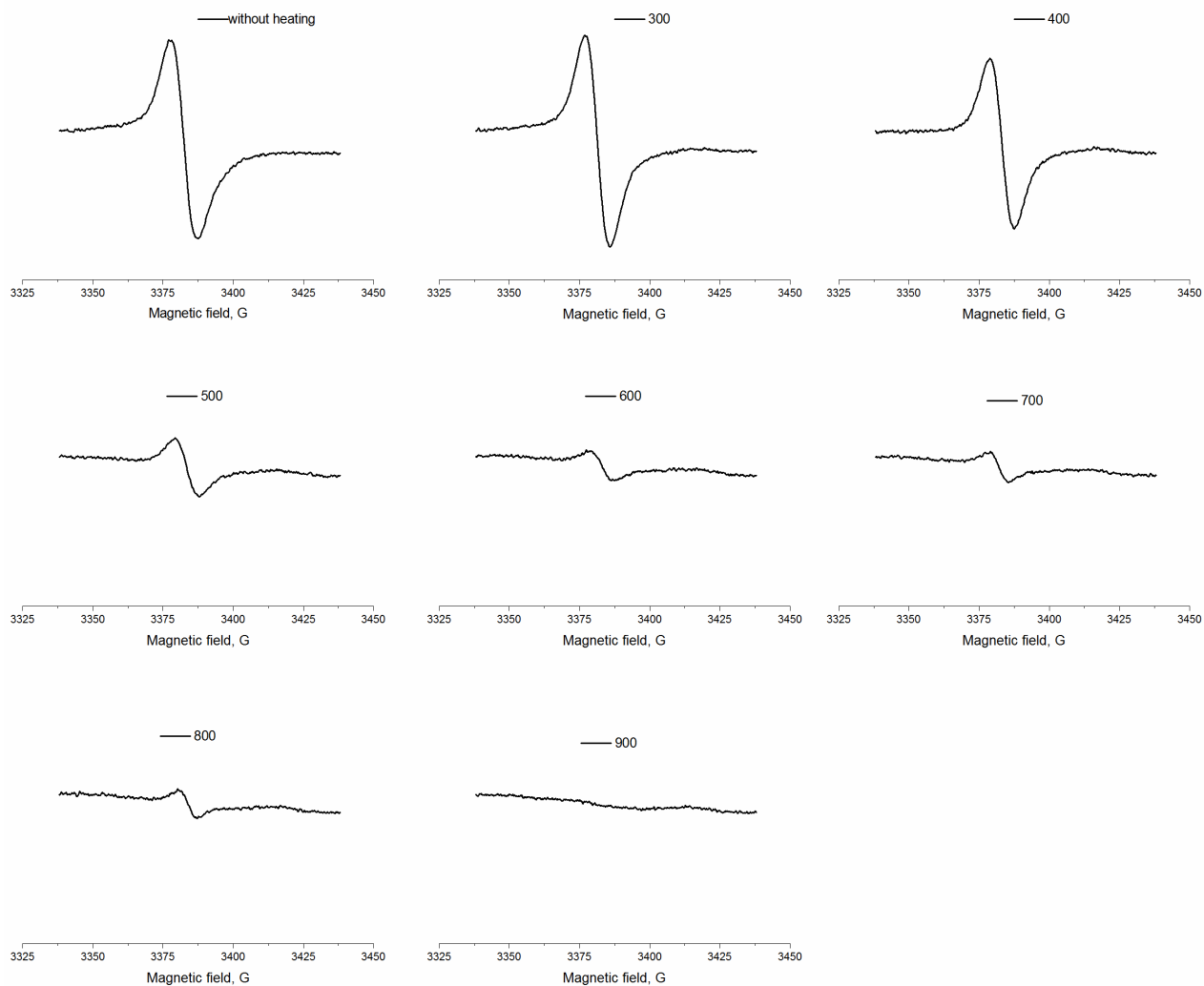


Figure 4-11 X-band EPR of AAO upon heating from 300 to 900 °C; each sample was heated with rate of 2 °C/min and kept at final temperature for 1 hr and then cooled down with rate of 10 °C/min to the room temperature. Each spectrum was taken with 1000 scans. The final temperature that AAO was treated at, is shown for each spectrum.

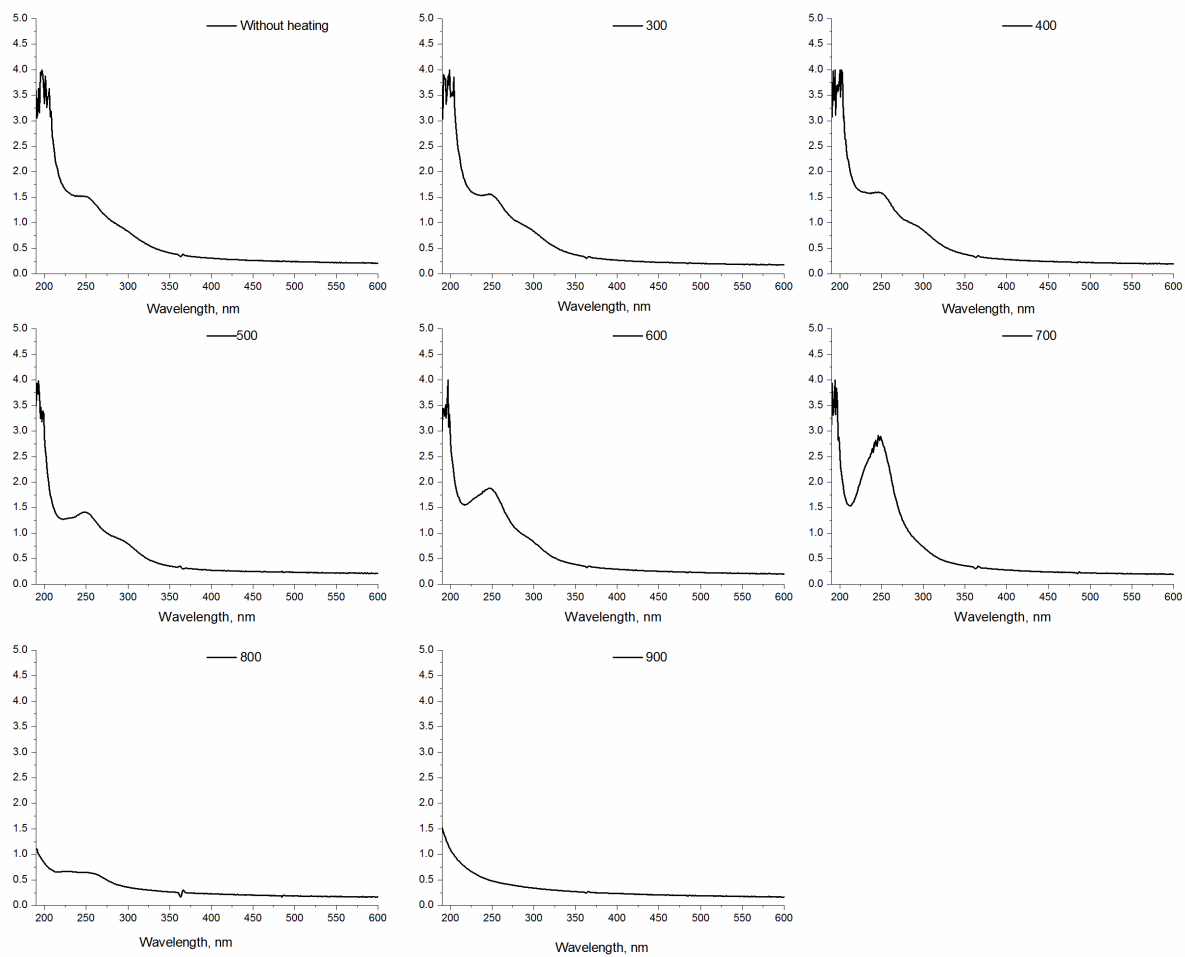


Figure 4-12 UV-Vis Spectroscopy of AAO treated at various temperature (shown on each spectrum). All spectrum were taken at room temperature and AAO was kept wet during measurement. The AAO samples were prepared and treated the same as for X-band EPR study in Figure 4-11.

4.2.5 Phase Transition of Nanopore Confined Lipid Bilayers As Studied by Quartz Crystal Microbalance (QCM)

In order to study the phase properties of lipid bilayers inside AAO, Quartz Crystal Microbalance (QCM) was used. QCM is a sensitive technique to the mass adsorption on the surface of quartz crystal. The piezoelectric quartz crystal is placed between two gold electrodes and frequency change of oscillating depends on the mass on crystal [97]. To use QCM for nanopore confined bilayer, Antonin Marek (NCSU, chemistry department) anodized the deposited aluminum on QCM crystal and prepared the AAO on QCM crystal, and we used AAO-QCM crystals to deposit lipids into the pores. Figure 4-13 shows a typical QCM crystal with AAO-lipid structure.

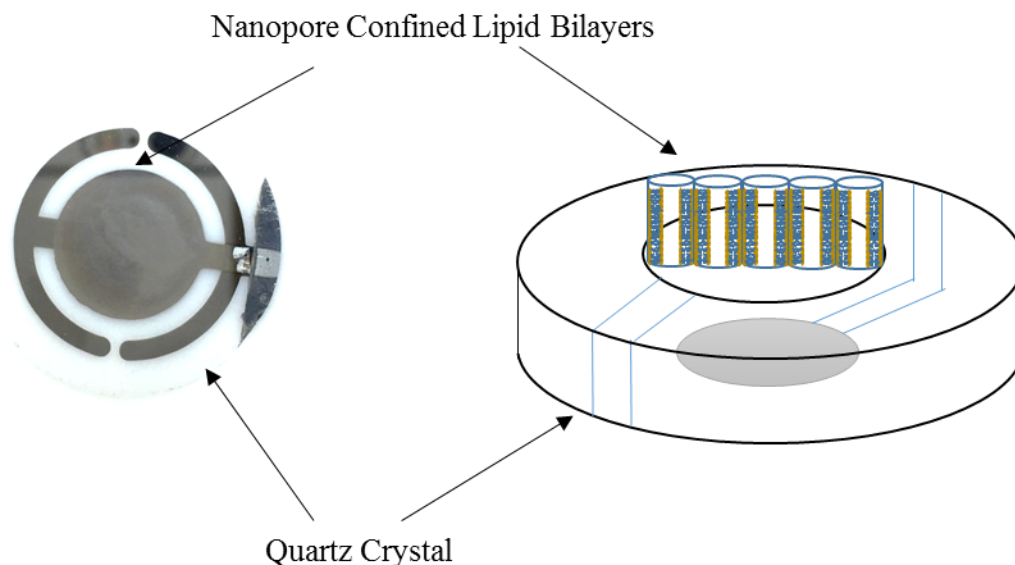


Figure 4-13 A Quartz Crystal Microbalance (QCM) crystal with nanopore confined bilayers (AAO-lipid).

The pore properties can be characterized by performing water adsorption/desorption isotherm on AAO-QCM. In this experiment, AAO-quartz crystal was placed in a vacuum chamber and water vapor is released to the chamber. The frequency of the crystal changes upon adsorption or desorption of water vapor. These changes were plotted versus reduced pressure (P/P_0). The higher the frequency, the less mass adsorbed on the surface.

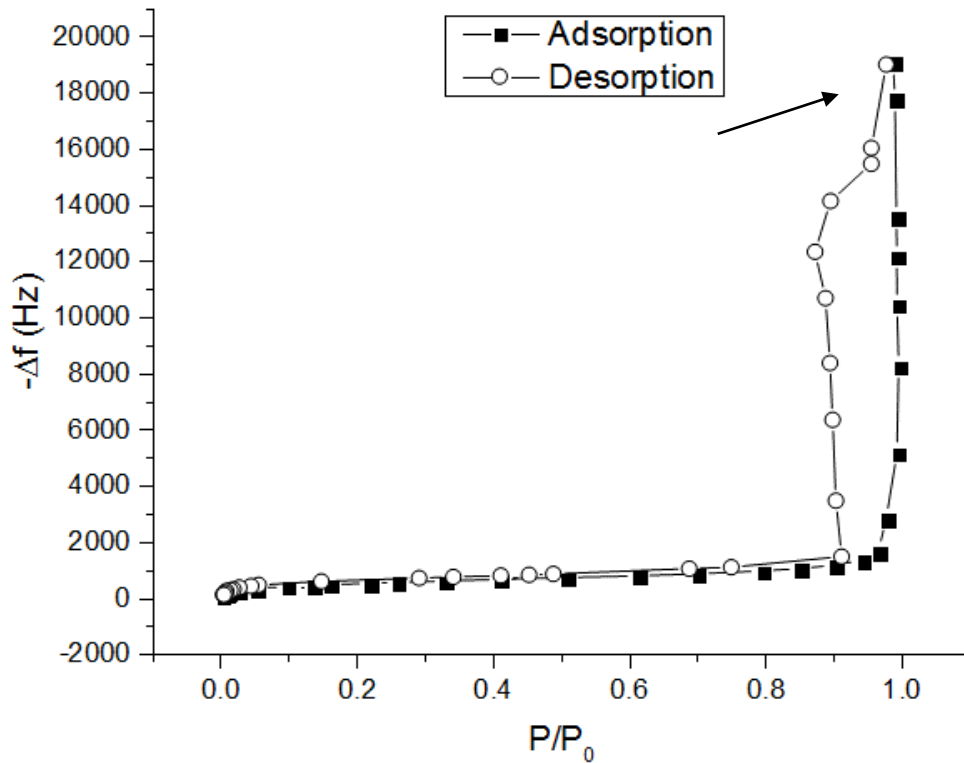


Figure 4-14 Water adsorption/desorption isotherm at 22 °C on AAO-quartz crystal. Arrow shows the frequency related to the end of hysteresis which was used to characterize the pore diameter.

The frequency change is directly proportional to the amount of mass adsorbed on the crystal surface. The water vapor volume adsorbed into the pores is given by:

$$v_p = \frac{(\Delta f_h)ZA_e}{(2f_0^2)\rho} \quad 4-1$$

where Δf_h is the frequency change at the end of hysteresis (arrow in Figure 4-14), f_0 is the initial resonance crystal frequency, A_e the area of top surface of electrode (0.28 cm^2) and $Z=9507260 \text{ kgm}^2\text{s}^{-1}$ [98]. Approximately, 20000 Hz change in frequency upon adsorption of water vapor was observed along with type IV hysteresis which is a characteristic of mesoporous material based on IUPAC calcification [99].

The pore diameter can be calculated from the relationship between the surface area and total pore volume:

$$d = \frac{4v_p}{A_s} \quad 4-2$$

where A_s is the total surface area of the pores on the crystal.

To calculate the surface area, Brunauer-Emmett-Teller (BET) theory was used [100]. This theory is based on multilayer adsorption and at relative pressure (P/P_0) between 0.05 to 0.035 where the following equation is applied:

$$\frac{p}{v(p_0 - p)} = \frac{c - 1}{v_m c} \left(\frac{p}{p_0} \right) + \frac{1}{v_m c} \quad 4-3$$

where v is the volume of adsorbed gas (water vapor), p is the vapor pressure at time t and p_0 is the maximum water vapor pressure. v_m is the adsorbed monolayer gas, and c is related to the affinity of gas to adsorb on a solid surface. Frequency change is directly proportional to the volume of gas adsorbed on a QCM crystal, therefore plotting $P/(\Delta f(P_0-P))$ against P/P_0 results in a BET plot based on crystal frequency (Figure 4-15). The intercept and slope of such a plot provide constant c and v_m .

Surface area can be then calculated from the monolayer adsorbed gas (v_m):

$$A_s = \frac{v_m N_A s}{V} \quad 4-4$$

where V and s are the molar volume and adsorption cross section area of adsorbed molecule and their values for water are $18 \times 10^{-6} \text{ m}^3$ and 0.114 nm^2 respectively.

The surface area and pore diameter for prepared AAO-QCM crystal was found to be 81 cm^2 and 52 nm respectively, which indicates the presence of a highly porous surface on quartz crystal.

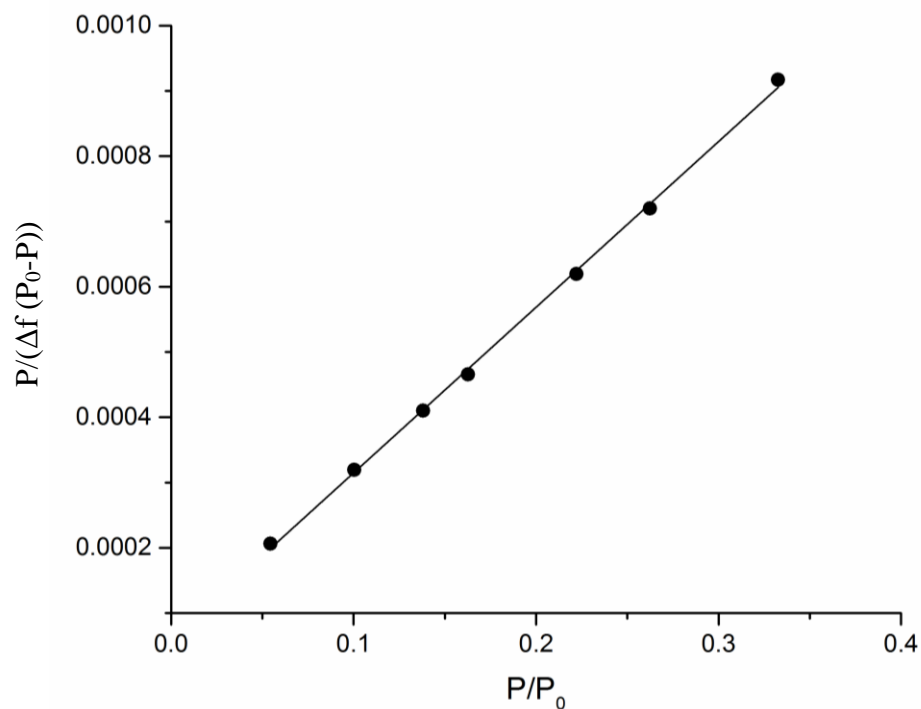


Figure 4-15 BET plot for AAO-QCM crystal obtained from adsorption plot of water adsorption/desorption isotherm at 22 °C.

DMPC lipid were deposited on QCM-AAO crystal to study the phase transition and peptide interaction. DMPC has a main phase transition temperature around 24 °C. Figure 4-16 shows the frequency of quartz crystal with AAO-DMPC bilayer changes at different temperatures. The voltage and frequency change of the crystal are plotted against temperature.

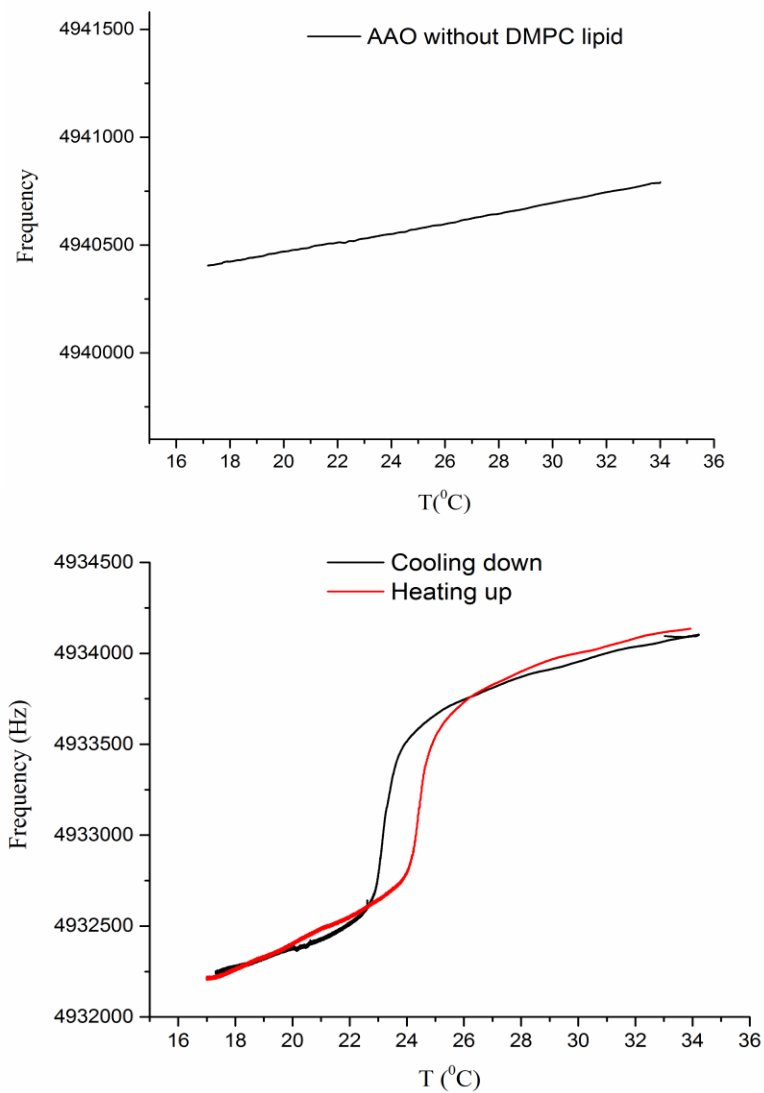


Figure 4-16 Frequency change of QCM-AAO crystal with and without DMPC deposited on compared to the original 5 MHz frequency of crystal without lipid and AAO (f_0); the main phase transition is about 24°C. To compare two plots, the Δf interval scale in frequency axis was kept the same.

The frequency change on DMPC on a flat surface crystal was reported and the frequency change was reported to be about 1.5 Hz at phase transition [101]. The change that was observed for our sample was about more than 1000Hz. This difference is because of having more lipids deposited in porous sample due to higher surface area of porous AAO compared to flat glass crystals. This clearly shows that using AAO on QCM crystal provides a promising tool to study phase transition or even interaction of proteins with confined lipid bilayer. The frequency differs from the original frequency (5MHz) depending on mass and viscosity of deposited lipid. As it is shown in Figure 4-16, the frequency in liquid phase is higher than that of in the gel phase, which might be due to higher viscosity in gel phase at low temperature. The lipids become more packed and lipid bilayer thickness increases as they undergo transition from liquid to gel phase which decreases the oscillation frequency of quartz crystal. The main phase transition temperatures are at 24.4 and 23.3 °C during heating and cooling respectively. There is a hysteresis observed between cooling and heating plot which is related to the difference between ordering and disordering mechanism of lipids upon cooling and heating. For DMPC on flat surface the main phase transition was reported to be 23.8 (heating) and 20.8 °C (cooling), however the resolution was poor [101], therefore employing AAO increased the amount of lipid deposited which results in an increase in the frequency change and consequently the higher resolution and accuracy were obtained. lipid phase transition hysteresis is not completely understood but it has been shown that lipid chain length plays important role in this phenomena and lipids with shorter acyl chain shows less hysteresis width [102].

The same result was obtained from the change of QCM voltage in which there is a sudden change in voltage at lipid phase transition range.

The voltage which is the maximum amplitude of oscillation is inversely proportional to dissipation factor. Dissipation factor is a parameter in QCM which defines how much energy dissipated during oscillation of quartz crystal [103].

The voltage is showing the crystal dissipation of energy upon cooling and more energy dissipated when lipids undergo transition from liquid to gel phase. The hysteresis between cooling and heating scans is also observed in this plot. These results are promising result to introduce a biosensor for studying phase properties, interaction of proteins or any interacting material with confined lipid bilayers.

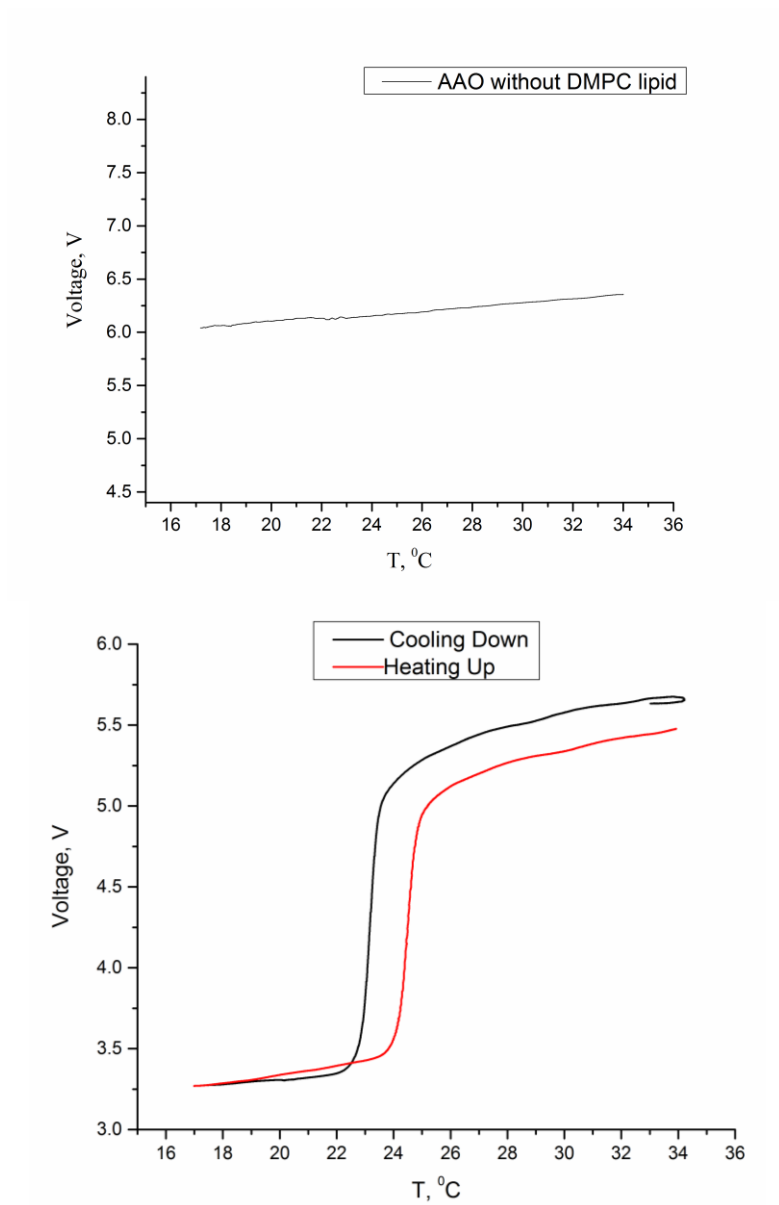


Figure 4-17 Voltage change of QCM-AAO crystal with DMPC deposited on; to compare two plots, the voltage scale intervals were kept the same.

4.2.6 Melittin-Lipid Interaction

Melittin can be found naturally in honeybee venom and is a peptide model for interaction study between lipid and antimicrobial peptides. It has 26 amino acids and by formation of α -helix structure and hydrophobic interaction it associates with many phospholipid bilayers and adsorbs on their surface following by formation a cylindrical pore which eventually disrupt the membrane [104]. Any factor such as temperature or addition of charged molecules which can affect the hydrophobic, electrostatic interaction and helix formation, are important in melittin interaction with membrane [105]. Many techniques such as NMR [106, 107], confocal laser scanning microscopy [108] and QCM [109] for supported lipid bilayer in flat surface were used to study kinetics and the mechanism of melittin effect on lipid bilayer, here we used QCM to detect the interaction of melittin with oriented lipid bilayers inside AAO nanopores. For NMR studies, defining the initial time of melittin effect is not accurate enough due to sample preparation, but in QCM, the exact initial effect of melittin on supported lipid bilayer can be detected. Here we deposited DMPC on QCM-AAO and effect of adding melittin versus time was studied. Figure 4-18 shows after melittin addition with the total concentration of 10 μ M, it immediately adsorbs on the surface of the lipid bilayer (A in Figure 4-18) and then penetrates into the lipid bilayer and disrupts it (B in Figure 4-18). This short but useful result shows that lipid deposited on AAO-QCM crystal can be used as a very sensitive technique to study protein-lipid bilayer interaction.

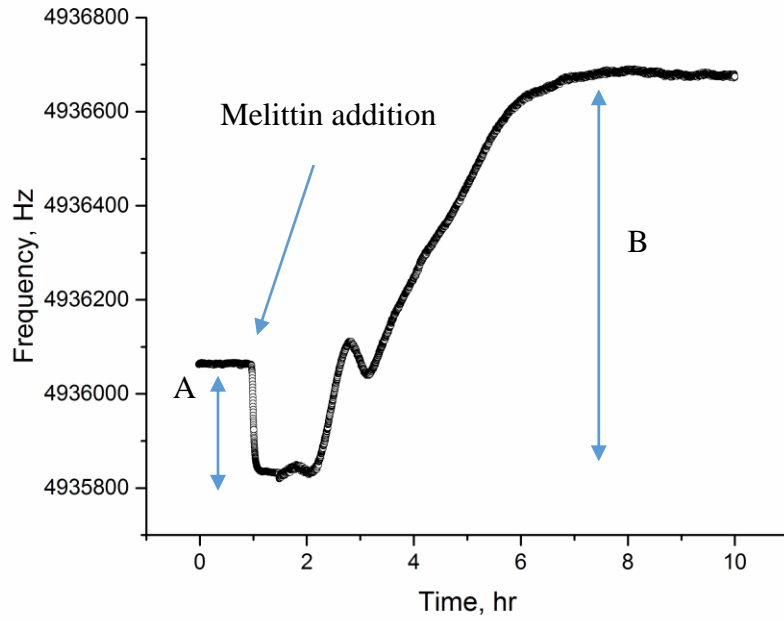


Figure 4-18 Melittin effect on nanopore confined lipid bilayer, A: Adsorption of melittin on the surface, B: disruption of lipid bilayers.

4.3 Conclusions

Nanopore confined bilayer as model of curved and confined lipid bilayer was prepared and studied. The lipid bilayer has interaction with aluminum oxide surface and shows different behavior than that of in vesicles. The surface potential was measured with EPR titration method described in chapter 3 and it was shown that surface potential of POPG lipids inside the AAO pores are higher than that of in vesicles, which is due to highly ordered and packed lipids inside AAO nanotubes. AAO surface charge and its spectroscopic properties were investigated and it was found that AAO showed a weak signal in X-band and if the deposited sample signal is not strong enough, the AAO signal becomes significant and it is needed to heat the AAO up to 900 °C to become EPR signal free. UV-Vis spectroscopy on AAO samples treated from 300 to 900 °C showed that AAO in UV region can be used if heated to at least up to 800 °C. Zeta potential measurements on AAO samples indicated that AAO is negatively charged at pH higher than 2.3. This negatively charged surface can be used to prepare protein nanotubes inside AAO pores based on electrostatic interactions. Cytochrome c and poly glutamic acid as positively and negatively charged macromolecules in physiological pH (7.4) were used to prepared multilayer protein nanotubes. The UV-Vis and CD spectroscopy of these samples showed layer by layer deposition of 3 double layer of cytochrome c-poly glutamic acid. The comparison of CD and UV-Vis spectroscopy in various wavelength regions for native and deposited cytochrome c indicated that the structure of cytochrome c is disrupted when attached to AAO surface.

Transmembrane structure of WALP peptide in DOPG lipids deposited into AAO was investigated by CD spectroscopy and it was found that WALP peptide shows an oriented structure when lipids are confined by AAO pores, which indicates the formation of ordered lipid bilayer arrays inside the pores.

Nanopore confined bilayer placed on QCM crystal can be used as “biosensor” and lipid phase properties inside pores were studied by QCM technique. The main lipid phase transition of DMPC was observed in high resolution as a sudden change in QCM frequency and voltage. The interaction of peptide with nanopore confined bilayer was studied using antibacterial peptide model, melittin, and its adsorption on lipid surface and later disruption of lipid bilayer were observed with quartz crystal frequency changes. It was shown that QCM-AAO-Lipid is a good system to study interaction and binding of peptides on the surface of lipid bilayers.

These observations show a great potential of QCM-AAO systems to use as biosensor to study lipid or protein properties inside the pores.

Chapter 5. Hydrogen Bonding through Lipid Bilayers as Assessed by ESEEM and HYSCORE

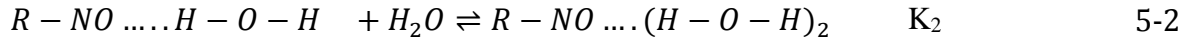
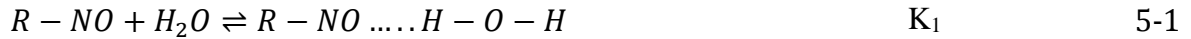
5.1 Introduction

Hydrogen bonding along with electrostatic interactions play important roles in protein folding, enzyme activities and the insertion of membrane protein inside lipid bilayer [110]. For instance, arginine amino acids in S4 peptide are hydrated and stabilized through hydrogen bonding inside the alkyl chain region [111]. Water penetration and polarity profile inside the lipid bilayers are important factors in membrane permeability and transmembrane helices stability [112]. Water penetration study in vesicles also provides useful information about the defects and packing differences at different curvatures as discussed in Chapter 3.

Evidence for water penetration and effect of solvent in biological membrane has been shown by studying hyperfine splitting in X-band EPR spectra [1]. Water concentration profile across membrane has been reported by measuring isotropic hyperfine coupling of a nitroxide radical and the isotropic hyperfine splitting constant was plotted against the hydrogen donor concentration (e.g. water) in a binary solvent mixture with nitroxide radical (16-(4,4-dimethyloxazolidine-N-oxy)stearic acid (16-SASL)), however it was assumed that THF (tetrahydrofuran) showed a similar behavior to water in a non-polar environment and it was used as a similar model to water in non-polar environment to calculate some required constants [113]. Isotropic hyperfine splitting was obtained from experimental X-band EPR and has been used to find the polarity profile across lipid bilayers [114].

Magnetic parameters obtained from EPR studies of nitroxides can be used to investigate the local solvent polarity and hydrogen bonding to the nitroxide radical. For instance A_{zz} and g_{xx} extracted from W-band EPR are sensitive parameters to the electric field along NO group and the hydrogen bonding of nitroxide. Analysis of W-band EPR parameters and molecular dynamic simulation showed that water penetration could be the reason for hydrogen bond formation with nitroxide observed in lipid bilayer [115].

Nitroxide is capable of formation of two hydrogen bonds, and these two hydrogen bonds formation equations can be written as:



These two H-bond formation constants (K_1 and K_2) affect spectral properties of EPR techniques.

In CW-EPR spectroscopy, hyperfine splitting and g tensors were measured to detect water molecules. These parameters (g factor and hyperfine splitting) are dependent on the local dielectric constant and their changes were used to indirectly detect local water concentration.

To directly detect local water concentration and hydrogen bonding, ESEEM spectroscopy was used. The simulated spectra using DFT calculation was used to obtain the water penetration profile across the membrane [116]. ESEEM is able to detect anisotropic hyperfine interaction with nearby nuclei. Two-pulse and three-pulse ESEEM were used to obtain local water concentration [112, 117], however, HYSCORE can be used to obtain local

water concentration closer to the nitroxide radical, since in HYSCORE, we are able to probe the hyperfine interactions in shorter range from nitroxide radical compared to three-pulse ESEEM. To the best of author's knowledge, this is the first time that HYSCORE was used to detect the water and hydrogen bonding formation inside lipid bilayer. General introductions in HYSCORE and ESEEM are provided in Chapter 1. Here we compare these two techniques and explain how to interpret the spectra to detect the local water molecules. To study the effect of curvature, water penetration into small and large unilamellar vesicles were then investigated by these techniques.

5.2 Results and Discussion

5.2.1 X-band EPR

To investigate the hydrogen bonding by ESEEM and HYSCORE, a glass forming solvent is needed because the experiments were performed at 77 K. A glass forming solvent is defined as a solvent in which the nitroxide radical does not aggregate at low temperature. In order to detect hydrogen bonding solely from water, solvent must not form any hydrogen bonds with nitroxide and it has to be miscible in water as well. Glycerol is known to form glass when mixed with water [118] but it can form hydrogen bonds with nitroxide radical which is not favorable. Diglyme (1-Methoxy-2-(2-methoxyethoxy)ethane) is a dimethyl ether of diethylene glycol and its glass forming capability was studied by X-band EPR spectroscopy at 77 K in various water concentrations.

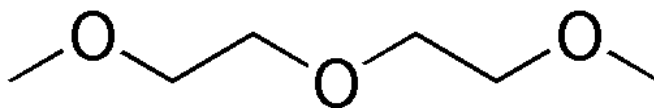


Figure 5-1 chemical structure diglyme used as glass forming solvent.

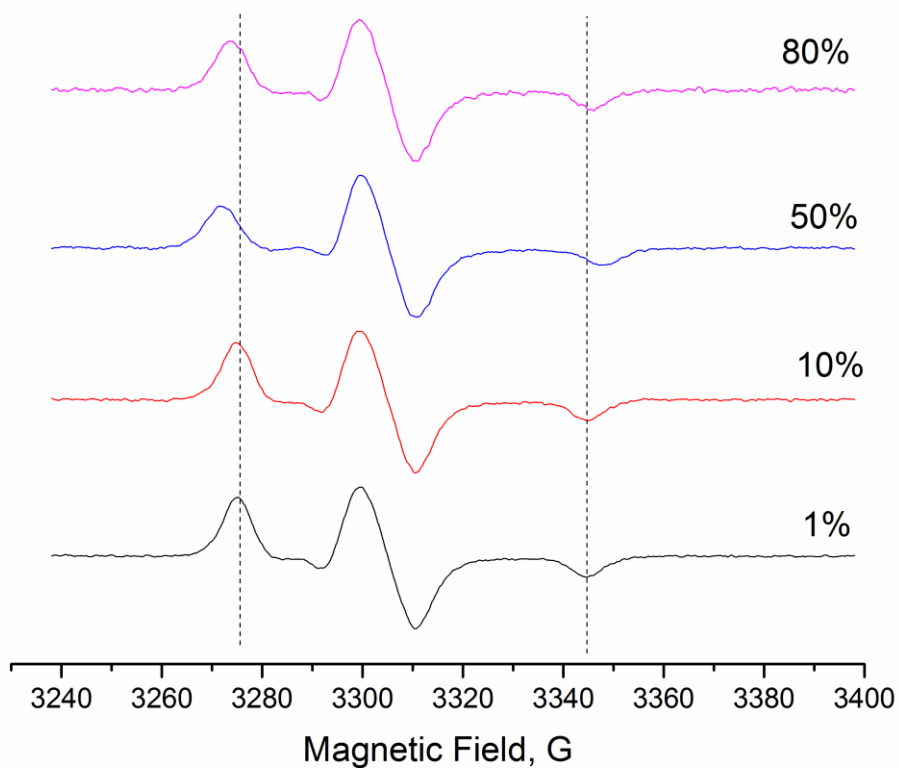


Figure 5-2 X-band EPR spectra of H₂O/diglyme mixture (Vol. %) with 1 mM TEMPO at 77 K. Dashed lines show how the outer hyperfine changes upon increasing H₂O percentage.

As it is seen in Figure 5-2, mixture does not show any appearance of a second component in X-band EPR which is an indicative of glass forming solvent, however the hyperfine and spectra parameters change as a result of polarity difference between the mixtures

at different water contents. At high concentration of water (80 %), the parallel hyperfine (the difference between two dashed lines in (Figure 5-2) does not follow the trend from 1 to 50 % and becomes smaller than that of 50 % water content. This suggests that water might crystallize partially and does not form a complete glass at concentration higher than 50%. We will confirm this later with 3-pulse ESEEM results as well. This solvent was selected for HYSORE and ESEEM study of the hydrogen bonding of water (up to 50 v/v %) and methanol with the nitroxide radical.

5.2.2 ESEEM of D₂O and CH₃OD in Diglyme

Different mixtures of D₂O/diglyme with 2 mM TEMPOL (nitroxide radical) were prepared and three-pulse ESEEM spectrum for each of them was obtained. The three-pulse ESEEM is capable of detecting the interaction of D₂O molecule with nitroxide radical. Deuterated water was used to distinguish the interaction of water hydrogens from other hydrogen atoms in matrix. The time domain spectrum was obtained and converted to frequency domain spectrum by Fourier transformation. The 3-pulse ESEEM was performed with 222ns delay between the first and the second pulses to observe all deuterium interaction since those interaction frequencies are not placed in blind spots when time delay is 222 ns. The time domain spectrum phase and baseline were corrected, and processed with a Hamming window, zero filling and Fourier transformation using Xepr data acquisition and processing software provided by Bruker to obtain the frequency domain spectrum.

Hamming window removes high frequency noises and the baseline correction removes the artifacts which can be observed after Fourier transformation. Figure 5-3 and Figure 5-4 are showing the time and frequency domain spectrum for 10 % (v/v) of 70 % (v/v) D₂O/H₂O in diglyme.

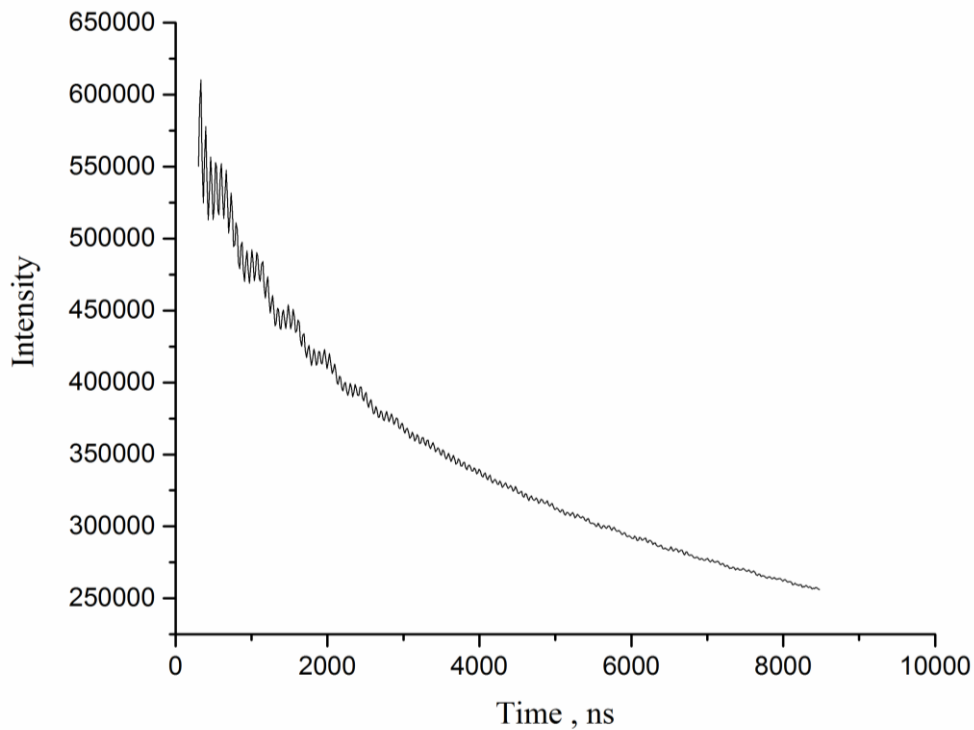


Figure 5-3 Three-pulse ESEEM time domain trace for 10 volume % of D₂O/H₂O (70 % v/v) in diglyme.

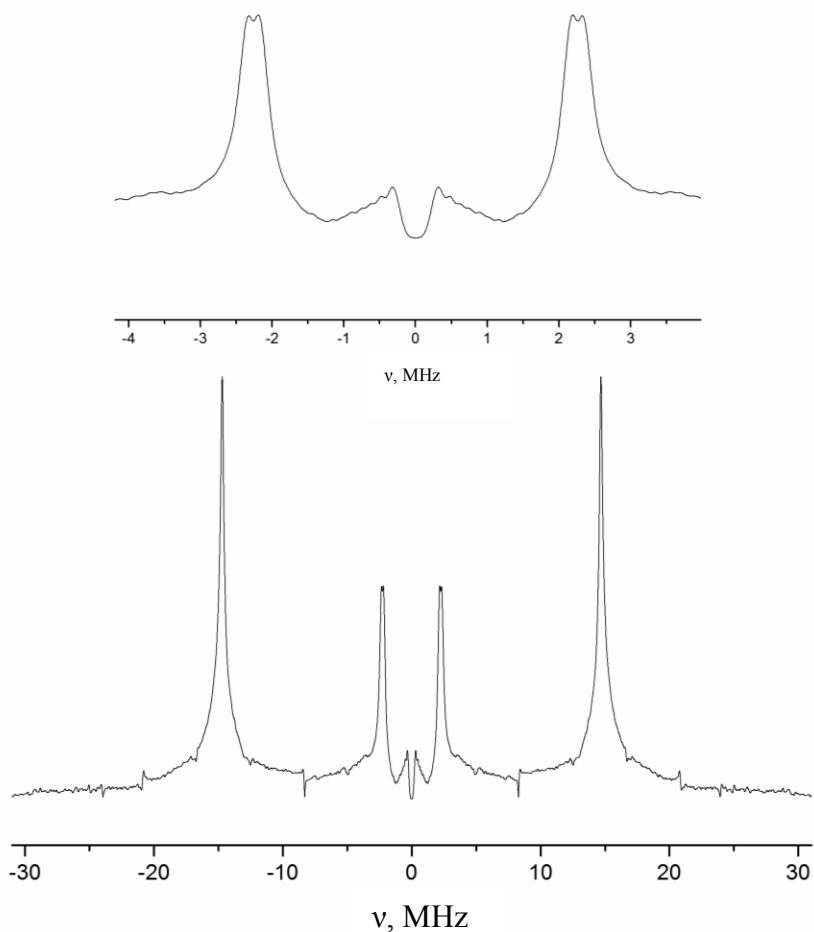


Figure 5-4 Fourier transformation of three-Pulse time domain for D₂O in diglyme: 10 volume % of D₂O/H₂O in diglyme. The top plot is zoom-in part of the ESSEM related to deuterium (D₂O) frequency (matrix deuteron signal).

The deuterium Larmor frequency at 2.3 MHz and that of protons at 14.6 MHz are seen in ESEEM spectrum (Figure 5-4). These two peaks are composed of a sharp peak with a broader background peak (which is not well resolved). The peak at 2.3 MHz is related to deuterium interaction coming from D₂O, however its amplitude corresponds to the bulk water concentration plus hydrogen bonded water molecules to the nitroxide. The broad background

of a sharp deuterium peak in three-pulse ESEEM comes from two hydrogen bonding sites of nitroxide. A doublet splitting observed at $\nu=2.3$ MHz (see the zoom-in plot in Figure 5-4) is due to the weak nuclear quadrupole interaction of deuterium nuclei [116, 117]. Nuclear quadrupole interaction as a result of the interaction between quadrupole moment and electric field created by a nearby electron and nuclei is observed when $I>1/2$ in which the nucleus has non spherical charge distributions [8]. This explains why this splitting is not observed at $\nu=14.6$ MHz which is the frequency of ^1H in the matrix.

We investigated the dependence between the height of matrix deuterium amplitude and D_2O concentration in diglyme. Matrix deuterium appears at the frequency position corresponding to Zeeman frequency of nearby nuclei, and it is related to the matrix of the sample which results in a very weak interaction between nuclei and an unpaired electron. The contribution of matrix peak is approximately within 1 nm distance from the nitroxide radical, and thus it should be proportional to the local concentration of D_2O . The amplitude of matrix peak versus D_2O concentration can be plotted by taking three-pulse ESEEM in various D_2O concentrations in diglyme.

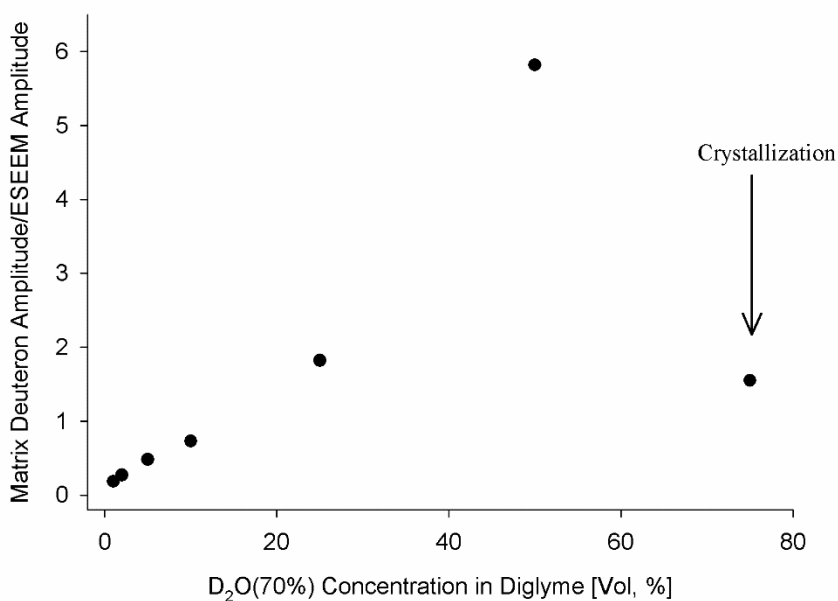


Figure 5-5 The matrix deuteron amplitude of three-pulse ESEEM dependency to the D₂O (70 % D₂O/H₂O) concentration in diglyme.

The matrix peak was normalized to account the TEMPOL radical concentration differences with dividing the height of the matrix peak by echo amplitude which is determined from time domain three-pulse ESEEM. As it is shown in Figure 5-5, at very high concentration of water, the mixture does not provide a good glass forming matrix and some of the water molecules were pushed out from formed glass and the nitroxide radical started to aggregate, therefore the D₂O matrix intensity around nitroxide dropped when crystallization happened. The intensity (y axis) is proportional to the local D₂O concentration of the matrix up to 1 nm and two D₂O molecules bonded to nitroxide radical, therefore three-pulse ESEEM itself was not able to distinguish hydrogen bonded D₂O and local concentration of D₂O in the matrix.

The nonlinear relationship observed in the plot corresponds to the hydrogen bonding formation.

In order to detect D₂O molecules bonded to the nitroxide, HYSCORE spectra were taken at 77 K. HYSCORE signal corresponding to deuterium was normalized using dividing by the echo amplitude to account the TEMPOL concentration. The echo amplitude was determined from three-pulse ESEEM and for each HYSCORE spectrum, a three-pulse ESEEM spectrum with the same setting was obtained.

The same approach was used to detect the hydrogen bonding formation between the methanol and nitroxide radical. In contrast to water, methanol forms glass in the entire concentration range, therefore HYSCORE and three-pulse ESEEM were obtained up to 100 % methanol. The ESEEM spectrum shows the same features as it was observed for water (Figure 5-6).

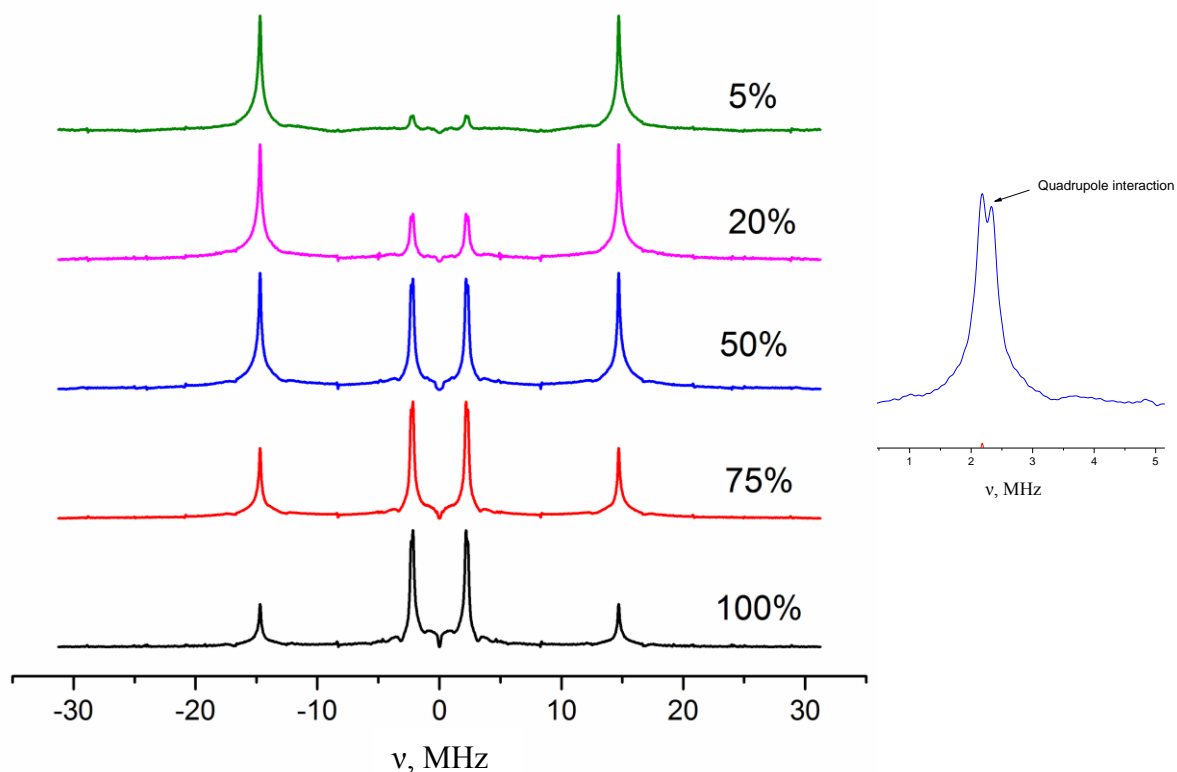


Figure 5-6 Three-pulse-ESEEM of different mixtures of CH₃OD/diglyme (Vol. %) with 2 mM TEMPOL. The intensity was normalized for the comparison; one should compare the ratio of deuterium peak (at 2.3 GHz) with respect to the ¹H matrix peak at 14.6 GHz. Right: zoom-in ESEEM of 50 % CH₃OD/diglyme which shows the splitting caused by quadrupole interaction between ²H and electron spin.

The amplitude of each deuterium matrix was normalized with the same way explained for water and was plotted against the ethanol percentage concentration.

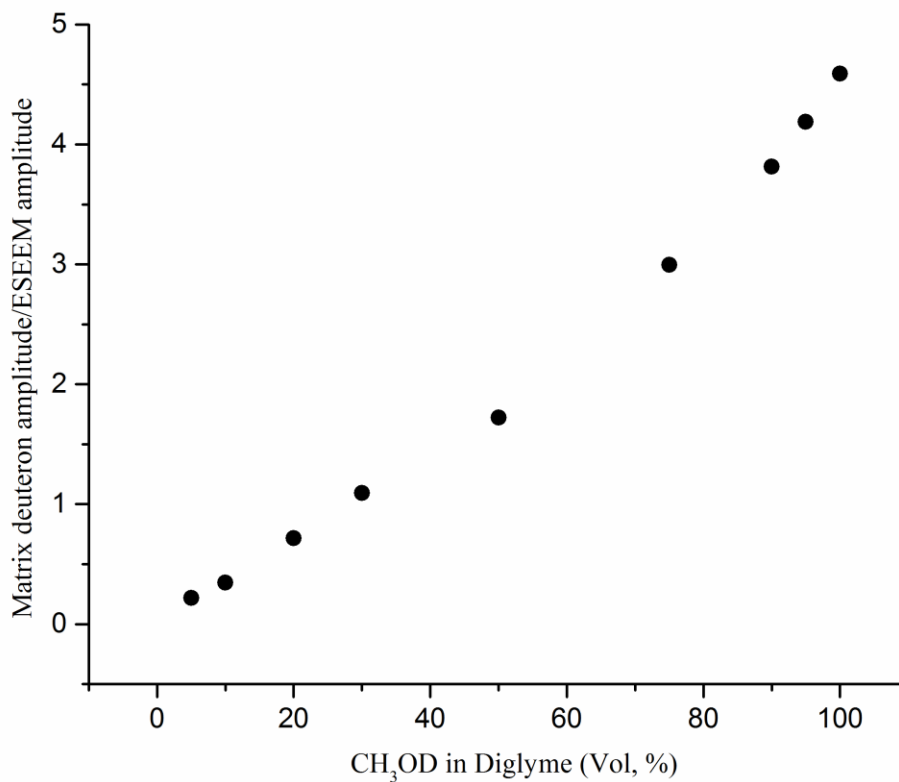


Figure 5-7 The matrix deuteron amplitude of three-pulse ESEEM dependency to the CH₃OD concentration in diglyme. The deviation from linear dependency is as a result of hydrogen bond formation with nitroxide radicals.

The relationship between CH₃OD concentration in DMSO and ESEEM deuteron amplitude was studied before [117] and they tried to exclude the hydrogen bonding contribution by looking at the splitting intensity shown in Figure 5-6, however since the matrix peak in ESEEM has two contributions to unattached and attached water (or ethanol) molecules, the amount of uncertainty is high to directly detect the hydrogen bonded molecules to the

nitroxide radical. Therefore we used HYSCORE to resolve the hydrogen bonded molecules intensity.

5.2.3 HYSCORE of D₂O and CH₃OD in Diglyme

HYSCORE is a two dimensional mode of three –pulse ESEEM, and can be used to detect the weak interactions between electron spin and nuclei in the vicinity . The HYSCORE spectra for different D₂O and CH₃OD concentration were obtained at 77 K. The time domain spectrum in each dimension was processed by removing background, applying Hamming function, zero filling and Fourier transform using X-EPR Bruker software.

Figure 5-8 shows the HYSCORE spectrum of 50 v/v % D₂O/H₂O (70 %) in diglyme. Peaks corresponded to the matrix proton frequency, H-bonded deuterons, and protons in TEMPOL are shown in the whole spectrum. The sky line projection of spectrum shows the location and the intensity of peaks. As it is shown, the H-banded deuterons can be well detected with higher resolution comparing to ESEEM. The intensity of the peak at $\nu=1.8$ GHz or 3.0 GHz corresponds to the concentration of deuterons bonded to the nitroxide through hydrogen bonding. Therefore HYSCORE makes it possible to detect solely hydrogen bonded waters with higher accuracy and resolution. This feature is not well resolved in three-pulse ESEEM.

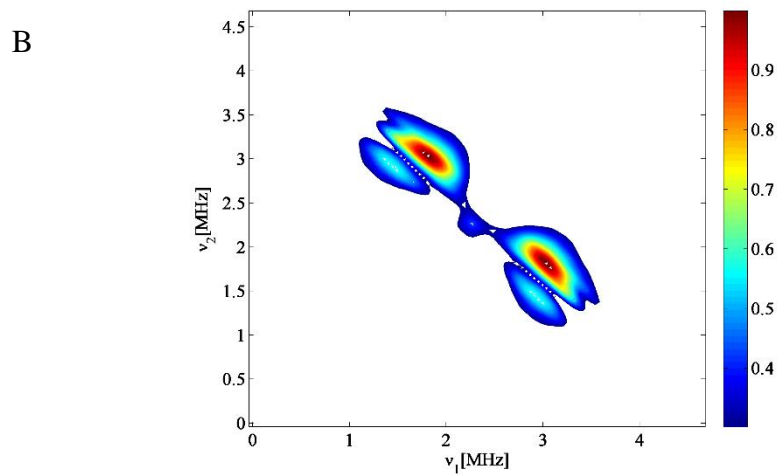
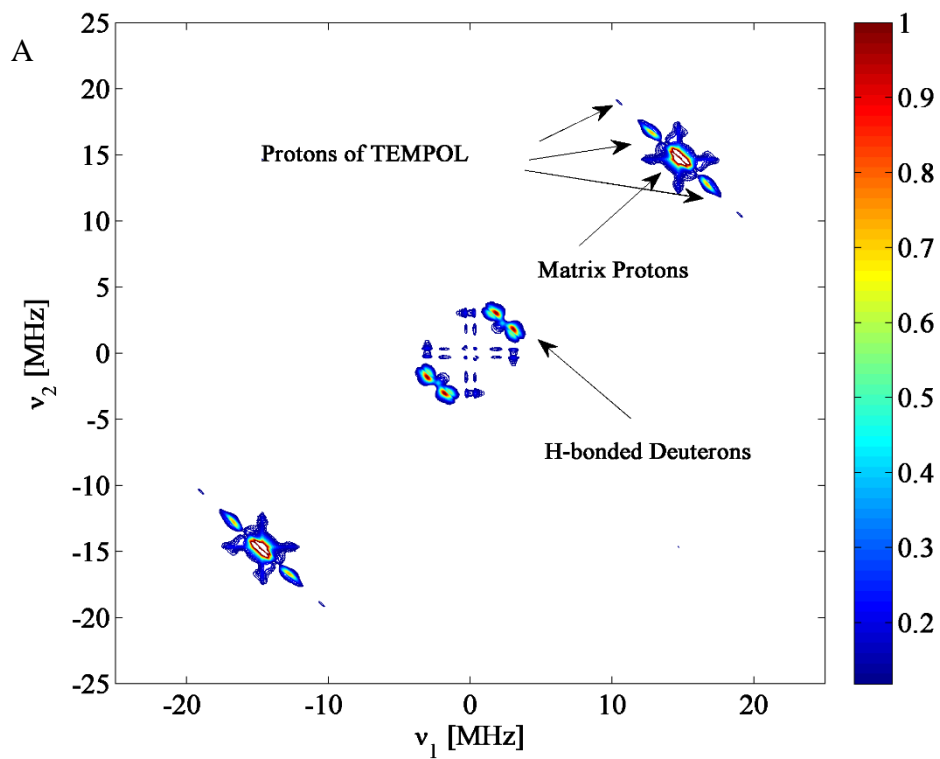


Figure 5-8 A) Contour presentation of HYSCORE for 50 v/v % D_2O/H_2O (70 %) in diglyme with 2 mM TEMPOL at 77 K. B) Cross-peaks from Deuterons H-bonded to NO group.

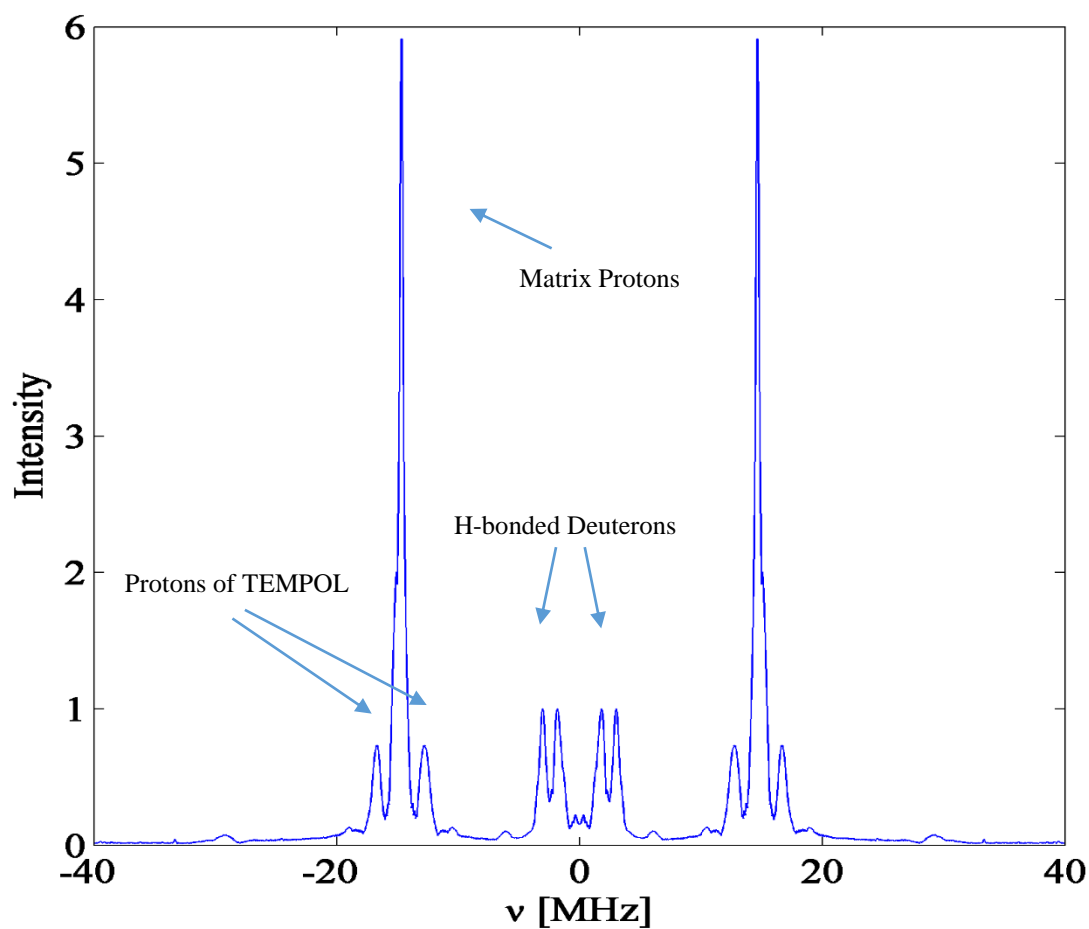


Figure 5-9 Skyline projection of 2D-HYSCORE spectrum for 50 v/v % D_2O/H_2O (70 %) in diglyme with 2 mM TEMPOL at 77 K. The corresponding peaks are assigned.

The H-bonded amplitude was normalized using dividing by echo amplitude and plotted against D_2O concentration.

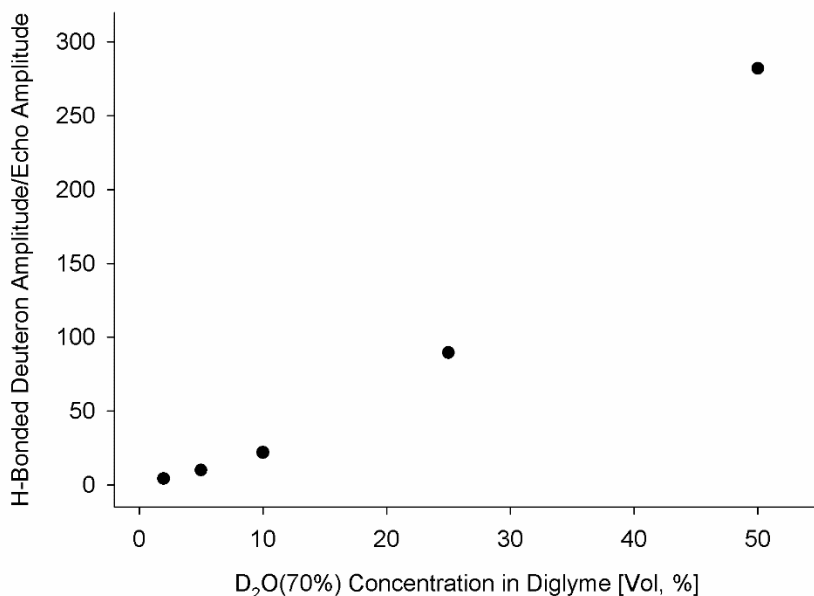


Figure 5-10 The H-bonded amplitude extracted from HYSORE versus the concentration of D₂O/H₂O (70 %) in diglyme. The intensity is related to the skyline projection plot located at 1.8 and 3 GHz.

The intensity change of the H-bonded deuterons peak upon increasing the D₂O concentration is due to the formation of two hydrogen bonded complexes ((NO-H₂O) and NO-(H₂O)₂). This can be used as a calibration plot for water molecules in the vicinity of about 2 Å, because the hydrogen bond length was reported to be 1.74 ± 0.06 Å [110]. We used HYSORE to compare the local water molecule concentration inside lipid bilayers.

CH₃OD was used as another model for hydrogen bond formation and its HYSORE spectrum shows features resembling to water.

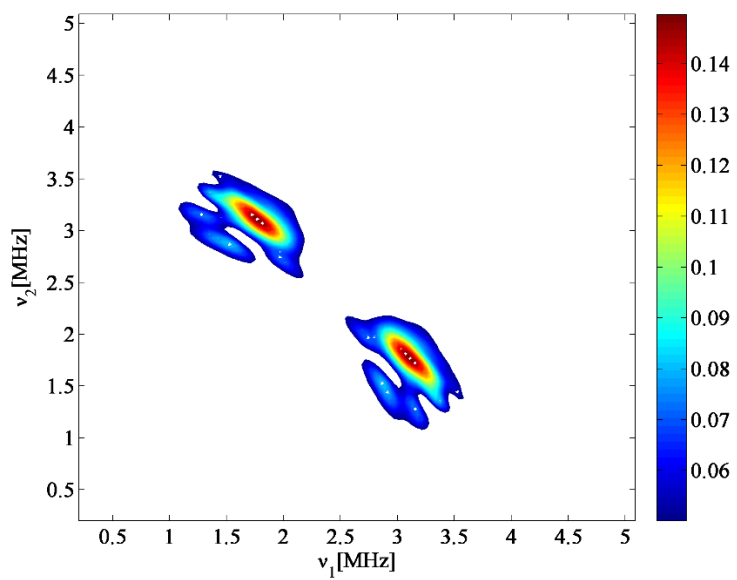


Figure 5-11 Cross-peaks from Deuterons H-bonded to NO group in 1 mM TEMPOL in 100 % CH₃OD.

The HYSCORE intensity of H-bonded deuterons (Figure 5-11) was normalized by echo amplitude and plotted against CH₃OD concentration in diglyme (Figure 5-12).

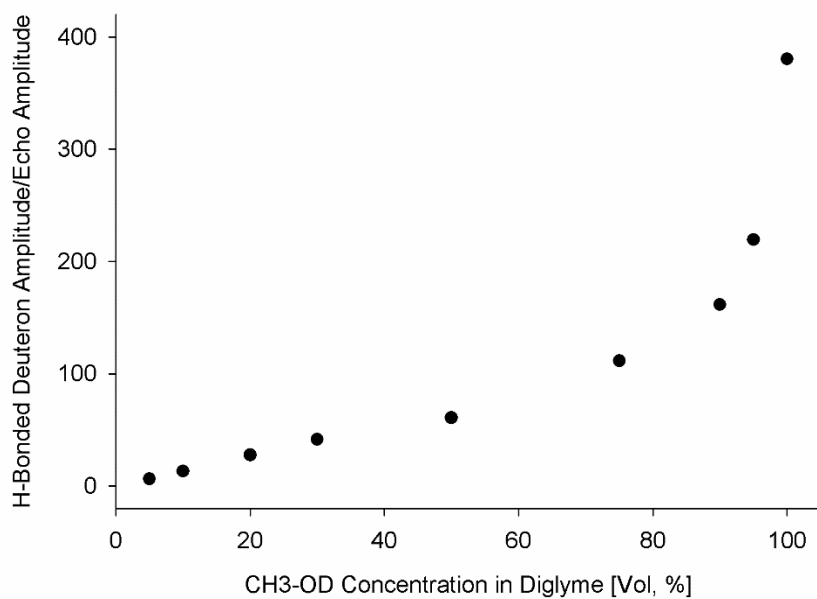


Figure 5-12 The H-bonded amplitude extracted from HYSORE versus the concentration of CH₃OD in diglyme (v/v %).

ESEEM and HYSORE data show that these techniques are able to detect the local water molecules with the distance of about 10 and 2 Å from nitroxide radical respectively.

5.2.4 Water Penetration into the Unilamellar Vesicles

POPG vesicles with 1.7 mole % 10 PC (as spin labeled phospholipid) were prepared in two different diameters. To detect the water interaction with nitroxide radical, the phosphate buffer (pH=7.4) was prepared in deuterated water (70 % D₂O). The three-pulse ESEEM and HYSCORE spectra taken at 77 K showed water penetration into the ULVs (Figure 5-13 to Figure 5-15).

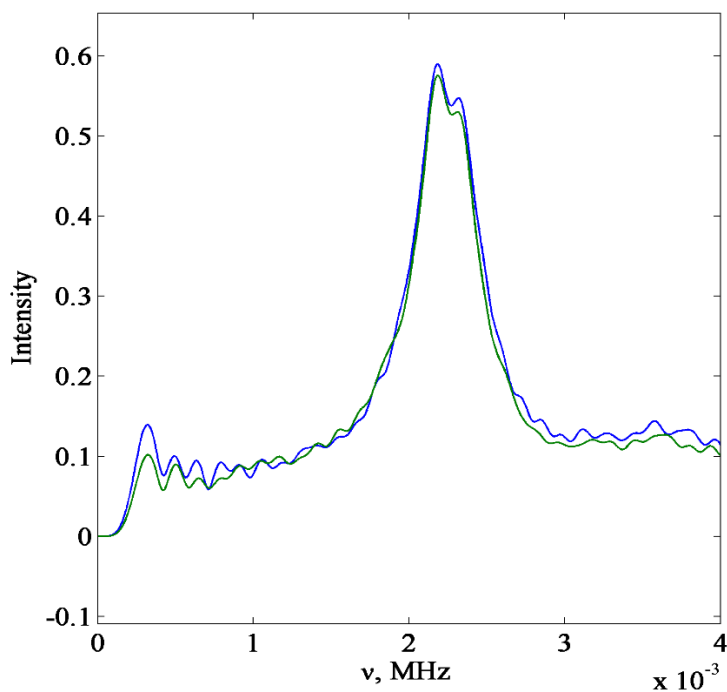


Figure 5-13 Three pulse-ESEEM spectra of 60 nm (green line) and 30 nm (blue line) POPG ULVs with 1.7 mole % 10PC.

HYSCORE spectrum shows the peaks corresponding to the deuteron and proton interaction with radical. The deuteron peak was normalized with respect to the matrix protons.

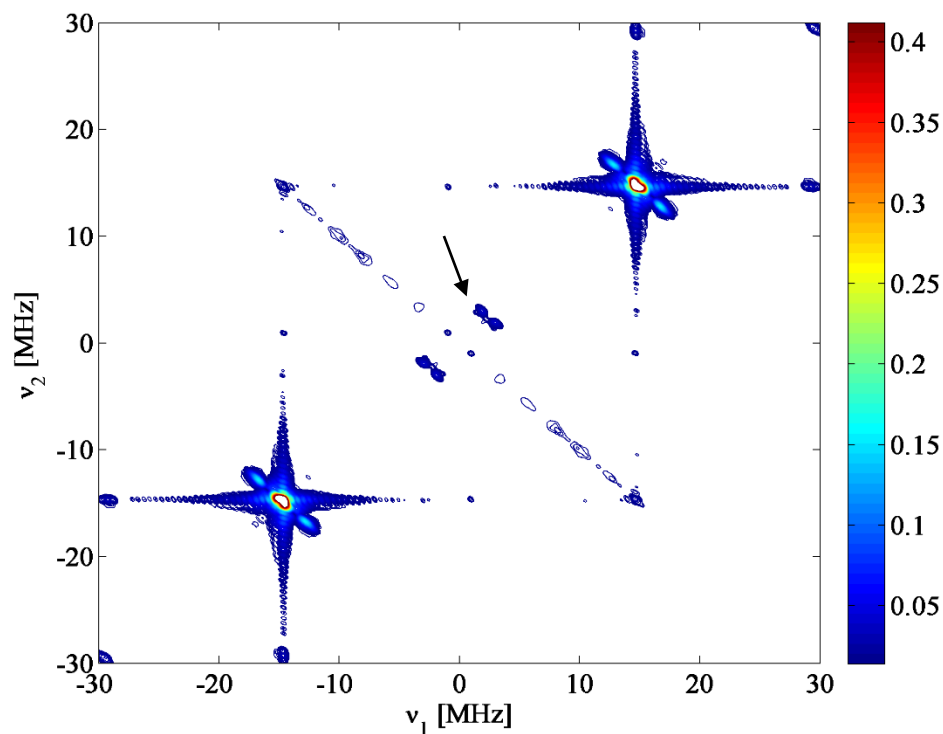


Figure 5-14 HYSCORE of 60 nm POPG ULVs doped with 1.7 mole % 10PC. The black arrow in the spectrum shows deuterons hydrogen bonded to the nitroxide radical. The strong peak at 14.6 GHz corresponds to the protons in the matrix.

The intensity of deuteron hydrogen bonded peak shown in Figure 5-14 (black arrow) is related to the local water concentration close to the radical (in the acyl chain). Therefore we can use the normalized intensity of this peak to compare the amount of water penetrated into lipid bilayers at two different vesicle sizes. Figure 5-15 and Figure 5-16 show the cross peak HYSCORE spectra and their skyline projection for deuterons hydrogen bonded to the nitroxide radical.

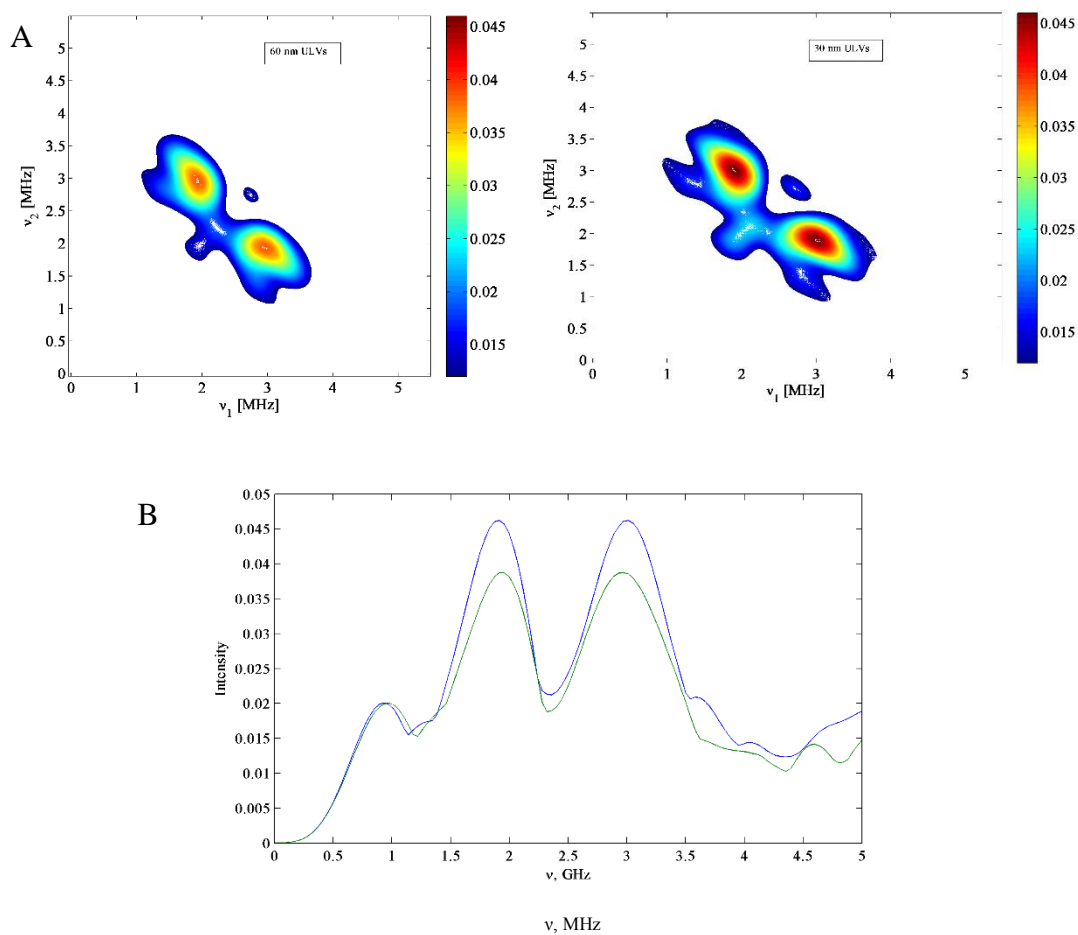


Figure 5-15 A) HYSORE Cross-peaks from deuterons H-bonded to NO group (left: 60 nm, right 30 nm ULVs B) Skyline projection of cross-peaks of 60 nm (green line) and 30 nm (blue line) POPG ULVs with 1.7 mole % 10PC.

Three-pulse ESEEM spectrum showed a signal at $\nu = 2.3$ GHz with similar quadrupole splitting observed in D₂O/diglyme mixture. This signal corresponds to attached and non-attached water molecules and shows an increase of water penetration in smaller vesicles. The intensity of this line is proportional to the number of water molecules around 1 nm distance

from nitroxide radical. To obtain relative local water molecules involving in hydrogen bond formation with nitroxide, HYSCORE spectrum was obtained. The cross peaks from deuterons and skyline projection in Figure 5-15 show higher intensity related to H-bonded water molecule in smaller ULVs. The ratio of hydrogen bonded water molecules, $[\text{H}_2\text{O}]_{\text{H}(60\text{ nm})} / [\text{H}_2\text{O}]_{\text{H}(30\text{ nm})}$ was estimated to be 0.73 by comparing normalized cross peak intensities.

POPG doped with 1.7 mole % 5PC was studied by HYSCORE to investigate the effect of curvature at C5 (carbon 5) position in acyl chain. 116 nm and 69 nm ULVs were prepared and water penetration ratio between these two vesicles was estimated. Nitroxide attached to the position 5 in acyl chain is closer to the polar head group and the water penetration profile in lipid bilayer obtained with other methods shows that the higher water molecules is accessible in 5PC compared to position 10 in 10PC [113, 116]. We used 5PC to investigate the depth of curvature effect on water penetration.

HYSCORE skyline projection and cross peaks for ^2H are shown in Figure 5-16. $[\text{H}_2\text{O}]_{\text{H}(116\text{ nm})} / [\text{H}_2\text{O}]_{\text{H}(69\text{ nm})}$ at C5 position across lipid bilayer was estimated to be 0.86. The higher water penetration was obtained for smaller vesicles in C5 position.

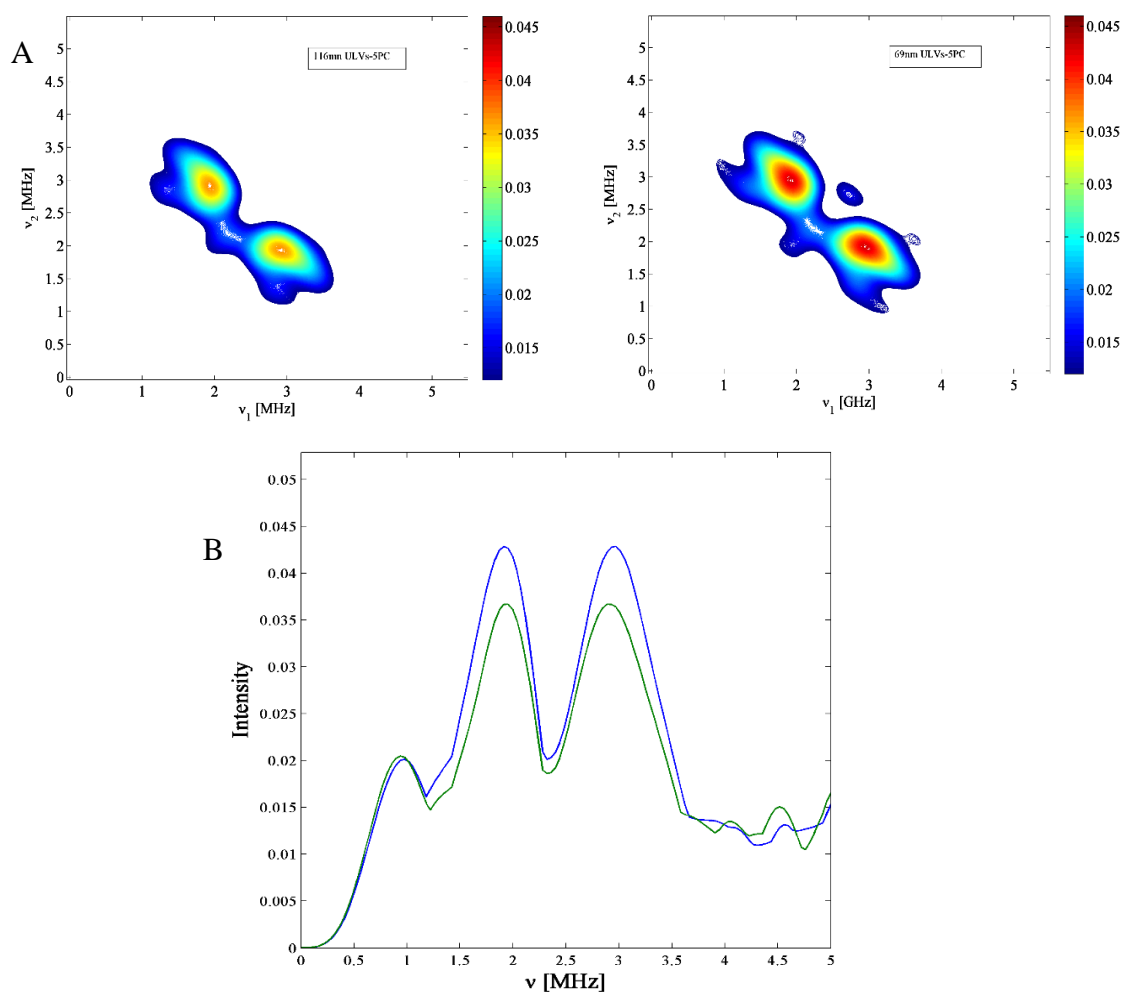


Figure 5-16 HYSORE Cross-peaks from deuterons H-bonded to the NO group (left: 116 nm, right: 69 nm ULVs B) Skyline projection of cross-peaks of 116 nm (green line) and 69 nm (blue line) POPG ULVs with 1.7 mole % 5PC.

We speculate that lipid packing does not affect water penetration into lipid bilayer, however there are some defects in smaller vesicles (Figure 5-17) which could be responsible for the higher water penetration in smaller vesicles. These data are consistent with TEMPO partitioning into ULVs results explained in Chapter 3. Since TEMPO is soluble in water, and

water penetrates into the smaller vesicles through defects, more TEMPO partitioning are expected in highly curved lipid bilayers.

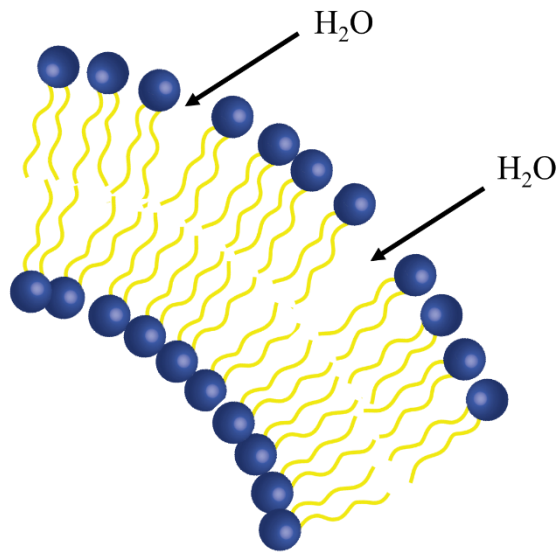


Figure 5-17 Model of highly curved lipid bilayers; the smaller vesicles have more defects in the lipid bilayer.

5.3 Conclusions

HYSCORE and ESEEM as two advanced EPR techniques were used to detect hydrogen bonded water and ethanol to the nitroxide radical (TEMPOL). The spectrum analysis and intensity interpretation of both techniques showed that both are able to detect the local water concentrations, however using HYSCORE, we were able to increase the resolution and accuracy in detecting those water molecules involving in hydrogen bonding. Methanol was also used as another model of hydrogen bonding system. HYSCORE showed well resolved peaks related to the hydrogen bonded water molecules. These peaks were used in lipid bilayer systems to study the local water content in ULVs. ULVs spin labeled with 10PC and 5PC were studied in small and large diameters and it was found that water penetrates more into smaller vesicles which is consistent with that data obtained in Chapter 3.

The data obtained for this chapter is promising for introducing a new technique to characterize and estimate the local water content in systems containing a nitroxide radical.

Summary

- 1- The unilamellar vesicles (ULVs) in different diameters were prepared by extrusion and sonication methods and their dynamics and surface electrostatics were studied.
- 2- The prepared unilamellar and smaller DMPG phospholipid vesicles showed broader DSC traces and less cooperative main phase transition.
- 3- The surface potential of lipid bilayers as an important factor in cell functionality was measured by X-band EPR spectroscopy. A pH-sensitive head-group labeled phospholipid was employed to determine the local electrostatic surface potential and EPR titration method was used to measure the changes in the interfacial pK_a of the probes that was evident from changes in its spectra with pH. Each spectrum was decomposed into the protonated and nonprotonated forms and surface potential was measured from the change of electrostatic contribution of interfacial pK_a .
- 4- Curvature effect on the electrostatic surface potential was studied and the magnitude of the negative surface electrostatic potential, Ψ , increased upon decrease in the vesicle diameter. This effect could be rationalized by assuming different lipid packing upon increase in the ULVs' curvature. For DMPG ULVs in the gel phase the observed effect is not that pronounced. We speculate that biologically relevant fluid bilayer phase allows for a larger variability in the lipid packing density in the lipid polar head group region than a more ordered gel phase.
- 5- To assure a complete probe pH equilibration in both inner and outer leaflets a gramicidin A (gA) proton channel was inserted into LUVs. The electrostatic potentials determined for

vesicles of the same diameter both with and without gA were found to be nearly identical.

It is likely that the lipid flip-flop is responsible for pH equilibration of IMTSL-PTE.

- 6- To measure the flip-flop (transverse diffusion) in curved bilayers, sodium ascorbate as a nitroxide reducing agent was added to the SUVs. The kinetic study of reduction showed that the rate of flip-flop is of the order of 10^{-5} s^{-1} . The rate constant increases when vesicle size decreases. This might be due to higher defects and tension in smaller vesicle which results in faster flip-flop rate.
- 7- The packing of lipids inside bilayer was investigated by carrying out a series of EPR oxygen accessibility experiments by comparing X-band EPR spectra in the presence and the absence of molecular oxygen but at the same temperature. A higher oxygen permeability into the lipid bilayer results in a further broadening of X-band EPR spectra of spin labels located inside the bilayer. We observed an increase in the oxygen permeability coefficient inside larger vesicles by calculating the Lorentzian broadening parameter obtained from simulating each spectrum. This could serve as another proof of a denser lipid packing inside smaller vesicles. Gel phase vesicles compared to the liquid phase vesicles of the same diameter showed a lower oxygen permeability, which can be explained by more packed and rigid lipids when the bilayer is in a gel phase.
- 8- TEMPO partitioning into ULVs was studied by X- and W-band EPR spectroscopy. A higher partitioning into lipid phase was observed in smaller vesicles that can be rationalized by assuming a higher number of defects in more curved lipid bilayers. However the rotational correlation time for TEMPO in smaller vesicles increases, which corresponds to the higher packed lipids.

- 9- Nanopore confined bilayer as model of curved and confined lipid bilayer was prepared by deposition of lipid suspension into Aluminum Anodic Oxide (AAO).
- 10- The surface potential of nanopore confined bilayer was measured with EPR titration method and it was shown that surface potential of POPG lipids inside the AAO pores are higher than that of in vesicles, which is due to highly ordered and packed lipids inside AAO nanotubes.
- 11- AAO surface charge and its spectroscopic properties were investigated and it turns out that AAO shows a weak signal in X-band EPR. It was shown that heating up to 900 °C removes the EPR signal. UV-Vis spectroscopy on AAO samples heated at different temperatures from 300 to 900 °C shows that to make AAO transparent in UV region it needs to be heated up to least 800 °C.
- 12- Zeta potential measurements on AAO samples indicates that AAO is negatively charged at pH higher than 2.3. This negatively charged surface can be used to prepare protein nanotubes inside AAO pores based on electrostatic interactions.
- 13- Cytochrome c and poly glutamic acid as positively and negatively charged macromolecules in physiological pH (7.4) were used to prepared multilayer protein nanotubes. The UV-Vis and CD spectroscopy of these samples showed the existence of layer by layer deposition of 3 double layer of cytochrome c-poly glutamic acid. The comparison of CD and UV-Vis spectroscopy in various wavelength regions for native (in aqueous solution) and deposited cytochrome c indicates that the structure of cytochrome c is disrupted when attached to AAO surface.

- 14- Transmembrane structure of WALP peptide in DOPG lipids deposited into AAO was investigated by CD spectroscopy and it was found that WALP peptide shows an oriented structure when lipids are confined by AAO pores, which indicates the formation of ordered lipid bilayer arrays inside the pores.
- 15- Nanopore confined bilayer placed on QCM crystal can be used as “biosensor” and lipid phase properties inside pores were studied by QCM technique. The lipid phase transition of DMPC was observed in high resolution as a sudden change in QCM frequency and voltage.
- 16- The interaction of peptide with nanopore confined bilayer was studied using antibacterial peptide model, melittin, and its adsorption on lipid surface and later disruption of lipid bilayer were observed with quartz crystal frequency changes. It was shown that QCM-AAO-Lipid is a good system to study interaction and binding of peptides on the surface of lipid bilayers.
- 17- HYSCORE and three-pulse ESEEM as two advanced EPR techniques were used to detect hydrogen bonded water and ethanol to the nitroxide radical (TEMPOL). The spectrum analysis and intensity interpretation of both techniques showed that both are able to detect local water concentrations close to nitroxide radical.
- 18- To increase the resolution and accuracy in detecting water molecules involving in hydrogen bonding, two dimensional three-pulse ESEEM, HYSCORE was employed. Methanol was also used as another model of hydrogen bonding system. HYSCORE showed well resolved peaks related to hydrogen bonded water content. These peaks were used in lipid bilayer systems to study local water content in ULVs.

19- ULVs spin labeled with 10PC and 5PC were studied in small and large diameters and it was found that water penetrates more into smaller vesicles which is consistent with the TEMPO partitioning data obtained from X-band and W-band EPR study.

References

1. Griffith, O.H., P.J. Dehlinger, and S.P. Van, *Shape of the hydrophobic barrier of phospholipid bilayers (evidence for water penetration in biological membranes)*. *J Membr Biol*, 1974. **15**(2): p. 159-92.
2. Alberts B, J.A., Lewis J, et al., *Molecular Biology of the Cell*. The Lipid Bilayer. 2002, New York: Garland Science.
3. Singer, S.J. and G.L. Nicolson, *The Fluid Mosaic Model of the Structure of Cell Membranes*. *Science*, 1972. **175**(4023): p. 720-731.
4. New, R.R.C., *Liposomes: A Practical Approach*. 1990: IRL Press at Oxford University Press.
5. Koynova, R. and B. Tenchov, *Phase Transitions and Phase Behavior of Lipids*, in *Encyclopedia of Biophysics*, G.K. Roberts, Editor. 2013, Springer Berlin Heidelberg. p. 1841-1854.
6. Atkins, P. and J. de Paula, *Atkins' Physical Chemistry*. 2010: OUP Oxford.
7. Macomber, R.S., *A complete introduction to modern NMR spectroscopy*. 1998: Wiley. 179.
8. Junk, M.N., *Electron Paramagnetic Resonance Theory*, in *Assessing the Functional Structure of Molecular Transporters by EPR Spectroscopy*. 2012, Springer Berlin Heidelberg. p. 7-52.
9. Murphy, D.M., *EPR (Electron Paramagnetic Resonance) Spectroscopy of Polycrystalline Oxide Systems*, in *Metal Oxide Catalysis*. 2009, Wiley-VCH Verlag GmbH & Co. KGaA. p. 1-50.
10. Klug, C.S. and J.B. Feix, *Methods and applications of site-directed spin labeling EPR spectroscopy*. *Methods Cell Biol*, 2008. **84**: p. 617-58.
11. Brustolon, M.R., *Electron Paramagnetic Resonance : A Practitioner's Toolkit*. 2009, Hoboken, NJ, USA: Wiley.
12. Weil, J.A. and J.R. Bolton, *Electron paramagnetic resonance : elementary theory and practical applications*. 2nd ed. 2007, Hoboken, N.J.: Wiley-Interscience.

13. García-Rubio, I., *Pulsed EPR: Principles and Examples of Applications to Hemeproteins*, in *Encyclopedia of Biophysics*, G.K. Roberts, Editor. 2013, Springer Berlin Heidelberg. p. 2115-2124.
14. García-Rubio, I., *Pulsed ENDOR and ESEEM: Principles and Examples of Applications to Heme Proteins*, in *Encyclopedia of Biophysics*, G.K. Roberts, Editor. 2013, Springer Berlin Heidelberg. p. 2125-2132.
15. Deligiannakis, Y., M. Louloudi, and N. Hadjiliadis, *Electron spin echo envelope modulation (ESEEM) spectroscopy as a tool to investigate the coordination environment of metal centers*. *Coordination Chemistry Reviews*, 2000. **204**(1): p. 1-112.
16. Höfer, P., et al., *Hyperfine sublevel correlation (hyscore) spectroscopy: a 2D ESR investigation of the squaric acid radical*. *Chemical Physics Letters*, 1986. **132**(3): p. 279-282.
17. *Avanti Polar Lipids, Preparation of liposomes*. Available from: http://www.avantilipids.com/index.php?option=com_content&view=article&id=1384&Itemid=372.
18. Owen, J.S., et al., *Platelet Lipid-Composition and Platelet-Aggregation in Human-Liver Disease*. *Journal of Lipid Research*, 1981. **22**(3): p. 423-430.
19. Boon, J.M., et al., *Facilitated phosphatidylserine (PS) flip-flop and thrombin activation using a synthetic PS scramblase*. *J Am Chem Soc*, 2003. **125**(27): p. 8195-201.
20. Bevers, E.M., et al., *Generation of Prothrombin-Converting Activity and the Exposure of Phosphatidylserine at the Outer Surface of Platelets*. *European Journal of Biochemistry*, 1982. **122**(2): p. 429-436.
21. Vorobyov, I. and T.W. Allen, *On the role of anionic lipids in charged protein interactions with membranes*. *Biochimica Et Biophysica Acta-Biomembranes*, 2011. **1808**(6): p. 1673-1683.
22. Cho, W. and R.V. Stahelin, *Membrane-protein interactions in cell signaling and membrane trafficking*. *Annu Rev Biophys Biomol Struct*, 2005. **34**: p. 119-51.
23. Mulgrew-Nesbitt, A., et al., *The role of electrostatics in protein-membrane interactions*. *Biochimica et Biophysica Acta (BBA) - Molecular and Cell Biology of Lipids*, 2006. **1761**(8): p. 812-826.

24. Deol, S.S., et al., *Lipid-Protein Interactions of Integral Membrane Proteins: A Comparative Simulation Study*. Biophysical Journal, 2004. **87**(6): p. 3737-3749.
25. Franklin, J.C., et al., *Probes of membrane electrostatics: synthesis and voltage-dependent partitioning of negative hydrophobic ion spin labels in lipid vesicles*. Biophys J, 1993. **64**(3): p. 642-53.
26. Cevc, G., *Membrane electrostatics*. Biochim Biophys Acta, 1990. **1031**(3): p. 311-82.
27. Cevc, G. and D. Marsh, *Phospholipid bilayers: physical principles and models*. 1987: Wiley.
28. Franklin, J.C. and D.S. Cafiso, *Internal electrostatic potentials in bilayers: measuring and controlling dipole potentials in lipid vesicles*. Biophys J, 1993. **65**(1): p. 289-99.
29. Demchenko, A.P. and S.O. Yesylevskyy, *Nanoscopic description of biomembrane electrostatics: results of molecular dynamics simulations and fluorescence probing*. Chemistry and Physics of Lipids, 2009. **160**(2): p. 63-84.
30. Zakharov, S.D., et al., *Tuning the membrane surface potential for efficient toxin import*. Proc Natl Acad Sci U S A, 2002. **99**(13): p. 8654-9.
31. Rottenberg, H., [17] *Determination of surface potential of biological membranes*, in *Methods in Enzymology*, B.F. Sidney Fleischer, Editor. 1989, Academic Press. p. 364-375.
32. Cafiso, D., et al., [16] *Measuring electrostatic potentials adjacent to membranes*, in *Methods in Enzymology*, B.F. Sidney Fleischer, Editor. 1989, Academic Press. p. 342-364.
33. Fromherz, P., [18] *Lipid coumarin dye as a probe of interfacial electrical potential in biomembranes*, in *Methods in Enzymology*, B.F. Sidney Fleischer, Editor. 1989, Academic Press. p. 376-387.
34. Lindström, F., P.T.F. Williamson, and G. Gröbner, *Molecular Insight into the Electrostatic Membrane Surface Potential by ¹⁴N/³¹P MAS NMR Spectroscopy: Nociceptin-Lipid Association*. Journal of the American Chemical Society, 2005. **127**(18): p. 6610-6616.
35. Fernandez, M.S. and P. Fromherz, *Lipoid pH indicators as probes of electrical potential and polarity in micelles*. The Journal of Physical Chemistry, 1977. **81**(18): p. 1755-1761.

36. Marra, J., *Direct measurement of the interaction between phosphatidylglycerol bilayers in aqueous electrolyte solutions*. Biophys J, 1986. **50**(5): p. 815-25.
37. Shin, Y.K. and W.L. Hubbell, *Determination of electrostatic potentials at biological interfaces using electron-electron double resonance*. Biophysical Journal, 1992. **61**(6): p. 1443-1453.
38. Shin, Y.K. and W.L. Hubbell, *Determination of electrostatic potentials at biological interfaces using electron-electron double resonance*. Biophys J, 1992. **61**(6): p. 1443-53.
39. Riske, K.A., et al., *Probing DMPG vesicle surface with a cationic aqueous soluble spin label*. Biochim Biophys Acta, 1999. **1418**(1): p. 133-46.
40. Khramtsov, V.V., et al., *The application of pH-sensitive spin labels to studies of surface potential and polarity of phospholipid membranes and proteins*. Biochim Biophys Acta, 1992. **1104**(2): p. 317-24.
41. Cafiso, D.S. and W.L. Hubbell, *EPR determination of membrane potentials*. Annu Rev Biophys Bioeng, 1981. **10**: p. 217-44.
42. Castle, J.D. and W.L. Hubbell, *Estimation of membrane surface potential and charge density from the phase equilibrium of a paramagnetic amphiphile*. Biochemistry, 1976. **15**(22): p. 4818-4831.
43. Gaffney, B.J. and R.J. Mich, *A new measurement of surface charge in model and biological lipid membranes*. Journal of the American Chemical Society, 1976. **98**(10): p. 3044-3045.
44. Mehlhorn, R.J. and L. Packer, [46] *Membrane surface potential measurements with amphiphilic spin labels*, in *Methods in Enzymology*, L.P. Sidney Fleischer, Editor. 1979, Academic Press. p. 515-526.
45. Mehlhorn, R.J. and L. Packer, *Membrane surface potential measurements with amphiphilic spin labels*. Methods Enzymol, 1979. **56**: p. 515-26.
46. Cafiso, D.S. and W.L. Hubbell, *Light-induced interfacial potentials in photoreceptor membranes*. Biophys J, 1980. **30**(2): p. 243-63.
47. Khramtsov, V. and L. Volodarsky, *Use of Imidazoline Nitroxides in Studies of Chemical Reactions ESR Measurements of the Concentration and Reactivity of Protons, Thiols, and Nitric Oxide*, in *Biological Magnetic Resonance*, L. Berliner, Editor. 2002, Springer US. p. 109-180.

48. Hartley, G.S. and J.W. Roe, *Ionic concentrations at interfaces*. Transactions of the Faraday Society, 1940. **35**: p. 101-109.
49. Fromherz, P., *A new method for investigation of lipid assemblies with a lipid pH indicator in monomolecular films*. Biochimica et Biophysica Acta (BBA) - Biomembranes, 1973. **323**(2): p. 326-334.
50. Fromherz, P., *Acid-base sensitization of fluorescence by energy transfer in an ordered dye-lipid-electrolyte lamella*. Chemical Physics Letters, 1974. **26**(2): p. 221-224.
51. Voinov, M.A., I. Rivera-Rivera, and A.I. Smirnov, *Surface electrostatics of lipid bilayers by EPR of a pH-sensitive spin-labeled lipid*. Biophys J, 2013. **104**(1): p. 106-16.
52. Voinov, M.A., I.A. Kirilyuk, and A.I. Smirnov, *Spin-labeled pH-sensitive phospholipids for interfacial pKa determination: synthesis and characterization in aqueous and micellar solutions*. J Phys Chem B, 2009. **113**(11): p. 3453-60.
53. Drin, G., et al., *A general amphipathic alpha-helical motif for sensing membrane curvature*. Nature Structural & Molecular Biology, 2007. **14**(2): p. 138-146.
54. Middleton, E.R. and E. Rhoades, *Effects of Curvature and Composition on alpha-Synuclein Binding to Lipid Vesicles*. Biophysical Journal, 2010. **99**(7): p. 2279-2288.
55. Zakharov, S.D., et al., *Tuning the membrane surface potential for efficient toxin import*. Proceedings of the National Academy of Sciences, 2002. **99**(13): p. 8654-8659.
56. Hallett, F.R., J. Watton, and P. Krygsmann, *Vesicle sizing: Number distributions by dynamic light scattering*. Biophys J, 1991. **59**(2): p. 357-62.
57. Biltonen, R.L. and D. Lichtenberg, *The use of differential scanning calorimetry as a tool to characterize liposome preparations*. Chemistry and Physics of Lipids, 1993. **64**(1-3): p. 129-142.
58. Cornell, B.A., J. Middlehurst, and F. Separovic, *Small phospholipid vesicles cannot undergo a fluid-to-crystalline phase transition*. Chemical Physics Letters, 1980. **73**(3): p. 569-571.
59. Chiu, M.H. and E.J. Prenner, *Differential scanning calorimetry: An invaluable tool for a detailed thermodynamic characterization of macromolecules and their interactions*. Journal of Pharmacy and Bioallied Sciences, 2011. **3**(1): p. 39-59.

60. McElhaney, R.N., *The use of differential scanning calorimetry and differential thermal analysis in studies of model and biological membranes*. Chemistry and Physics of Lipids, 1982. **30**(2–3): p. 229-259.
61. Schwarz, G. and G. Beschiaschvili, *Thermodynamic and kinetic studies on the association of melittin with a phospholipid bilayer*. Biochim Biophys Acta, 1989. **979**(1): p. 82-90.
62. Zhao, W., et al., *Atomic-Scale Structure and Electrostatics of Anionic Palmitoyloleoylphosphatidylglycerol Lipid Bilayers with Na⁺ Counterions*. Biophysical journal, 2007. **92**(4): p. 1114-1124.
63. Héning, J.r.m., W. Shinoda, and M.L. Klein, *Models for Phosphatidylglycerol Lipids Put to a Structural Test*. The Journal of Physical Chemistry B, 2009. **113**(19): p. 6958-6963.
64. Kukol, A., *Lipid Models for United-Atom Molecular Dynamics Simulations of Proteins*. Journal of Chemical Theory and Computation, 2009. **5**(3): p. 615-626.
65. Riske, K.A., et al., *Temperature and ionic strength dependent light scattering of DMPG dispersions*. Chemistry and Physics of Lipids, 1997. **89**(1): p. 31-44.
66. Kelkar, D.A. and A. Chattopadhyay, *The gramicidin ion channel: a model membrane protein*. Biochim Biophys Acta, 2007. **1768**(9): p. 2011-25.
67. Paleos, C.M. and P. Dais, *Ready reduction of some nitroxide free radicals with ascorbic acid*. Journal of the Chemical Society, Chemical Communications, 1977(10): p. 345-346.
68. Kornberg, R.D. and H.M. McConnell, *Inside-outside transitions of phospholipids in vesicle membranes*. Biochemistry, 1971. **10**(7): p. 1111-20.
69. Kol, M.A., et al., *Phospholipid flop induced by transmembrane peptides in model membranes is modulated by lipid composition*. Biochemistry, 2003. **42**(1): p. 231-7.
70. Nakano, M., et al., *Flip-flop of phospholipids in vesicles: kinetic analysis with time-resolved small-angle neutron scattering*. J Phys Chem B, 2009. **113**(19): p. 6745-8.
71. Gerelli, Y., et al., *Lipid exchange and flip-flop in solid supported bilayers*. Langmuir, 2013. **29**(41): p. 12762-9.

72. Kučerka, N., et al., *Scattering Density Profile Model of POPG Bilayers As Determined by Molecular Dynamics Simulations and Small-Angle Neutron and X-ray Scattering Experiments*. The Journal of Physical Chemistry B, 2012. **116**(1): p. 232-239.
73. McConnell, H.M. and R.D. Kornberg, *Inside-outside transitions of phospholipids in vesicle membranes*. Biochemistry, 1971. **10**(7): p. 1111-1120.
74. Smirnov, A.I., R.B. Clarkson, and R.L. Belford, *EPR Linewidth (T₂) Method to Measure Oxygen Permeability of Phospholipid Bilayers and Its Use to Study the Effect of Low Ethanol Concentrations*. Journal of Magnetic Resonance, Series B, 1996. **111**(2): p. 149-157.
75. Shimshick, E.J. and H.M. McConnell, *Lateral phase separation in phospholipid membranes*. Biochemistry, 1973. **12**(12): p. 2351-2360.
76. Smirnov, A.I., T.I. Smirnova, and P.D. Morse, 2nd, *Very high frequency electron paramagnetic resonance of 2,2,6,6-tetramethyl-1-piperidinyloxy in 1,2-dipalmitoyl-sn-glycero-3-phosphatidylcholine liposomes: partitioning and molecular dynamics*. Biophys J, 1995. **68**(6): p. 2350-60.
77. Nuscher, B., et al., *alpha-synuclein has a high affinity for packing defects in a bilayer membrane - A thermodynamics study*. Journal of Biological Chemistry, 2004. **279**(21): p. 21966-21975.
78. Polnaszek, C.F., et al., *Analysis of the factors determining the EPR spectra of spin probes that partition between aqueous and lipid phases*. Journal of the American Chemical Society, 1978. **100**(26): p. 8223-8232.
79. Smirnov, A., R.L. Belford, and R.B. Clarkson, *Comparative Spin Label Spectra at X-Band and W-band*, in *Biological Magnetic Resonance*, L. Berliner, Editor. 2002, Springer US. p. 95-97.
80. Li, R.Q., et al., *Polarization-dependent fluorescence of proteins bound to nanopore-confined lipid bilayers*. J Chem Phys, 2008. **129**(9): p. 095102.
81. Cremer, P.S. and S.G. Boxer, *Formation and Spreading of Lipid Bilayers on Planar Glass Supports*. The Journal of Physical Chemistry B, 1999. **103**(13): p. 2554-2559.
82. Smirnov, A.I. and O.G. Poluektov, *Substrate-Supported Lipid Nanotube Arrays*. Journal of the American Chemical Society, 2003. **125**(28): p. 8434-8435.
83. Smirnov, A.I., *Nanotube structures having a surfactant bilayer inner wall coating*, U. Patent, Editor 2011, North Carolina State University: USA.

84. Ballister, E.R., et al., *In vitro self-assembly of tailorable nanotubes from a simple protein building block*. Proceedings of the National Academy of Sciences, 2008. **105**(10): p. 3733-3738.
85. Lee, S.B., et al., *Antibody-Based Bio-Nanotube Membranes for Enantiomeric Drug Separations*. Science, 2002. **296**(5576): p. 2198-2200.
86. Komatsu, T., *Protein-based nanotubes for biomedical applications*. Nanoscale, 2012. **4**(6): p. 1910-1918.
87. Perry, J.L., C.R. Martin, and J.D. Stewart, *Drug-Delivery Strategies by Using Template-Synthesized Nanotubes*. Chemistry – A European Journal, 2011. **17**(23): p. 6296-6302.
88. Tian, Y., et al., *Fabrication of Protein Nanotubes Based on Layer-by-Layer Assembly*. Biomacromolecules, 2006. **7**(9): p. 2539-2542.
89. Hou, S., J. Wang, and C.R. Martin, *Template-Synthesized Protein Nanotubes*. Nano Letters, 2005. **5**(2): p. 231-234.
90. Friscia, S., S.L. Turchi, and C.E. Hepfer, *The influence of pH on electrophoretic mobility, a laboratory investigation*. Biochemical Education, 1992. **20**(1): p. 41-42.
91. Caesar, C.E.B., et al., *Assigning Membrane Binding Geometry of Cytochrome c by Polarized Light Spectroscopy*. Biophysical Journal, 2009. **96**(8): p. 3399-3411.
92. Sanghera, N. and T.J. Pinheiro, *Unfolding and refolding of cytochrome c driven by the interaction with lipid micelles*. Protein Sci, 2000. **9**(6): p. 1194-202.
93. Santucci, R. and F. Ascoli, *The Soret circular dichroism spectrum as a probe for the heme Fe(III)-Met(80) axial bond in horse cytochrome c*. Journal of Inorganic Biochemistry, 1997. **68**(3): p. 211-214.
94. Steinbrecher, T., et al., *Peptide-Lipid Interactions of the Stress-Response Peptide TisB That Induces Bacterial Persistence*. Biophysical Journal, 2012. **103**(7): p. 1460-1469.
95. Weiss, T.M., et al., *Hydrophobic Mismatch between Helices and Lipid Bilayers*. Biophysical Journal, 2003. **84**(1): p. 379-385.
96. Chernyakova, K.V., et al., *Nature of paramagnetic centers in anodic aluminum oxide formed in a solution of tartaric acid*. Russian Journal of Physical Chemistry A, 2012. **86**(10): p. 1630-1635.

97. Dixon, M.C., *Quartz Crystal Microbalance with Dissipation Monitoring: Enabling Real-Time Characterization of Biological Materials and Their Interactions*. Journal of Biomolecular Techniques : JBT, 2008. **19**(3): p. 151-158.
98. Lazarowich, R.J., et al., *Fabrication of porous alumina on quartz crystal microbalances*. Journal of Applied Physics, 2007. **101**(10): p. 104909.
99. Balbuena, P.B. and K.E. Gubbins, *Theoretical interpretation of adsorption behavior of simple fluids in slit pores*. Langmuir, 1993. **9**(7): p. 1801-1814.
100. Brunauer, S., P.H. Emmett, and E. Teller, *Adsorption of Gases in Multimolecular Layers*. Journal of the American Chemical Society, 1938. **60**(2): p. 309-319.
101. Wargenau, A. and N. Tufenkji, *Direct detection of the gel-fluid phase transition of a single supported phospholipid bilayer using quartz crystal microbalance with dissipation monitoring*. Anal Chem, 2014. **86**(16): p. 8017-20.
102. Toombes, G.E.S., et al., *Determination of α -III Phase Transition Temperature for 1,2-Dioleoyl-*sn*-Glycero-3-Phosphatidylethanolamine*. Biophysical Journal, 2002. **82**(5): p. 2504-2510.
103. Rodahl, M., et al., *Quartz crystal microbalance setup for frequency and *Q*-factor measurements in gaseous and liquid environments*. Review of Scientific Instruments, 1995. **66**(7): p. 3924-3930.
104. Wang, K.F., R. Nagarajan, and T.A. Camesano, *Antimicrobial peptide alamethicin insertion into lipid bilayer: A QCM-D exploration*. Colloids and Surfaces B: Biointerfaces, 2014. **116**(0): p. 472-481.
105. Lundquist, A., et al., *Melittin-Lipid interaction: A comparative study using liposomes, micelles and bilayer disks*. Biochimica et Biophysica Acta (BBA) - Biomembranes, 2008. **1778**(10): p. 2210-2216.
106. de Bony, J., J. Dufourcq, and B. Clin, *Lipid-protein interactions: NMR study of melittin and its binding to lysophosphatidylcholine*. Biochim Biophys Acta, 1979. **552**(3): p. 531-4.
107. Naito, A., et al., *Conformation and dynamics of melittin bound to magnetically oriented lipid bilayers by solid-state (³¹P and (¹³C NMR spectroscopy*. Biophysical Journal, 2000. **78**(5): p. 2405-2417.

108. Neubacher, H., et al., *Permeabilization assay for antimicrobial peptides based on pore-spanning lipid membranes on nanoporous alumina*. Langmuir, 2014. **30**(16): p. 4767-74.
109. Hain, N., M. Gallego, and I. Reviakine, *Unraveling Supported Lipid Bilayer Formation Kinetics: Osmotic Effects*. Langmuir, 2013. **29**(7): p. 2282-2288.
110. Smirnova, T.I., et al., *Geometry of hydrogen bonds formed by lipid bilayer nitroxide probes: a high-frequency pulsed ENDOR/EPR study*. J Am Chem Soc, 2007. **129**(12): p. 3476-7.
111. White, S.H., *Membrane Protein Insertion: The Biology–Physics Nexus*. The Journal of General Physiology, 2007. **129**(5): p. 363-369.
112. Bartucci, R., et al., *Intramembrane Polarity by Electron Spin Echo Spectroscopy of Labeled Lipids*. Biophysical Journal, 2003. **84**(2): p. 1025-1030.
113. Marsh, D., *Membrane water-penetration profiles from spin labels*. Eur Biophys J, 2002. **31**(7): p. 559-62.
114. Marsh, D., *Polarity and permeation profiles in lipid membranes*. Proc Natl Acad Sci U S A, 2001. **98**(14): p. 7777-82.
115. Conte, E., et al., *Lipid peroxidation and water penetration in lipid bilayers: a W-band EPR study*. Biochim Biophys Acta, 2013. **1828**(2): p. 510-7.
116. Erilov, D.A., et al., *Water concentration profiles in membranes measured by ESEEM of spin-labeled lipids*. J Phys Chem B, 2005. **109**(24): p. 12003-13.
117. Milov, A.D., et al., *ESEEM Measurements of Local Water Concentration in D2O-Containing Spin-Labeled Systems*. Applied Magnetic Resonance, 2008. **35**(1): p. 73-94.
118. Angell, C.A., J.M. Sare, and E.J. Sare, *Glass transition temperatures for simple molecular liquids and their binary solutions*. The Journal of Physical Chemistry, 1978. **82**(24): p. 2622-2629.